UNIVERSIDADE FEDERAL DO CEARÁ

CENTRO DE TECNOLOGIA

DEPARTAMENTO DE ENGENHARIA METALÚRGICA E DE MATERIAIS

PROGRAMA DE PÓS-GRADUAÇÃO EM ENGENHARIA E CIÊNCIA DE MATERIAIS

MESTRADO EM ENGENHARIA E CIÊNCIA DE MATERIAIS

PEDRO PAULO NUNES MAIA

PLASTICITY OF THE HEAT-AFFECTED ZONE IN 9NI STEEL WELDED PIPES: EVALUATION OF THE MICROCONSTITUENTS' DEFORMABILITY

FORTALEZA

2022

PEDRO PAULO NUNES MAIA

PLASTICITY OF THE HEAT-AFFECTED ZONE IN 9NI STEEL WELDED PIPES: EVALUATION OF THE MICROCONSTITUENTS' DEFORMABILITY

Thesis submitted to the Post-Graduate Program in Engineering and Materials Science of the Universidade Federal do Ceará, in partial fulfilment of the requirements for the degree of Master in Materials Science and Engineering. Concentration area: Physical and Mechanical Properties of Materials.

Advisor: Prof. Dr. Cleiton Carvalho Silva

Coadvisor: Prof. Dr. Émerson Mendonça Miná

FORTALEZA

2022

Dados Internacionais de Catalogação na Publicação
Universidade Federal do Ceará
Biblioteca Universitária
Gerada automaticamente pelo módulo Catalog, mediante os dados fornecidos pelo(a) autor(a)

M187p Maia, Pedro Paulo Nunes.
Plasticity of the heat-affected zone in 9Ni steel welded pipes : Evaluation of the microconstituents' deformability / Pedro Paulo Nunes Maia. – 2022.
106 f. : il. color.

Dissertação (mestrado) – Universidade Federal do Ceará, Centro de Tecnologia, Programa de Pós-Graduação em Engenharia e Ciência de Materiais, Fortaleza, 2022.
Orientação: Prof. Dr. Cleiton Carvalho Silva.
Coorientação: Prof. Dr. Émerson Mendonça Miná.

1. 9Ni steels. 2. Heat-affected zone. 3. Micromechanical characterisation. 4. Plasticity. 5. Electron backscatter diffraction. I. Título.

CDD 620.11

PEDRO PAULO NUNES MAIA

PLASTICITY OF THE HEAT-AFFECTED ZONE IN 9NI STEEL WELDED PIPES: EVALUATION OF THE MICROCONSTITUENTS' DEFORMABILITY

Thesis submitted to the Post-Graduate Program in Engineering and Materials Science of the Universidade Federal do Ceará, in partial fulfilment of the requirements for the degree of Master in Materials Science and Engineering. Concentration area: Physical and Mechanical Properties of Materials.

Approved at: May 25th, 2022

EXAMINING COMMISSION

Prof. Dr. Cleiton Carvalho Silva (Advisor)
Universidade Federal do Ceará (UFC)

Prof. Dr. Émerson Mendonça Miná (Coadvisor)
Universidade Federal do Ceará (UFC)

Prof. Dr. Hamilton Ferreira Gomes de Abreu
Universidade Federal do Ceará (UFC)

Dr. Marcelo Torres Piza Paes
Centro de Pesquisas Leopoldo Américo Miguez de Mello (CENPES/Petrobras)

To my parents, João and Maria.

To my siblings, Tarcísio and Thamyres.

To my partner, Jéssica.

ACKNOWLEDGEMENTS

To my parents, João and Maria, who cared so much for the education of their children, making every effort to guarantee the best opportunities for them. To my brother, Tarcísio, for being a reference for me, and to my sister, Thamyres, for always being a friend willing to listen and advise me. To Brazilina, for all the care and affection. To my significant other, Jéssica, who has stood by me through all my academic journey, helping me in each way possible, sharing all the joys and frustrations. I love you so much.

I would like to express my sincere gratitude to my advisor, Professor Cleiton Carvalho Silva, for the trust placed in my work, for the encouragement and for your immense contribution to this thesis. Thank you for believing in my potential and for inspiring me to achieve my goals. I would also like to thank my coadvisor, Professor Émerson Mendonça Miná, for his immense support, making every effort to help me overcome the difficulties faced throughout this work.

I would like to thank the *Universidade Federal do Ceará* (UFC), in special, the professors of the *Departamento de Engenharia e Ciência de Materiais* (DEMM). A special thanks to my friend, Professor Elineudo Pinho de Moura.

To persons of the *Laboratório de Pesquisa e Tecnologia em Soldagem* (LPTS) – students, assistants, technicians, engineers and professors. A special thanks to Bruno, Mário and Lucas, for giving support manufacturing the specimens and performing the mechanical tests, and to Professors Willys Machado Aguiar and Hélio Cordeiro de Miranda for the lessons and the constructive discussions.

To persons of the *Laboratório de Pesquisa em Corrosão* (LPC) and the *Laboratório de Caracterização de Materiais* (LACAM) for aiding in samples preparation and for sharing researches.

To my friends: Madson, Rodrigo, Igor, Artur, Samuel, Davi, Rocha, Vicente and Ravel. Thank you for bringing joy to these hard times.

I would like to thank the *Central Analítica*-UFC (funded by FINEP-CT-INFRA, CAPES-*Pró-Equipamentos*, and MCTI-CNPq-SisNano2.0). I would also like to thank the *Agência Nacional do Petróleo, Gás Natural e Biocombustíveis* (ANP), the *Financiadora de Estudos e Projetos* (FINEP) and the *Ministério da Ciência, Tecnologia e Inovação* (MCTI) for the financial support through the *Programa de Recursos Humanos da* ANP *para o Setor Petróleo e Gás* (PRH-ANP/MCTI). This study was financed in part by the *Coordenação de Aperfeiçoamento de Pessoal de Nível Superior – Brasil* (CAPES) – Finance Code 001.

I think that the right way, of course, is to say the whole structural interconnections of the thing is the thing that we have to look at, that all the sciences and all the efforts, not just the sciences but all the efforts of intellectual kinds, are to see the connections of the hierarchies, to connect beauty to history, to connect history to man's psychology, man's psychology to the working of the brain, the brain to the neural impulse, the neural impulse to the chemistry, and so forth, up and down, both ways. And today we cannot, and there's no use making believe we can, draw carefully a line all the way from one end of this thing to the other, in fact we just begun to see that there is this relative hierarchy (FEYNMAN, 1964).

ABSTRACT

Low carbon nickel-alloyed steels have been, through decades, applied in services that demand good toughness at low temperatures. Within this group, 9Ni steel stands out as the most traditional material used to transport and store liquefied natural gas. 9Ni steels have been recently adopted in supercritical CO_2 injection systems in deepwater oil fields. The manufacture of these subsea systems involves multi-pass welding procedures, which produce a lath martensitic Heat-Affected Zone (HAZ) with high heterogeneity of microstructural features and local mechanical properties, and may introduce Local Brittle Zones (LBZ) at the Coarse-Grained HAZ (CGHAZ). A detailed microstructural investigation was conducted along the this HAZ, mapping local mechanical properties and correlating the microstructural features with the mechanical behaviour during plastic deformation. The results revealed that the highest microhardness values are found at the Super-critically reheated CGHAZ (SCR-CGHAZ), characterised by its refined microstructure and a quite low area fraction of coarse lath martensites. The Subcritically reheated CGHAZ (SC-CGHAZ) and the Intercritically reheated CGHAZ (IC-CGHAZ) – regions with wider martensite blocks and higher coarse lath area fraction – composed the softer zones of the HAZ. However, reheating at intercritical temperatures induces the formation of fresh martensite and the stabilisation C-rich retained/reversed austenite particles, which may degrade the mechanical properties at the IC-CGHAZ. Furthermore, analysis of the HAZ plasticity – focusing on the contribution of coarse martensite laths to its deformability – revealed that the CGHAZ is the only HAZ region that experiences significant strain, with the SC-CGHAZ presenting the highest strain levels. Regarding the coarse laths, Electron Backscatter Diffraction (EBSD) analyses on progressively deformed specimens showed that these constituents might carry plasticity during most of the early plastic regime until the microstructure reaches a state of high constraint, participating in a hierarchic plastic deformation, which is initiated with the strain-induced martensitic transformation of interlath austenite films. The present thesis brings solid results regarding the microstructural characterisation of the HAZ in 9Ni steel girth welded pipes, aiding in understanding how multipass welding processing may impact the mechanical properties of the HAZ. It also brings new insights on the mechanical behaviour of lath martensite, assessing how its microconstituents, especially the coarse martensite laths, may contribute to its deformability.

Keywords: 9Ni steels. Heat-affected zone. Micromechanical characterisation. Plasticity. Electron backscatter diffraction.

RESUMO

Aços baixo carbono ligados ao níquel têm, ao longo de décadas, sido aplicados em serviços que demandam boa tenacidade a baixas temperaturas. Nessa família, o aço 9Ni destaca-se como o principal material aplicado no transporte e armazenamento de gás natural liquefeito. Recentemente, o aço 9Ni tem sido adotado na fabricação de sistemas de injeção de CO_2 supercrítico em campos de petróleo em águas profundas, um processo que demanda a aplicação de uma soldagem multipasse, a qual produzirá uma Zona Afetada pelo Calor (ZAC) composta por martensita em ripas com elevada heterogeneidade de características microestruturais e de propriedades mecânicas locais, apresentando riscos de introdução de zonas frágeis localizadas na ZAC de Grãos Grosseiros (ZACGG). Uma extensiva investigação microestrutural foi conduzida ao longo desta ZAC, mapeando as propriedades mecânicas locais e correlacionando características microestruturais ao comportamento mecânico durante a deformação plástica. Os resultados revelaram que os maiores valores de microdureza são observados na ZACGG supercrítica, caracterizada por sua microestrutura refinada e sua baixa fração de ripas grosseiras. A ZACGG Subcrítica (ZACGG-SC) e a ZACGG Intercrítica (ZACGG-IC) – regiões com blocos de martensita mais largos e com maior fração de ripas grosseiras – compõem as regiões mais macias da ZAC. Também foi observado que reaquecimentos intercríticos podem induzir a formação de martensita fresca e a estabilização de austenita retida rica em C, impactando as propriedades mecânicas da ZACGG-IC. Ademais, análises sobre a plasticidade da ZAC revelaram que a ZACGG é a única região que sofre deformação significativa, com a ZACGG-SC apresentando os maiores níveis de deformação. Em relação às ripas grosseiras, análises de difração de elétrons retroespalhados revelaram que estas podem conduzir a plasticidade durante o início do regime plástico até que a microestrutura atinja um estado de alta restrição, participando de uma deformação plástica hierárquica, que é iniciada pela transformação martensítica induzida por deformação dos filmes de austenita entre ripas. Esta dissertação traz resultados consistentes sobre a caracterização microstrutural da ZAC em tubos soldados de aço 9Ni, auxiliando no entendimento de como um processo multipasse pode impactar as propriedades mecânicas da ZAC. Ela também traz novas percepções sobre o comportamento mecânico da martensita em ripas, verificando como seus microconstituintes, especialmente as ripas grosseiras, podem contribuir para sua deformabilidade.

Palavras-chave: Aços 9Ni. Zona afetada pelo calor. Caracterização micromecânica. Plasticidade. Difração de elétrons retroespalhados.

LIST OF FIGURES

LIST OF TABLES

LIST OF ABBREVIATIONS AND ACRONYMS

APT	Atom Probe Tomography
BCC	Body-Centered Cubic
BCT	Body-Centered Tetragonal
BM	Base Metal
CCT	Continuous Cooling Transformation
CGHAZ	Coarse-Grained HAZ
CTOD	Crack Tip Opening Displacement
DBTT	Ductile-Brittle Transition Temperature
EBSD	Electron Backscatter Diffraction
ECCI	Electron Channelling Contrast Imaging
FCC	Face-Centered Cubic
FGHAZ	Fine-Grained HAZ
FPSO	Floating, Production, Storage and Offloading
FZ	Fusion Zone
G-T	Greninger-Troiano
GMAW	Gas Metal Arc Welding
GND	Geometrically Necessary Dislocations
HAZ	Heat-Affected Zone
HSLA	High-Strength Low-Alloy
IC-CGHAZ	Intercritically reheated CGHAZ
ICHAZ	Intercritical HAZ
IPF	Inverse Pole Figure
K-S	Kurdjumov-Sachs
KAM	Kernel Average Misorientation
LBZ	Local Brittle Zones
LNG	Liquefied Natural Gas
LOM	Light Optical Microscopy
M-A	Martensite-Austenite
N-W	Nishiyama-Wasserman
OR	Orientation Relationship

PAG	Prior-Austenite Grain
PMTC	Phenomenological Theory of Martensite Crystallography
SC-CGHAZ	Subcritically reheated CGHAZ
SCHAZ	Subcritical HAZ
SCR-CGHAZ	Super-critically reheated CGHAZ
SEM	Scanning Electron Microscopy
TEM	Transmission Electron Microscopy
TRIP	Transformation Induced Plasticity
UA-CGHAZ	Unaltered CGHAZ
UTS	Ultimate Tensile Strength
YS	Yield Strength

CONTENTS

1 INTRODUCTION

Steels with 9 wt.% Ni and low carbon content have been widely used in applications that demand good toughness at cryogenic temperatures. During the 1940s, the interest in storage liquefied gases resulting from the extraction and refinement of petroleum stimulated the development of a family of low-carbon nickel-alloyed steels, aiming to optimise some features, such as toughness at cryogenic temperatures, weldability, and profitability. Continuing research on this family of steels led to the development of 9Ni steel, which, since the 1960s, has been adopted by the oil & gas industry as the primary material for Liquefied Natural Gas (LNG) storage and transportation.

Presenting a Ductile-Brittle Transition Temperature (DBTT) as low as -196 °C, 9Ni steels stand out as an excellent option for a wide range of cryogenic applications, being recently applied on the top side portion of supercritical CO_2 injection systems in deepwater oil fields. This process mitigates the emission of CO_2 while improving wells' efficiency through oil recovery. The transport of CO_2 in a liquid or supercritical state demands the application of high pressures, scaling up to 550 bar. In this scenario, any depressurisation event caused by cracking or any malfunction in the flange sealing ring may cause a sudden decrease in temperature, reaching values as low as -90 °C, which would promote the embrittlement of most Body-Centered Cubic (BCC) structural steels, such as the API 5L X65 steel pipes – widely applied in the oil & gas industry.

A challenge to this application is related to the welding of the 9Ni steel pipes to manufacture of the injection system. Due to the large wall thickness of these pipes, the welding process must follow a multi-pass approach, resulting in an essentially martensitic HAZ with microstructural heterogeneities introduced by the superposition of welding heat cycles. These heterogeneities are mainly related to the size and morphology of microconstituents and the fraction and distribution of secondary phases. It has been reported that the multi-pass welding can introduce LBZ in 9Ni steels HAZ, which would be related to variations in faction and chemical composition of constituents, such as retained/reversed austenite or Martensite-Austenite (M-A) particles.

Along with the aspects associated with these constituents, other microstructural features may also impact the mechanical properties of 9Ni steels. The retained austenite has been classically categorised as the most significant microconstituent for toughness improvement in 9Ni steels, which many authors classify as TRIP steel, proposing that the martensite transformation

induced by strain would enhance plasticity by the introduction of deformation mechanisms. However, recent studies revealed that austenite content might not follow a positive correlation with the toughness of Ni-alloyed lath martensite steels. Also, reports from the Welding Research Technology Laboratory of the *Universidade Federal do Ceará* show that the area fraction of stabilised austenite in the HAZ of 9Ni steel welds varies between 2 and 8%, fractions that were considered too low to ensure improvement in fracture toughness at cryogenic temperatures.

Recent papers point out the martensite morphology heterogeneity as one major factor in determining mechanical properties of lath martensite steels – such as the 9Ni steel. This heterogeneity is related to the presence of coarse martensite laths (presenting widths of up to 5 μm) within a matrix of thin martensite laths (with widths between 50 and 500 nm). These coarse laths act as soft zones within a much harder matrix of thin martensite laths. Regarding the plasticity, the mechanical properties heterogeneity associated with the coarse martensite laths would act in scattering local yield strength within the microstructure. It is expected that the deformability of these constituents would be enhanced when compared to the matrix, motivating an interpretation inspired by nano-composite structures. Most studies on lath martensite morphology heterogeneity are conducted over heat-treatment conditions, while just a few approach the influence of this microstructural aspect on welded joints' mechanical properties. Although coarse martensite laths have already been identified at the HAZ in the welding of low-carbon Ni-alloyed steels, their influence on mechanical properties and the strain mechanisms acting in these constituents have not been appropriately evaluated under the welding metallurgy perspective.

In this context, blurred relationships, regarding the compositional, microstructural and mechanical aspects of these advanced steels for cryogenic applications, has been noticed, being even more evident when analysing the welding of the 9Ni steels. Since this manufacturing process imposes a complex HAZ, its investigation on the mechanical behaviour of its microconstituents demands the application of mechanical tests associated with advanced microstructural characterisation techniques. The present study continues the work initially developed by the research staff of the Welding Research Technology Laboratory of the *Universidade Federal do Ceará*, which conducted an extensive investigation of the Gas Metal Arc Welding (GMAW) of 9Ni steel pipes applied on liquefied CO_2 injection systems.

1.1 Objectives

Here, is proposed a detailed microstructural investigation on the HAZ of previously obtained welds, mapping the mechanical properties at a micro-scale and evaluating the microstructure evolution through EBSD analyses on progressively deformed specimens subjected to tensile loading, correlating the microstructural features with the mechanical behaviour of the weld during plastic deformation.

1.1.1 Specific objectives

1. To characterise and assess micromechanical properties of the different HAZ regions introduced by the reheating cycles of the multi-pass welding process, evaluating the strengthening mechanisms acting on those regions.
2. To identify the morphology heterogeneity observed in the lath martensite microstructure, evaluating the contribution of coarse martensite lath to the plasticity and the mechanical properties of the HAZ of 9Ni steel girth welded pipes.
3. To assess how the heat-input applied in the welding process may affect the HAZ regions and its microconstituents and, consequently, the performance of the evaluated 9Ni steel welds.

1.2 Thesis structure

This thesis is divided into three main chapters, which will cover the proposed objectives, aiming to partially fulfil the requirement for the degree of Master in Materials Science and Engineering.

Chapter 2 reviews the concepts that underlie the research associated with this thesis and presents the state-of-the-art for the lath martensite microstructural features. An overview of the metallurgical aspects of lath martensite steels – focusing on 9Ni steel – is presented along with the singularities related to the welding metallurgy of these materials, covering the impacts on the HAZ associated with the thermal cycles to which the steel is submitted in arc welding processes.

Chapter 3 is written as a research paper, presenting a study that aims to conduct a detailed microstructural investigation through the different HAZ regions, using an extensive microhardness mapping on the HAZ of 9Ni steel pipes multi-pass girth welds as a reference,

identifying microstructural features that correlate to the local mechanical responses.

Chapter 4 presents a second research paper. The study aims to clarify the contribution of coarse martensite lath to the plasticity and the mechanical properties of the HAZ of 9Ni steel girth welded pipes, evaluating the strain evolution during the plastic deformation of the welded joint.

Finally, Chapter 5 summarises the conclusions and contributions of both papers presented in Chapters 3 and 4.

2 LITERATURE REVIEW

This chapter presents a review of the concepts that underlie the research associated with this thesis. Sections 2.1 and 2.2 present the challenges and historical contexts related to high toughness structural steels development, focusing mainly on 9Ni steel. Section 2.3 addresses the metallurgy of 9Ni steels discussing the constituents of its martensitic microstructure, which are presented and detailed in Subsections 2.3.1 and 2.3.2. Finally, Section 2.4 presents the singularities related to the welding metallurgy of 9Ni steels, focusing on the HAZ associated with the thermal cycles to which the material is submitted in arc welding processes.

2.1 Toughness and ductile-brittle transition

In the development of structural steels, it is usually aimed at the obtainment of a high mechanical strength combined with good toughness, a goal that appears to be contradictory since, in general, steels with greater strength have lower ductility are less tolerant to discontinuities and more susceptible to fracture (MORRIS *et al.*, 2001).

Balancing the trade-off between mechanical strength and toughness is a recurrent challenge in metallurgy. A specific case is the selection of structural steels for application at cryogenic temperatures, where the occurrence of a ductile-brittle transition will hamper the balance of these properties.

Steels with BCC crystal structure may significantly lose their ductility and toughness when subjected to temperatures below the DBTT. In this condition, the steel may be subjected to a brittle fracture, being either an intergranular fracture or a fracture by cleavage (transgranular fracture), as indicated in Figure 1a.

The ductile-brittle transition phenomenon is oversimplified by the Yoffee's diagram, presented in Figure 1b as an idealised representation of a ductile or brittle fracture that would occur at the tip of a pre-existing crack. For a ductile fracture to occur, the material must undergo yield, initiating the plastic deformation mechanisms. Thus, in a situation where the yield stress, σ_y, is greater than the brittle fracture stress, σ_f, there will be no plastic deformation, causing a brittle fracture. The "yield stress" is defined as the maximum stress in the plastic zone at the crack tip and is proportional to the material's yield point, while brittle fracture stress corresponds to the lowest stress associated with brittle fracture (MORRIS, 2011).

Yoffee's diagram indicates the DBTT at the intersection of the yield stress and brittle

fracture stress curves as a function of temperature, suggesting two generic ways to decrease the DBTT: by reducing the effective yield stress – an undesirable procedure for structural steels – or by raising the brittle fracture stress by controlling the risks of intergranular and transgranular fractures (MORRIS, 2008).

Figure 1 – Schematics of results from impact tests on different temperatures, revealing a DBTT (a). Yoffee's diagram representing the reduction in DBTT from the increase in brittle fracture stress (b).

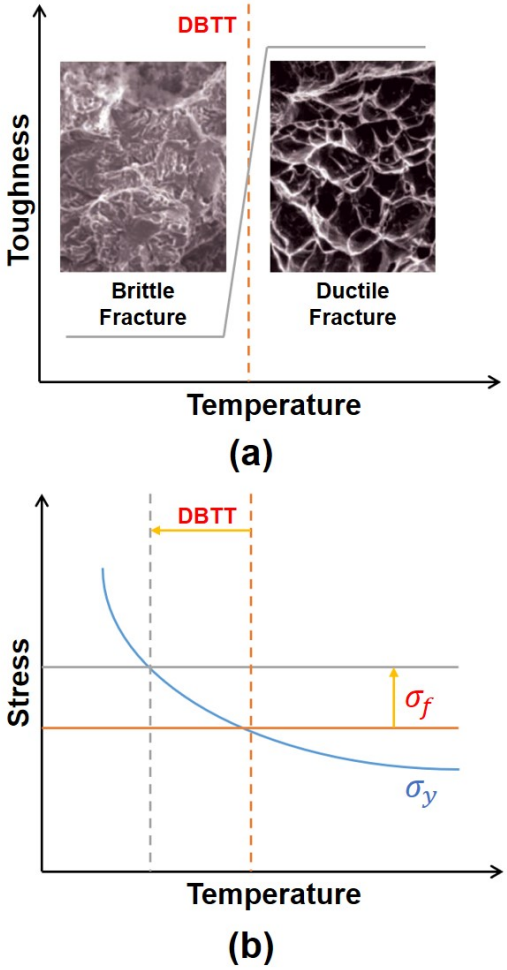

Source: Modified from Morris (2008).

To reduce the risk of intergranular fracture, the grain boundaries must be clean of impurities such as phosphorus and sulfur. As for the risk of transgranular fracture, it is commonly mitigated by the refinement of the effective grain size, that is, the reduction of the free path travelled by a crack until it meets a crystallographic discontinuity that prevents its propagation (MORRIS, 2011).

Good toughness has been achieved in high-strength steels with lath martensite

microstructure. The lath martensite – discussed in depth in Subsection 2.3.1 – has a high density of interfacial defects, presenting a small effective grain size capable of controlling the extent of cleavage of atomic planes, increasing the brittle fracture stress, thus reducing the DBTT (MORRIS *et al.*, 2013). Currently, most steels proposed for low-temperature and cryogenic applications are lath martensite steels, ranging from classic alloys such as AISI 4340 to Ni-alloyed cryogenic steels such as 9Ni steel.

The addition of Ni as an alloying element is an effective practice for reducing DBTT in steels, being recognised since the beginning of the 20th century (PENSE; STOUT, 1975). The Ni ability to improve low carbon steel properties at cryogenic temperatures is associated with several experimental observations that are mainly related to microstructure, such as the formation of martensitic structures with small effective grain size (MORRIS *et al.*, 2013) and the retention of thermodynamically stabilised austenite (STRIFE; PASSOJA, 1980).

2.2 9Ni steels

Steels containing 9 wt.% Ni and low carbon content have been widely utilised in applications that demand good toughness at cryogenic temperatures. During the 1940s, the interest in the storage of gases – in the liquid phase – resulting from the process of extracting and refining oil stimulated the development of a family of Ni-alloyed steels with low carbon content, seeking to optimise toughness at cryogenic temperatures, weldability, and economic factors (LIPPOLD *et al.*, 2011).

In this family, steels with 3.5 wt.% and 5 wt.% of Ni content were initially developed, being soon applied in the manufacture of LNG storage tanks. However, during service, a failure with safety consequences was reported for these tanks in Cleveland, Ohio, in 1944, in a steel tank of 3.5 wt.% Ni steel, a material whose properties are currently known as inadequate for this operation (PATEL, 2000). This event motivated the extension of researches on nickel-linked low-carbon steels, leading, in 1947, to the development of 9Ni (ARMSTRONG; BROPHY, 1947) steel, which from the 1960s onwards was adopted by the industry as the primary material for the manufacture of LNG storage tanks (PATEL, 2000).

Armstrong and Gagnebin (1940) studies point to a decrease in the DBTT of steels with low carbon content along with the increase in the Ni content of these materials. Figure 2 indicates a significant drop in DBTT with the increment of Ni content in low carbon steels, reaching a point where a ductile-brittle transition is not observed from compositions with 13

wt.% of Ni (LIPPOLD *et al.*, 2011).

Figure 2 – Effect of Ni content on the toughness of low carbon steels. Results based on Charpy impact test.

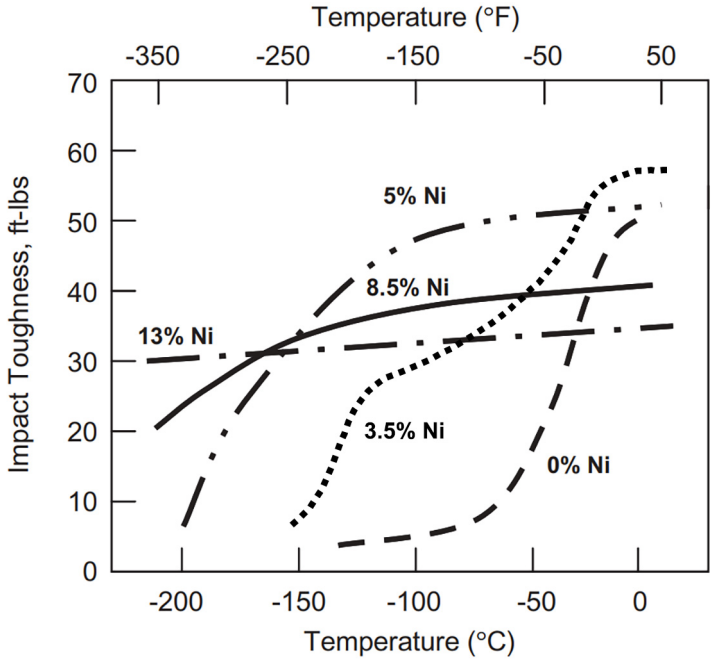

Source: Modified from Lippold *et al.* (2011), original from Armstrong and Gagnebin (1940).

9Ni steels have a sufficiently low DBTT for cryogenic applications, being capable of working at temperatures as low as −196 °C (SCHEID *et al.*, 2016). Commonly applied in LNG transport and storage, 9Ni steels have recently been applied in reinjection systems of liquefied CO_2 in oil reservoirs (FARIAS *et al.*, 2018), a process that has been carried out in deepwater oil fields, such as the Lula pre-salt oil field, in Brazil (BELTRÃO *et al.*, 2009). To be transported in the liquid phase, CO_2 must be subjected to pressures high above 500 bar (KNOOPE *et al.*, 2013). In this case, a sudden depressurisation caused by any local fault will promote an abrupt temperature drop reaching values around −100 °C (MAHGEREFTEH; ATTI, 2006).

Although the properties of 9Ni steels have been known for a long time (especially their toughness to fracture), the correlation between mechanical properties and microstructural observations still generates uncertainties and, in some cases, controversies. Presenting a microstructure composed essentially of martensite in laths, these steels have, for decades, raised discussions about several observed microstructural aspects, such as the effects of microstructural interfaces, morphological heterogeneities, and the presence and decomposition of second phases.

2.3 Physical metallurgy of 9Ni steels

9Ni steels, such as the ASTM A333 Gr. 8 steel studied in this thesis, are, in their manufacturing process, submitted to heat treatments to control the microstructure and to acquire the desired mechanical properties. These treatments involve the steel's normalisation, quenching and tempering (ASTM, 2018), resulting in a predominantly martensitic microstructure.

Presenting a microstructure characterised by a martensite matrix with lath-like morphology, 9Ni steels are classified by several authors as a lath martensite steel (MORITO *et al.*, 2003; MORRIS, 2011; KINNEY *et al.*, 2014; MORSDORF *et al.*, 2015). Despite being chaotic at first sight, the microstructure of these steels is strongly related to a hierarchical organisation, presenting a high density of interfaces with different levels of misorientation, in addition to presenting precipitates, considerable fractions of stabilised austenite, and other singularities addressed in this Section.

2.3.1 Lath martensite

Characterised by a high hardenability, 9Ni steels exhibit an essentially martensitic microstructure after being subjected to a wide range of thermal cycles. Aiming to draw an experimental Continuous Cooling Transformation (CCT) diagram for a 9Ni-Cr-Mo-V-0.11C steel, Fonda and Spanos (2014) verified a remarkable insensibility to cooling rate variations in quenching treatments. After austenitization at 1200 °C, the authors observed a microstructure constituted of lath martensite, which maintains considerable similarity from high cooling rates, such as 130 °C/s, to cooling rates as low as 0.16 °C/s, as shown by the micrographs in Figure 3, where the notation $\Delta t_{8/5}$ indicates the cooling time from 800 °C to 500 °C.

The crystallographic description of the martensitic transformation in steels is marked by the initial work of Bain and Dunkirk (1924), which built the foundations for the conception of the Phenomenological Theory of Martensite Crystallography (PMTC) during the 1950s (BOWLES; MACKENZIE, 1954). The PMTC considers two essential aspects of the martensitic transformation: the correspondence between the crystal lattices of the austenite (parent phase) and the martensite, and the preservation of the invariant plane according to the final martensite morphology (lath or plate). The martensitic transformation occurs through the Bain deformation, a simple shear motion, and a rigid body rotation (ARCHIE *et al.*, 2018). Figure 4 shows a schematic of the Bain deformation acting on the austenite crystal. In Figure 4a, there are a pair of

Face-Centered Cubic (FCC) cells corresponding to the austenitic structure, whose union provides the emergence of a Body-Centered Tetragonal (BCT) cell as highlighted in Figure 4b. The BCT cell (Figure 4c) transforms into the BCC cell of Figure 4d through the distortion corresponding to the Bain deformation, where the initial FCC cell undergoes compression of about 23% on one of the orthogonal axes and an expansion of about 12% on the remaining two axes, resulting in a volumetric expansion. Then, simple shear and rigid body rotation movements are responsible for reducing the network energy to tolerable levels (MORRIS, 2011).

Figure 3 – Light micrographs 9Ni-Cr-Mo-V-0.11C steel samples subjected to quenching in different cooling rates. 130 °C/s (a), 66 °C/s (b), 8.2 °C/s (c), 1.3 °C/s (d), and 0.16 °C/s (e).

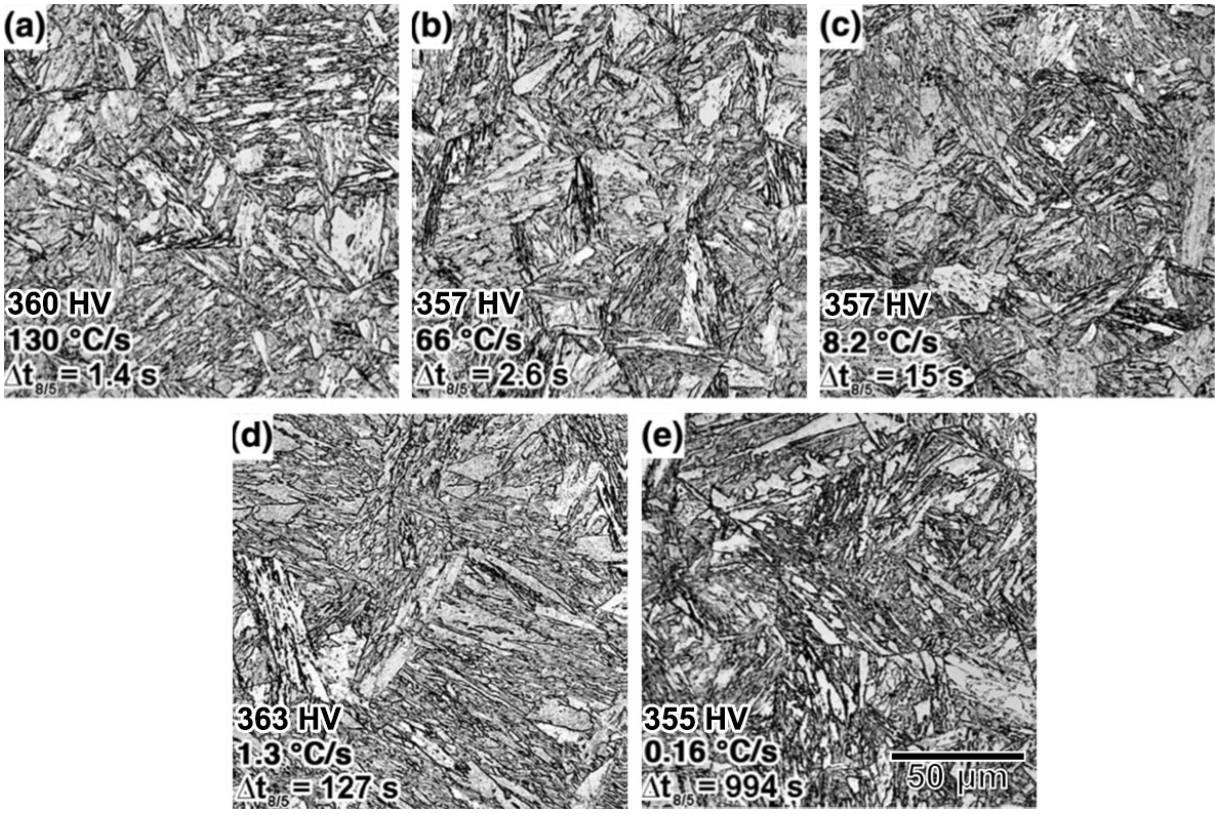

Source: Modified from Fonda and Spanos (2014).

The correspondence between the parent crystal lattices and the product phases, as a result of the atomic movements inherent to the martensitic transformation, conceives an Orientation Relationship (OR) between the austenite, γ, and the martensite, α'. In order to describe the OR between these phases, multiple models were proposed, such as the three most notable models for ferrous martensite: Kurdjumov-Sachs (K-S) (KURDJUMOV; SACHS, 1930), Nishiyama-Wasserman (N-W) (NISHIYAMA, 1934; WASSERMANN, 1935), and Greninger-Troiano (G-T) (GRENINGER; TROIANO, 1949) ORs. All these three models may be described by the parallel planes $\{111\}_{\gamma} || \{101\}_{\alpha'}$, which is associated with the invariant plane of the

transformation, and by the directions $\langle 1\bar{1}0\rangle_{\gamma} || \langle 11\bar{1}\rangle_{\alpha'}$ on the parallel planes. These parallel directions are oriented at an angle θ from each other, with values equal to 0° for the K-S OR, 2.5° for the G-T OR, and 5.26° for the N-W OR (KELLY, 1992; ARCHIE *et al.*, 2018).

Figure 4 – Pair of austenite FCC unit cells (a) forming a BCT cell (b) which, after Bain deformation (c-d), becomes a BCC cell. The subscript F is indicative of the FCC crystal lattice, while the B is indicative of the BCC crystal lattice.

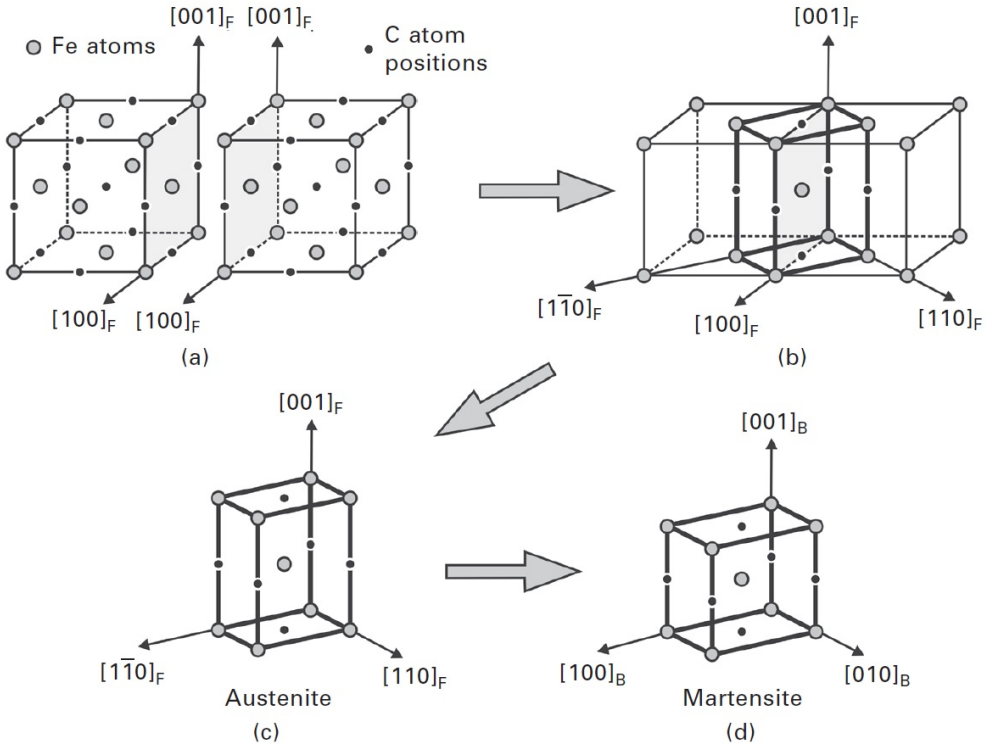

Source: Archie *et al.* (2018).

Each of the ORs will produce a set of variants according to the combinations of planes and directions of the families highlighted in the previous paragraph. Lath martensite and its parent phase follow an OR very close to G-T; however, favouring simplifications, it is common for authors to use the K-S OR to crystallographically describe the lath martensite (MORITO *et al.*, 2006). In the K-S OR, a total of 24 variants are observed, resulting from the four equivalent planes of the family $\{111\}_{\gamma}$ in combination with the six possible combinations of the parallel directions $\langle 1\bar{1}0\rangle_{\gamma} || \langle 11\bar{1}\rangle_{\alpha'}$. Table 1 presents the KS variants for the parallel planes $(111)_{\gamma} || (011)_{\alpha'}$, which are labelled according to the work of Morito *et al.* (2006). The remaining variants refer to the equivalent planes that form the same parallel relationship $\{111\}_{\gamma} || \{101\}_{\alpha'}$ and therefore follow a pattern similar to the six variants shown in Table 1. Figure 5 illustrates the relationship between variants V5 and V6 of the K-S OR, which are twin-related.

Table 1 – K-S variants for the parallel planes $(111)_\gamma || (011)_{\alpha'}$.

Variant	γ direction	α' direction
V1	$[\bar{1}01]_\gamma$	$[\bar{1}\bar{1}1]_{\alpha'}$
V2	$[\bar{1}01]_\gamma$	$[\bar{1}1\bar{1}]_{\alpha'}$
V3	$[01\bar{1}]_\gamma$	$[\bar{1}\bar{1}1]_{\alpha'}$
V4	$[01\bar{1}]_\gamma$	$[\bar{1}1\bar{1}]_{\alpha'}$
V5	$[1\bar{1}0]_\gamma$	$[\bar{1}\bar{1}1]_{\alpha'}$
V6	$[1\bar{1}0]_\gamma$	$[\bar{1}1\bar{1}]_{\alpha'}$

Source: Morito *et al.* (2006).

K-S variants behaviour is a determining factor for the microstructural organisation of lath martensite. Characterised by a hierarchical organisation, the microstructure of lath martensite steels can be partitioned into substructures whose crystallographic orientations define a hierarchy of misorientation levels, which is directly related to the K-S variants.

2.3.1.1 Hierarchical structure

Although the morphological characterisation of lathed martensite dates back to the early 1970s (KRAUSS; MARDER, 1971), it was only at the beginning of the 21st century that the accessibility to the EBSD technique allowed considerable clarification about the microstructural elements that constitute this morphological class.

Lath martensite is subdivided into structural units: Prior-Austenite Grain (PAG), martensite packets, martensite blocks, and martensite laths. Figure 6a presents the large-scale units, indicating the boundaries relate to PAG, martensite packets, and martensite blocks, while Figure 6b exhibit the martensite laths, nanometric structures of low misorientation, which represent the smallest structural unit of lath martensite.

To understand the hierarchical organisation of lath martensite, it is necessary, initially, to observe the crystallographic orientation of the martensite laths. Consisting of the fundamental component of the martensitic microstructure, martensite laths are single crystals composed of a single K-S variant. As its nomenclature suggests, this constituent is characterised by its lath-like morphology, with width varying from 50 nm to 500 nm (MORSDORF *et al.*, 2015). Furthermore, as Figure 6b indicates, the neighbouring laths establish a non-cumulative low misorientation between each other (MORITO *et al.*, 2006).

Figure 5 – Representation of the relationship between the V5 and V6 variants and the γ phase according to the parallelism $(111)_{\gamma} || (011)_{\alpha'}$.

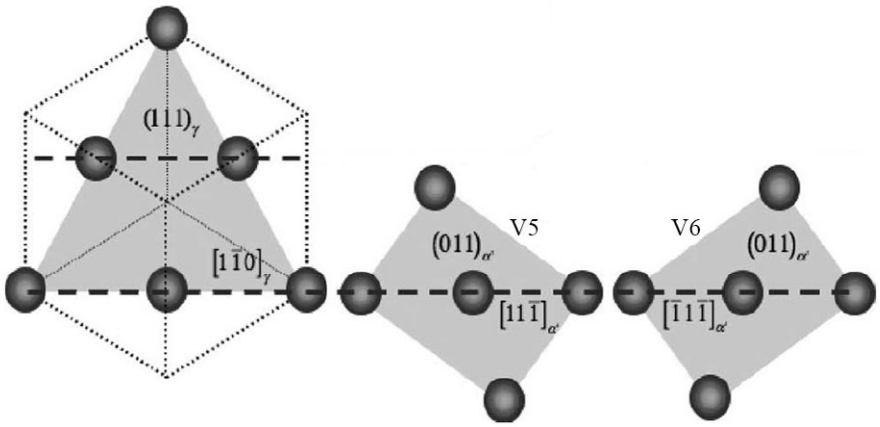

Source: Modified from Morris (2011).

An agglomerate of laths that share the same K-S variant constitutes a substructure defined as a sub-block, according to Morito *et al.* (2006). The identification of this substructure requires the application of EBSD techniques, as shown in Figure 7, where the regions of homogeneous colour on the orientation maps are identified as sub-blocks, indicating that those regions are composed of laths of just one of the six highlighted K-S variants, labelled according to Table 1.

Figure 7 also highlights the martensite blocks, labelled as B1, B2, and B3. A notable feature of the martensite blocks is the bivariant character of these structures, formed by well-defined pairs of K-S variants. As shown in Figure 7, these pairs are V1-V4, V2-V5 and V3-V6. Morito *et al.* (2006) highlight that these pairs guarantee the least possible misorientation among all K-S variants pairs, attributing this factor to the observed configurations. Kinney *et al.* (2014) point out that the thermodynamic advantage of the bivariant character of the martensite blocks is strongly related to favourable conditions concerning internal strain and surface energy. The configuration of these blocks results in a strained network equivalent to a simple tetragonal strain (MORRIS, 2011).

As seen in Figure 6a, a set of blocks composes the microstructural constituent identified as a martensite packet. A packet is composed of a cluster of blocks developed over the same invariant plane $\{111\}_{\gamma}$, where it is possible to observe all the three types of blocks presented in Figure 7. Consequently, packets can be identified as regions where the martensite laths are "stacked" on the same plane $\{011\}_{\alpha'}$ (MICHIUCHI *et al.*, 2009; KINNEY *et al.*, 2014).

Thus, four crystallographically distinct packets configurations could be observed in a single PAG, as verified in Figure 8, where all four configurations are observed inside a PAG, ensuring the presence of all 24 K-S variants in all grains analysed by Kinney *et al.* (2014) in a study performed over a 9Ni steel.

Figure 6 – Light micrograph revealing the boundaries relatives to PAG, martensite packet and martensite block (a). Transmission electron microscopy over a set of laths (A-G) in the same sub-block (b).

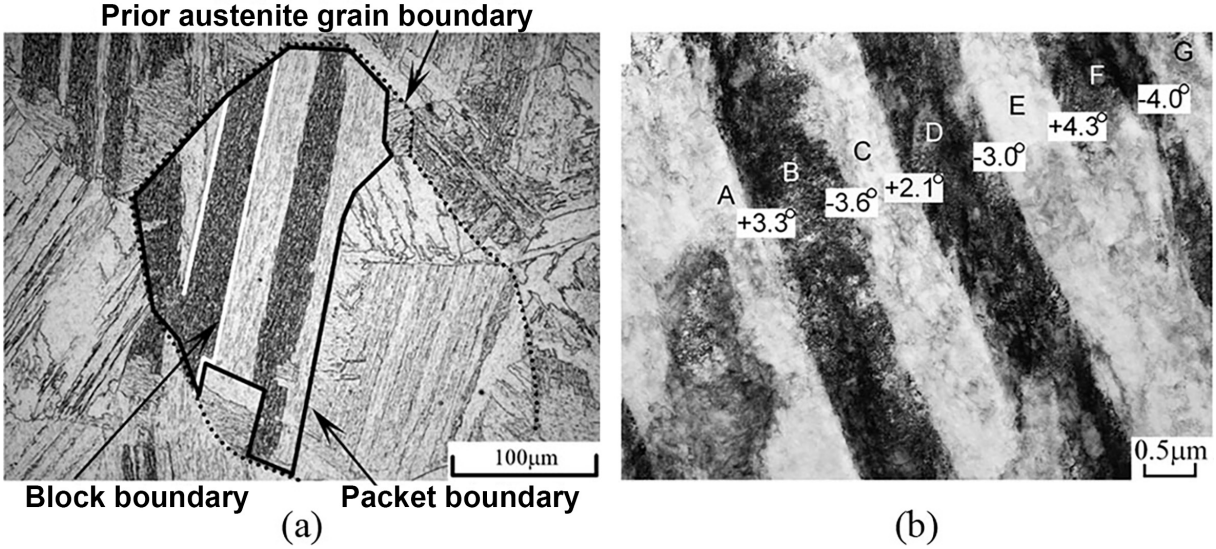

Source: Modified from Morito *et al.* (2006).

Packets are ideally composed of the three-block configurations present in equivalent fractions, so that the strained network of the martensitic transformation resembles a simple dilation, being easily accommodated by the polycrystalline matrix (MORRIS, 2011).

2.3.1.2 Morphological heterogeneity

In addition to the hierarchical constituents, many lath martensite steels – such as the Ni-alloyed low-carbon steels – are characterised by the presence of coarse microconstituents, free of interfacial defects in their interior, which have been just recently reported as important microconstituents for lath martensite plasticity (MORSDORF *et al.*, 2016).

These coarse structures are highlighted by the low Kernel Average Misorientation (KAM) indexed regions, indicated by the white arrows in Figure 9, which presents a mapping over the microstructure of Fe-0.13C-5Ni steel. Throughout the years, these constituents were reported in various studies, being labelled as martensite plates (FONDA *et al.*, 1994), coalesced bainite (BHADESHIA *et al.*, 2006; KEEHAN *et al.*, 2008) and, more recently, as coarse laths

(FONDA; SPANOS, 2014; MORSDORF *et al.*, 2015).

Figure 7 – Orientation maps obtained by EBSD on lath martensite steels, highlighting 3 different block configurations and 6 different K-S variants (a-b). Pole figures {100} exhibiting the crystallographic orientations corresponding to maps a and b, respectively (c-d).

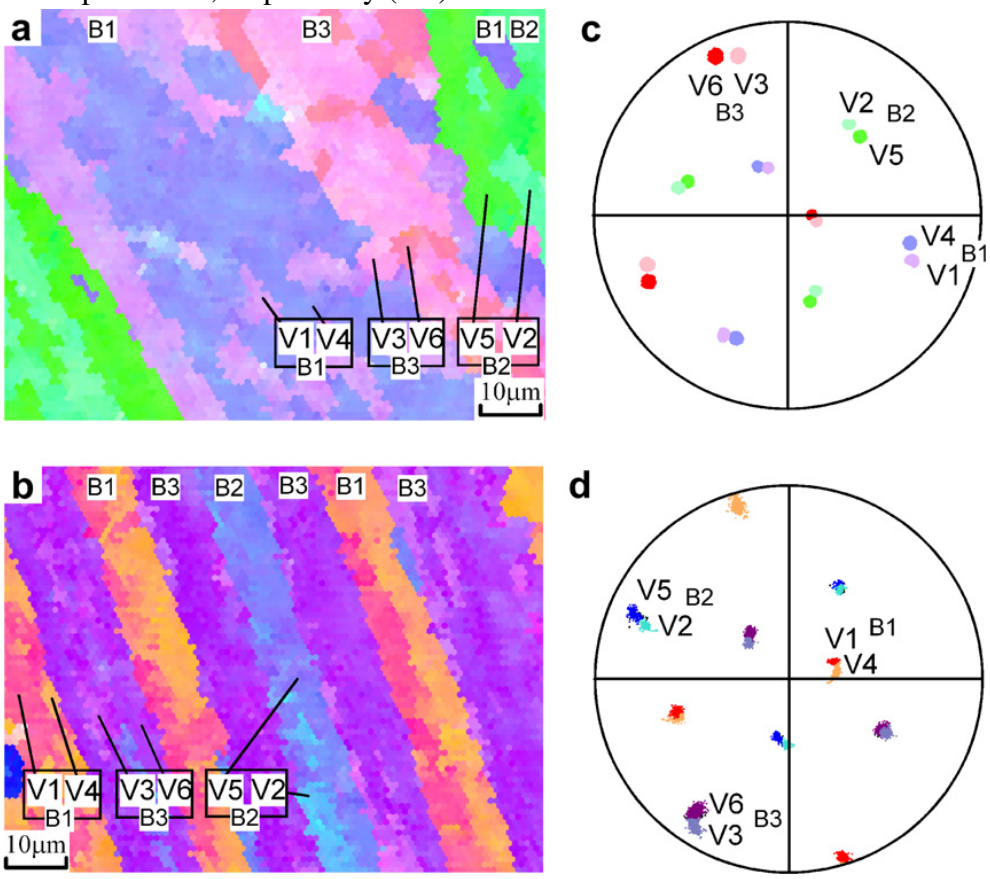

Source: Morito *et al.* (2006).

Fonda *et al.* (1994) were one of the first to observe and report the presence of a coarse martensite structure in their microstructural investigation over a High-Strength Low-Alloy (HSLA) steel subjected to thermal welding cycles simulations. Due to the limitations of two-dimensional microstructural observation, the authors characterised the structure as auto-tempered martensite with plate morphology, where remarkable precipitation of carbides is observed inside this constituent, as seen in Figure 10a.

Analysing a broad set of martensitic steels, Bhadeshia *et al.* (2006) described the formation of coarse constituents in a lath martensite matrix, labelling them as coalesced bainite. According to the author, sub-units, constituted by small bainite plates with the same crystallographic orientation, may coalesce into a coarse unit called coalesced bainite, which is shown in Figure 10b. This mechanism would be related to a high driving force associated with

reasonably slow cooling rates and lower free energy achieved by the coalescence into a single coarse structure. Later, through a three-dimensional characterisation of the coalesced bainite, Keehan *et al.* (2008) verified that the constituent presents a lath-like morphology.

Figure 8 – Orientation maps of PAG, revealing the presence of four crystallographically distinct configurations of martensite packets.

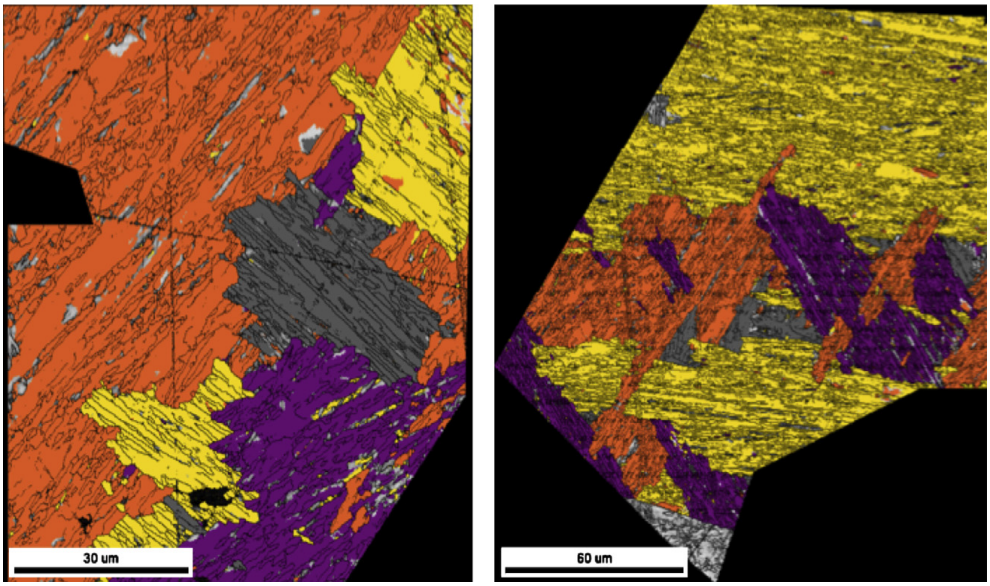

Source: Kinney *et al.* (2014).

In recent studies, Fonda and Spanos (2014) return to the characterization of these coarse constituents observed in a 9Ni steel, going against the hypothesis of bainite coalescence, labelling them as auto-tempered coarse martensite laths. The authors highlight two main reasons for characterising this structure as a martensite lath. The first one is the observation of these constituents over a wide range of cooling rates, even under severe cooling conditions, where diffusional transformations, such as the bainite formation, would be prevented. The other reason would be the presence of multiple orientation variants (typically three) of cementite, as highlighted in Figure 10c, indicating that this constituent was initially formed as a supersaturated phase, with the cementite precipitation occurring during the subsequent cooling, depending on the cooling rate imposed by the heat treatment. However, the authors do not rule out the possibility of coalescence of martensite sub-units as a mechanism for coarse lath formation.

An extensive microstructural characterization of lath martensite, especially on coarse laths, was carried out by Morsdorf *et al.* (2015) in a study over a Fe–0.15C–5Ni alloy. The authors observed microstructural heterogeneities related to morphology, chemical composition, and mechanical properties, as summarized by the schematic presented in Figure 11. In the schematic, the coarse laths are represented by structures characterised by a flat end connected

to the austenitic grain contour and by their growth towards the centre of the grain, assuming a wedge shape that would extend over a depth that could be greater than 4 μm (MORSDORF *et al.*, 2015).

Figure 9 – KAM over a Fe-0.13C-5N sample. The map is superimposed by PAG boundaries. White arrows indicate coarse constituents free of internal interfacial discontinuities.

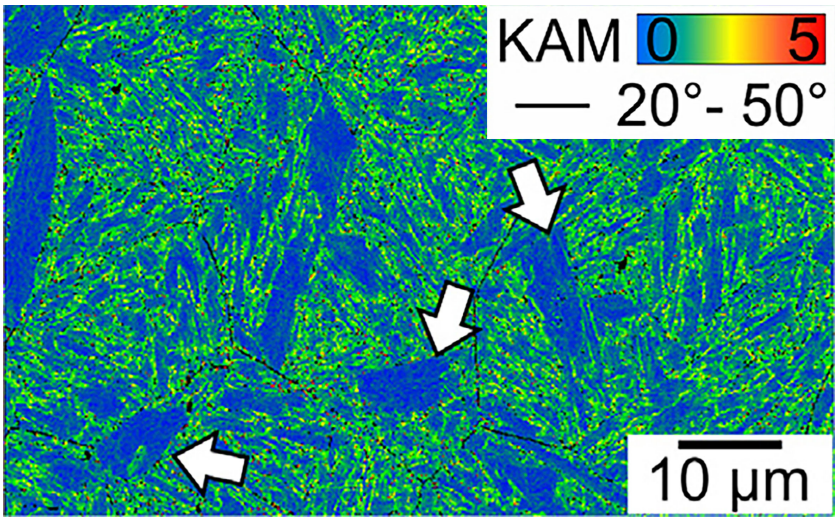

Source: Modified from Morsdorf *et al.* (2016).

Figure 10 – Reports on the coarse constituents within the microstructure of lath martensite steels, which were labeled as martensite plates (a), coalesced bainite (b), and coarse laths (c).

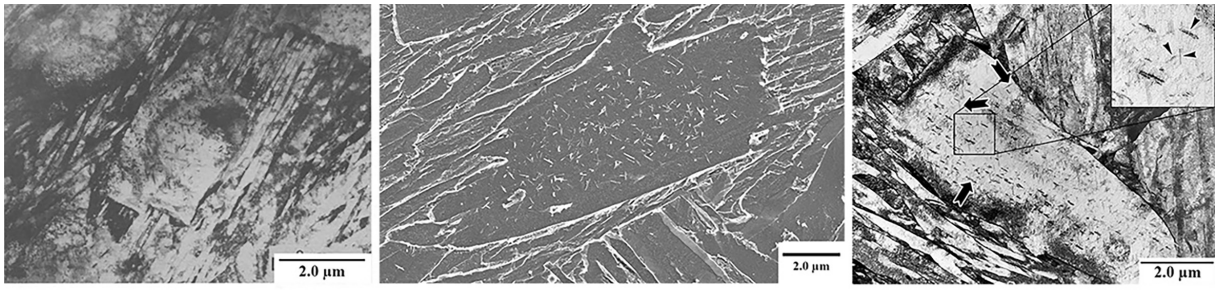

(a) **(b)** **(c)**

Source: Modified from Fonda *et al.* (1994) (a), Bhadeshia *et al.* (2006) (b) and Fonda and Spanos (2014) (c).

The insertions in Figure 11 exhibit analyses based on Electron Channelling Contrast Imaging (ECCI) and Atom Probe Tomography (APT) techniques. ECCI analysis allows the evaluation of the density of dislocations, which are identified by the dark regions in the presented images, where it is possible to identify a lower dislocation density in coarse laths in comparison to regions composed of thin laths. The APT analyses seek to highlight the intense carbon segregation for the dislocations observed in coarse laths, while, for thin laths regions, the interstitial carbon distribution tends to assume a homogeneous behaviour. These differences

in microstructural features are reflected in the mechanical properties heterogeneity, which is schematically represented in Figure 11 through the local Yield Strength (YS) scale, indicating the coarse laths as soft zones inside a matrix of thin laths of greater hardness, a configuration that motivates an interpretation based on the analogy to nanocomposites (MORSDORF *et al.*, 2015).

Figure 11 – Schematic of the hierarchical structure of lath martensite, illustrating the mechanical heterogeneity related to lath size, dislocation density, and interstitial carbon distribution.

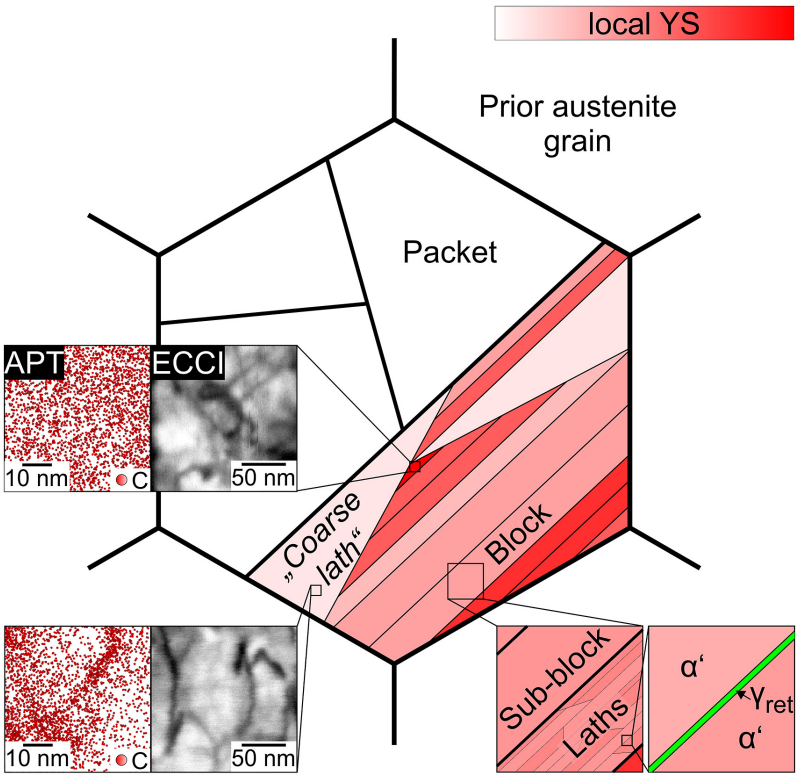

Source: Morsdorf *et al.* (2016).

Furthermore, the observations analysed by Morsdorf *et al.* (2015) enabled the conception of lath martensite transformation stages proposed by the authors and illustrated in Figure 12a. Strains introduced by the martensitic transformation are plastically accommodated by the neighbouring austenite, a phenomenon that plays a significant role in the morphological characteristics of lath martensite. In the first stages, at temperatures just above the martensite start temperature (M_S), the austenite is a soft constituent with low dislocation density, imposing a low resistance to the initial growth of martensite laths. Throughout the transformation, the remaining austenite strength progressively increases due to temperature decrease and the accommodation of accumulated dislocation due to the inherent strain of martensitic transformation. Therefore, the growth of new laths is hampered, especially in regions close to previously nucleated to coarse laths. When the austenite reaches a high defect density level, the nucleation of thin laths will be

auto-catalytically triggered, resulting in a microstructure composed of coarse laths in a matrix of thin laths.

Furthermore, at temperatures close to the martensite finish temperature (M_f), the austenite retained between the laths will be under a high constraint, stabilising itself. This high constraint level is also related to the internal twinning of some thin martensite laths (MORSDORF *et al.*, 2015), as indicated by the inset in Figure 12a. During cooling, the initially nucleated coarse laths undergo an auto-tempering, promoting the segregation of carbon inside this constituent, which becomes softer.

Figure 12 – Schematic of the martensitic transformation sequence with colour scale for dislocation density (a). Coarse lath fraction as a function of PAG size and C content (b). Histogram of the coarse lath fraction analysis colour-coded according to image b (c).

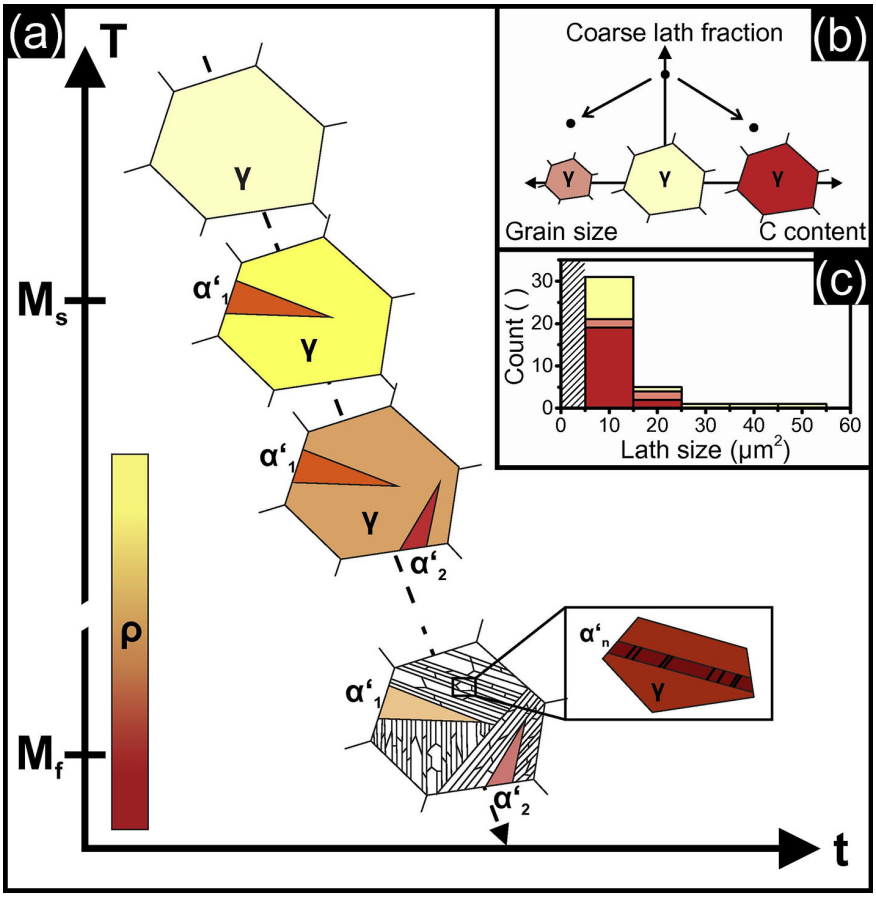

Source: Morsdorf *et al.* (2015).

Seeking comparative results, Morsdorf *et al.* (2015) also characterized steels with higher carbon content (Fe–0.3C–5Ni) and with smaller PAG size (Figure 12b), noting a drop in the coarse lath fraction for both cases, as shown in the histogram in Figure 12c. These results would be related to the lower M_s observed for the comparative samples, which results in an initial

austenitic structure of higher strength, imposing a higher resistance to the coarse lath growth.

2.3.1.3 Plastic strain

Plastic strain distribution in lath martensite results from a set of microstructural features, such as the crystallographic aspects, the interfaces of the martensitic microstructure, the morphology of the constituents, and the presence of retained austenite films (MORSDORF *et al.*, 2016).

Crystallographic aspects are related to the activation of slip systems associated with the plastic strain mechanism. Considering the slip systems of a BCC cell – $\{110\}\langle 111\rangle$ and $\{211\}\langle 111\rangle$ – and the geometric constraints of the microstructure, it is possible to use a binary classification, which refers to a slip system with Burgers vector parallel to the lath interfaces (in-lath-plane slip system) and a slip system with Burgers vector not parallel to the lath interfaces (out-of-lath-plane slip system) (MICHIUCHI *et al.*, 2009). Evaluating results from in-situ analysis and mathematical modelling based on Taylor and Sachs principles, Michiuchi *et al.* (2009) verified the preferential activation of the in-lath-plane slip system. Laths within a single martensite packet share the same geometric orientation; thus, the slip plane remains parallel along with the blocks that compose this packet. Despite this, the slip direction diverges between blocks, resulting in different Schmid factors and the consequent activation of different slip systems. This results in the heterogeneity of deformability between blocks of the same packet (MORSDORF *et al.*, 2016).

Concerning the influence of microstructural interfaces, it has been verified that intense plastic activity is observed in high-angle boundaries, such as block boundaries and packet boundaries. This observation is associated with the non-agreement between the slip systems acting in the regions adjacent to the interface. This behaviour results in a high level of stress associated with the accumulation of dislocations at those boundaries, responsible for the formation of slip steps (MORSDORF *et al.*, 2016). This phenomenon becomes even more evident when the shear stress acting on the interface plane is maximum, a condition observed in cases where the interface plane assumes an angle close to 45° with the applied load direction (DU *et al.*, 2016b). Thus, the topological inclination of boundary planes becomes a determining factor for the deformability of lath martensite so that packets with habit planes $\{011\}_{\alpha'}$ in different orientations will be subject to distinct deformation conditions.

The exposed features join the heterogeneities presented in the previous Subsec-

tion (heterogeneities related to constituents morphology, dislocation densities, and interstitial carbon distributions) to determine the plastic deformation character of the martensite at the microstructural level. These relationships are represented by Figure 13, which shows the deformation response resulting from a combination of factors that influence the deformability of lath martensite.

Figure 13 – Schematic representation of the combined factors that determine the microstructural deformability of lath martensite.

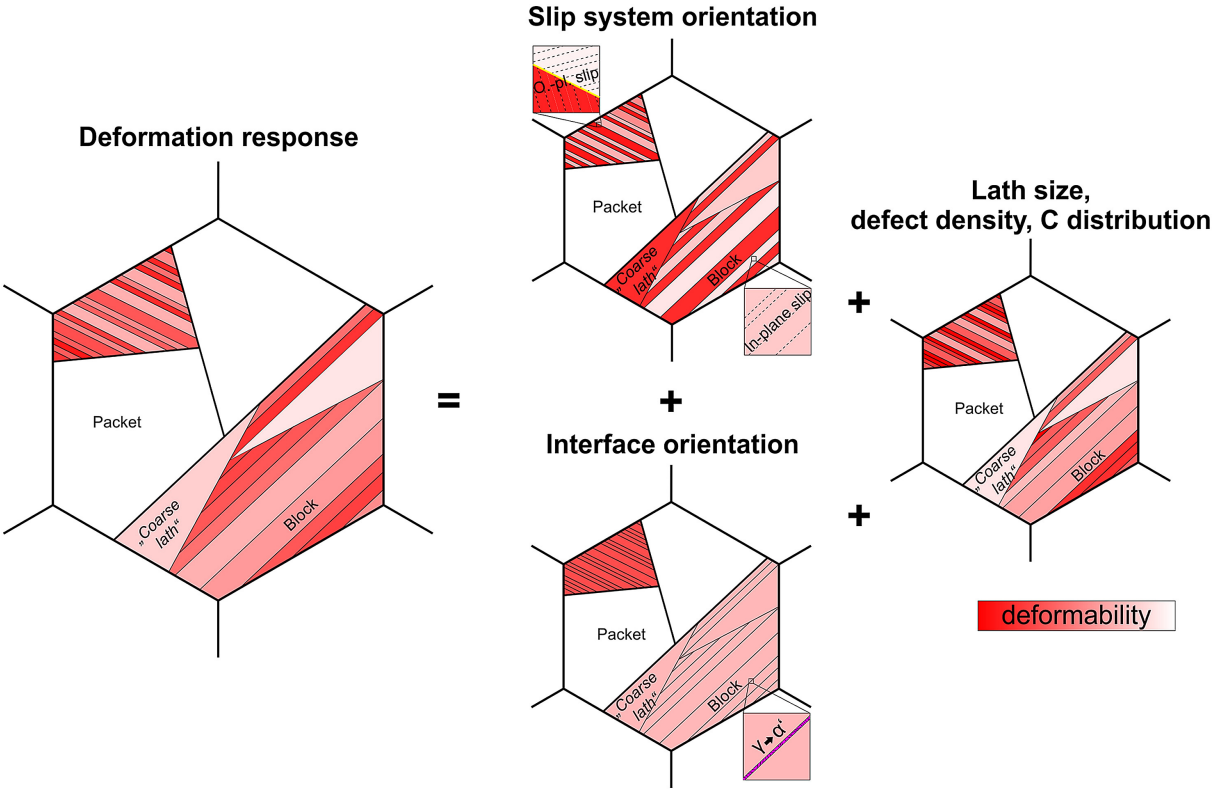

Source: Morsdorf *et al.* (2016).

The discussion of these fundamental mechanisms of lath martensite plasticity was only made possible in the last couple of decades, due to the broader access to tools and instrumentation – such as the scanning electron microscopes capable to perform detailed EBSD analyses – required to map complex crystallographic relations. Through the analysis of EBSD data, it is possible to quantify plastic strain via two different approaches: the first is based on the degradation of the diffraction patterns in strained materials and the second based on local misorientation analyses (WRIGHT *et al.*, 2011).

The local misorientation approach is based on the manifestation of residual strain as local variations in lattice orientation. The KAM stands out as the most popular among the different methods for characterising local misorientation. It is based on the average misorientation

between a point on a measurement grid (centred at each point of the scan) and its neighbours; However, to focus on small local rotations, the grain boundary effect is excluded by only including misorientations less than a specified tolerance (LEHOCKEY *et al.*, 2000; WRIGHT *et al.*, 2011). Figure 9 presents a KAM map, where the higher KAM values are indicative of areas of concentrated Geometrically Necessary Dislocations (GND) density.

GND are the result of strain gradients introduced by plastic deformation. Plastic strain may induce zones under tension and compression loads within the crystal lattice, creating differences in the number of atomic planes between each of these zones that are accommodated by introducing edge dislocations into the crystal. These are GND. In polycrystals, the strain gradient induced by plastic deformation may be accommodated by GND within each grain while also can providing compatibility of displacements between adjacent grains (COURTNEY, 2005). GND density maps can be estimated from EBSD orientation data by determining dislocation density tensor components from the misorientation measurements (PANTLEON, 2008). These maps are capable of identifying areas of concentrated strain within a microstructure.

Furthermore, the austenite films retained between microstructural interfaces also play a role in the plastic deformation mechanisms of lath martensite. Its contribution to plasticity, and other characteristics of the retained austenite, are presented in the following Subsection.

2.3.2 Retained/reversed austenite

The good cryogenic toughness of 9Ni steels has been attributed to the presence of some austenite fraction in its microstructure, being this subject reported and discussed for decades by many authors such as Marshall *et al.* (1962) and Zhang *et al.* (2013). Thus, quenching and tempering heat treatments at intercritical temperatures ($Ac_1 < T < Ac_3$) started to be commonly adopted in the manufacturing process of these alloys, aiming to achieve considerable precipitation and retention of austenite to obtain good toughness under cryogenic conditions (PENSE; STOUT, 1975).

The precipitation and the stabilization of austenite are related both to the diffusion of γ-stabilizers alloying elements, such as Ni and C, and to the high density of nucleating agents in the microstructure of lath martensite, such as lath, blocks, packets, and PAG boundaries. The execution of quenching heat-treatments at lower temperatures can potentiate the precipitation of austenite in a later intercritical tempering, which is related to the obtainment of a finer microstructure with more nucleating points. Furthermore, a tempering treatment at higher temperatures

will also contribute to the precipitation of austenite by promoting greater diffusibility of the γ-stabilizers alloying elements (YANG *et al.*, 2010).

After executing an intercritical tempering, it is common to observe austenite particles that precipitate along the PAG and lath boundaries (FULTZ *et al.*, 1985). The precipitation along the PAG boundaries is associated with the activation of the heterogeneous nucleation of reverse austenite (FULTZ *et al.*, 1986). The austenite precipitation along martensite lath boundaries, in addition to being related to precipitation on nucleating agents (such as lath boundaries), is associated with the presence of austenite initially retained in the martensitic microstructure (ZHANG *et al.*, 2013; JAIN *et al.*, 2017), which is stabilized at the end of the martensitic transformation due to the high constraint level and segregation of solute during transformation, enriching the austenite in γ-stabilizer elements (MORSDORF *et al.*, 2015). In tempering, the precipitation of reverse austenite occurs predominantly in Ni-rich martensite regions in the vicinity of the retained austenite films. Thus, favouring the retainment of austenite in previous quenching enhances the obtainment of higher austenite fraction in later intercritial tempering (JAIN *et al.*, 2017).

An example is the heat treatments in which an intercritical quenching is executed to ensure a higher initial fraction of retained austenite. Figure 14a presents a micrograph of Transmission Electron Microscopy (TEM), which indicates the intense precipitation of austenite observed in a 9Ni steel sample subjected to an intercritical tempering after the execution of an intercritical quenching. In contrast, Figure 14b presents the micrograph of a sample subjected to an intercritical tempering after the execution of a conventional quenching. It is possible to observe a remarkable increase in austenite fraction on the sample subjected to quenching at intercritical temperature (ZHANG *et al.*, 2013). Studies by Jain *et al.* (2017) on a 10 wt.% Ni steel report that the increase in the austenite volume fraction after intercritical tempering can be greater than 10% for samples subjected to previous intercritial quenching, while, for samples subjected to conventional quenching, this increase may reach 3%.

2.3.2.1 Role of retained austenite on the plastic strain

Evidence of high strain and ductile fracture observed in lath martensite steels (MINE *et al.*, 2013) exposes contradictions between the reported behaviour and the recognized brittle behaviour of the martensite phase. Results like these and the good cryogenic toughness of lath martensite steels have long been associated with the presence of austenite located between the

martensite laths (STRIFE; PASSOJA, 1980; AHSAN *et al.*, 2014). However, evaluating the interlath austenite behaviour in the face of plastic deformation becomes difficult due to the nanometric dimensions of these constituents, whose proper detection and resolution require TEM analysis.

Figure 14 – TEM micrograph of 9Ni steel samples submitted to intercritical temper after intercritical quenching (a) and submitted to intercritical temper after common quenching (b).

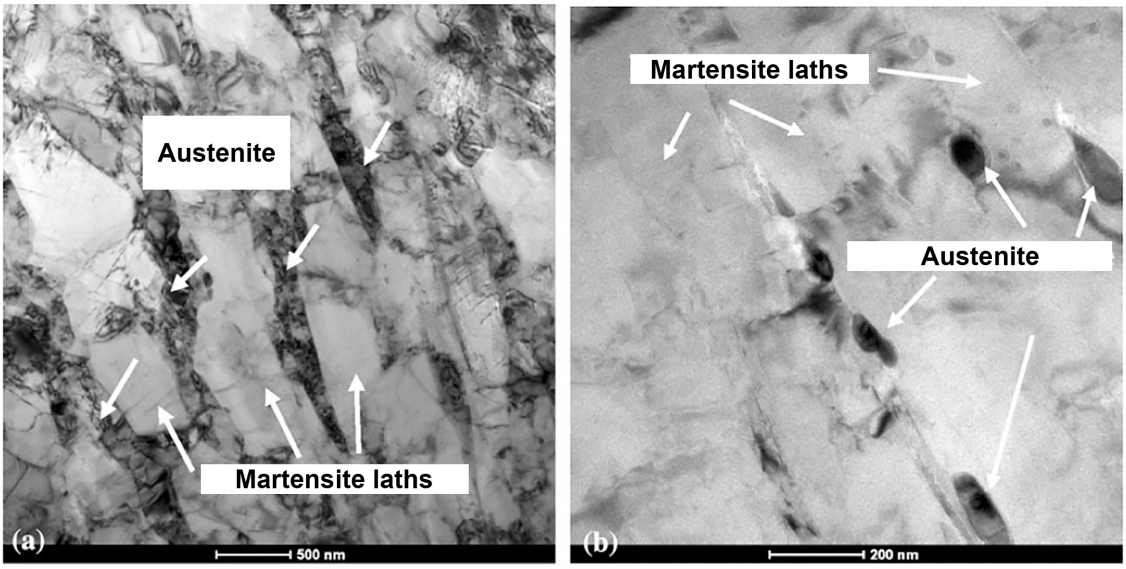

Source: Modified from Zhang *et al.* (2013).

Maresca *et al.* (2014) conducted a detailed study on the computational simulation of an anisotropic martensite laths model (BCC) considering the interlath retained austenite films (FCC), exploiting an approach in which the kinematics is governed by the slip systems of the single crystals. The authors reported intense shear along the laths habit plane, where the retained austenite films act as a "viscous plane" on which the adjacent laths would slide through. This behaviour would be associated not only with the flow stress in the austenite phase but also with the OR between the austenite and martensite phases, which establishes an approximately parallel orientation between the austenite slip plane, $\{111\}_{\gamma}$, and the habit plane of martensite laths, $\{011\}_{\alpha'}$.

On the other hand, Morsdorf *et al.* (2016) verified that, during the plastic deformation of a 5Ni steel, the austenite initially retained between the martensite laths is not detected at strain levels greater than 4%, indicating that the austenite undergoes a martensitic transformation induced by plastic deformation in the early plastic regime. Thus, the retained austenite volume fraction would not be a determining factor for the deformability of martensite in laths throughout

the whole plastic deformation process, but only in the initial stages.

Furthermore, some authors classify low-carbon Ni-alloyed martensitic steels as Transformation Induced Plasticity (TRIP) steels (ZHANG, 2012; ISHEIM *et al.*, 2013; JAIN *et al.*, 2018). From this perspective, the good toughness of these steels would be a consequence of the TRIP effect, which would be responsible for introducing deformation mechanisms associated with the transformation of retained austenite into martensite, which is induced by plastic deformation (OLSON; AZRIN, 1978). However, Barrick and DuPont (2019), in a study on the welding of 10Ni steels, found that the toughness of this material does not exhibit an expected strong and positive correlation with the volume fraction of retained austenite, indicating that other microstructural features would have a greater influence on the toughness of the investigated steel.

2.4 Welding metallurgy

Welding is arguably the most widely used manufacturing process, standing out in several scenarios. Be that as may, weldability[1] is desirable for an expressive majority of metallic alloys, such as structural steels. Despite that, the favouring of better weldability is commonly a detrimental factor to the high mechanical strength desired for these alloys. Thus, in the development of high-strength steels, aiming for a good balance between weldability and mechanical properties is an essential task for materials engineering.

In this scenario, 9Ni steels would not be an exception. Over the last few decades, studies focused on the welding metallurgy of these steels have been presented with high relevance, ranging from research on the deposition of weld metals with equivalent composition (MU *et al.*, 2018; MU *et al.*, 2019), to studies on transition zones (FARIAS *et al.*, 2018) and researches on the various microstructural features of the HAZ (JANG *et al.*, 1998; JANG *et al.*, 2002; FERNANDES *et al.*, 2020).

Following the objective of this thesis, this Section will focus on a review of the microstructural features of the HAZ resulting from the welding of 9Ni steels and their equivalent alloys, presenting reports on the microstructural characterisation and the mechanical properties evaluation of this sensitive zone.

[1] Weldability refers to the ability to carry out the welding process aiming to obtain a flawless structure while achieving the projected mechanical, chemical, physical, and metallurgical properties (BLACK; KOHSER, 2007).

2.4.1 Heat-affected zone

The arc welding heat source is characterised by its high-density energy, which is locally imposed over a small region compared to the dimensions of the welded structure. These conditions result in high heating and cooling rates, which severity will depend on the distance between the analysis point and the heat source, promoting non-equilibrium metallurgical transformations throughout a region whose peak temperatures range from values above the alloy's melting point to values equivalent to a given critical metallurgical transformation temperature. This region would comprise the FZ and the HAZ of the welded joint, the latter being defined as an unfused zone that underwent relevant metallurgical transformations (KOU, 2003).

Generally, in steel welding, the HAZ can be segmented according to the observed final microstructure and the peak temperatures reached along this zone. This segmentation is illustrated in Figure 15, which discriminates 3 HAZ regions: the CGHAZ, where austenitic grain growth occurs due to exposure to high critical temperatures ($T_f > T \gg Ac_3$); the Fine-Grained HAZ (FGHAZ), a region that was austenitized, but did not exhibit a significant grain growth due to exposure to lower critical temperatures ($T > Ac_3$); and the Intercritical HAZ (ICHAZ), region exposed to intercritical temperatures ($Ac_3 > T > Ac_1$), undergoing a partial austenitization, which usually promotes the precipitation of carbides and secondary phases (LIPPOLD *et al.*, 2015). Some authors discriminate a fourth HAZ region, the Subcritical HAZ (SCHAZ), a region that is subjected to tempering effects due to the exposure to subcritical temperatures ($Ac_1 > T$) (BHADESHIA; HONEYCOMBE, 2017).

The HAZ microstructure becomes even more heterogeneous in cases where the welding process is carried out through the deposition of multiple welding beads, promoting an overlap of thermal cycles imposed by the processing. In this situation, it is necessary to evaluate the microstructural impact the new thermal cycles will exert on the previously mentioned HAZ segmentation regions. The CGHAZ, for example, can be sub-segmented into four zones according to the reheating temperatures: SC-CGHAZ; IC-CGHAZ; SCR-CGHAZ, when reheating temperatures reach low critical values; Unaltered CGHAZ (UA-CGHAZ), when reheating temperatures reach high critical values – promoting grain growth – or no relevant reheating effect is observed (KIM *et al.*, 1991; BLONDEAU, 2013). This segmentation is illustrated in Figure 16, which schematically presents the microstructures of the zones mentioned above. The reheating segmentation can also be extended to FGHAZ and ICHAZ, considering the due metallurgical aspects of these regions.

Figure 15 – Schematic of the HAZ segmentation, revealing the relationship between the HAZ microstructure, the thermal distribution, and the Fe-Fe_3C phase diagram in steel welding.

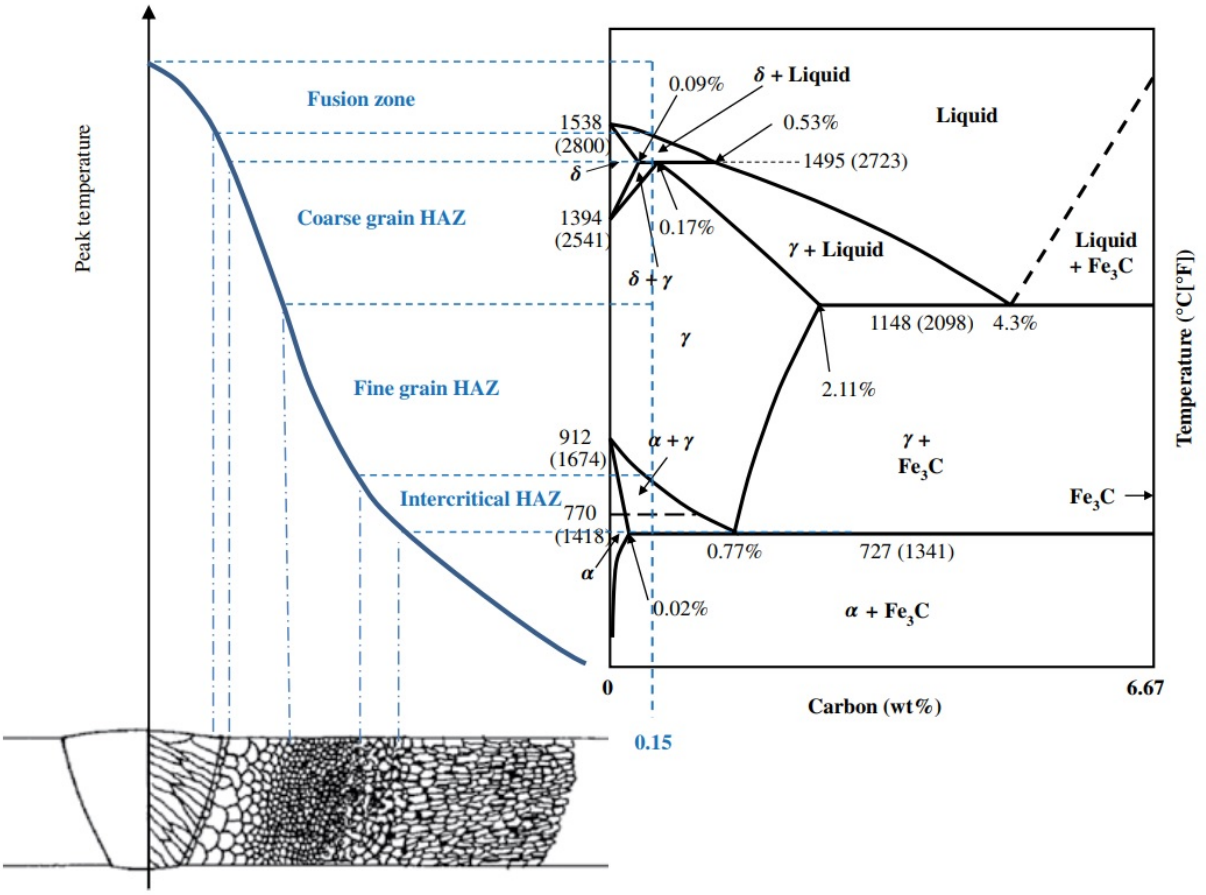

Source: Lippold *et al.* (2015).

2.4.2 9Ni steels welding

In 9Ni steels welding, it is expected to obtain a predominantly martensitic HAZ, given the previously mentioned high hardenability of these alloys (FONDA; SPANOS, 2014). It is observed with the obtainment of a martensitic matrix throughout the entire HAZ, whose microstructure varies only in function of the size of the hierarchical constituents and the volume fraction of second phases (retained/reverse austenite and carbides) (JANG *et al.*, 1998). In addition, another expected feature is the variation in mechanical/metallurgical properties when the base metal is subjected to different prior heat treatment, which is reported by Barrick *et al.* (2017), who evaluated the HAZ resulting from welding performed on 10Ni steels samples subjected to intercritical quenching and tempering and 10Ni steels samples subjected to simple quenching.

These microstructural features are widely related to the heterogeneity of the mechanical properties of the HAZ in 9Ni steels welds. Nippes and Balaguer (1986), through thermal

simulations carried out in a Gleeble system, verified a decrease in volume fraction of retained austenite with the increase in the peak temperature, relating this decrease of austenite content to the observed decrease in toughness. These results would be following the reports of Jang *et al.* (1997), which, evaluating the results of Crack Tip Opening Displacement (CTOD) tests, found a decrease in the toughness of HAZ regions closer to the FZ, an observation that would be associated with the low volume fraction of retained austenite at these regions, which would result from the limitation of nucleating sites for the austenite.

Figure 16 – Schematic representation of the superposition of thermal cycles and microstructures observed in multipass welding of steels.

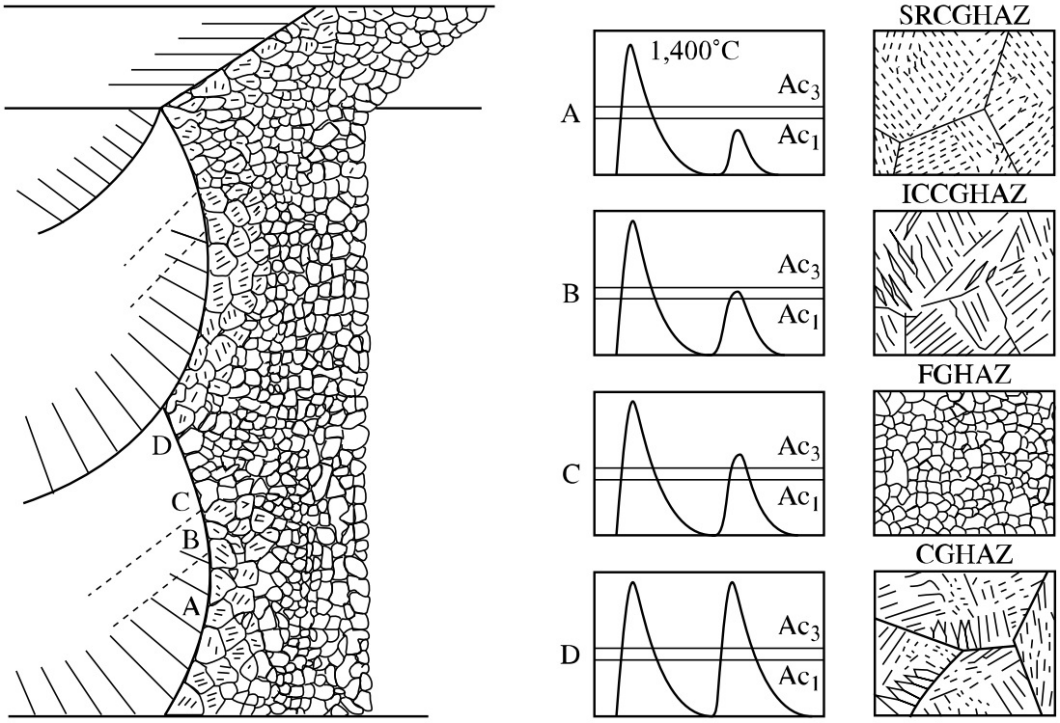

Source: Blondeau (2013), original from Matsuda *et al.* (1996).

The same authors carried out studies on the HAZ in multi-pass welding of 9Ni steels, where the presence of LBZ was verified, which correspond to regions characterized as UA-CGHAZ and IC-CGHAZ (JANG *et al.*, 2002; JANG *et al.*, 2003). This observation would be associated with the M-A constituents along the CGHAZ. In IC-CGHAZ, the M-A constituents show a significant increase in carbon content compared to the M-A constituents of the other CGHAZ regions, while the UA-CGHAZ presents a higher fraction of M-A constituents in comparison to the other regions (JANG *et al.*, 2003). Similar results are observed in studies on multi-pass welding of high-strength steels (KIM *et al.*, 1991; DAVIS; KING, 1994).

Furthermore, regarding the intercritical reheating, Barrick and DuPont (2019), eval-

uating thermal simulations of 10Ni steel welding, observed a microstructure characteristic of an IC-CGHAZ for a wide range of peak temperatures, ranging from 750 °C to 1000 °C. This wide range would be associated with the "sluggish" Ni diffusion at the high heating and cooling rates observed in welding. The authors also report that the toughness and the retained austenite fraction do not exhibit the expected strong correlation proposed by previous studies, suggesting that other microstructural features could have more impact on the toughness of ZAC.

3 MICROMECHANICAL CHARACTERISATION OF THE HEAT-AFFECTED ZONE IN MULTI-PASS WELDING OF 9NI STEEL PIPES

3.1 Abstract

9Ni steels have been recently adopted in supercritical CO_2 injection systems in deepwater oil fields. The manufacture of these reinjection systems involves multi-pass welding procedures, which produce an HAZ with a high heterogeneity level regarding the microstructural features and the local mechanical properties. An extensive microstructural and micromechanical characterisation was performed over the HAZ of three welded joints with different heat-input conditions to evaluate the effects of the reheating cycles and the welding parameters on the microconstituents. Light Optical Microscopy (LOM), Scanning Electron Microscopy (SEM) and EBSD analyses were performed to identify microstructural features that correlate to the local mechanical responses evaluated through an extensive microhardness mapping. Regarding the CGHAZ, the highest microhardness values for all welding conditions are found at the SCR-CGHAZ, characterised by its refined microstructure and a quite low area fraction of coarse martensite laths. The SC-CGHAZ and the IC-CGHAZ – regions where wider martensite blocks and higher coarse martensite lath area fractions were observed – composed the softer zones of the microhardness map. It was also found that reheating at intercritical temperatures induces the formation of fresh martensite and the stabilisation of C-rich retained/reversed austenite particles, which may degrade the mechanical properties at the IC-CGHAZ.

Keywords: 9Ni steels. Welding. Heat-affected zone. Microstructural features. Micromechanical characterisation.

3.2 Introduction

The challenges of the offshore oil and gas production have been, through decades, promoting many technological advancements to the petroleum industry, like the prospecting of oil in deep waters (HEDBERG *et al.*, 1979), the deep offshore drilling technologies (DUHEN *et al.*, 1997), and the manufacturing of complex subsea systems (CEZAR *et al.*, 2015). In Brazil, the oil production in the pre-salt region of the Santos basin faces a challenge related to the high concentration of carbon dioxide (CO_2), which may reach values up to 12%. As soon as modules process the CO_2 removal on the Floating, Production, Storage and Offloading (FPSO) unit, the

separated CO_2 has been pressurised and then transported through pipelines to injection wells (BELTRÃO *et al.*, 2009). This process mitigates the emission of CO_2 and plays an essential role in oil recovery, improving wells' efficiency (DING *et al.*, 2017).

Favouring the efficiency of the injection processes, the CO_2 must be transported in a liquid or supercritical state, demanding the application of high pressures, scaling up to 550 bar (ELDEVIK *et al.*, 2009; KNOOPE *et al.*, 2013). In this scenario, depressurisation, caused by cracking or by a malfunction in flange sealing rings, may lead to an abruptly localised decrease in temperature, which may reach -90 °C, eventually promoting localised embrittlement of the pipeline (SCHEID *et al.*, 2016).

In this context, 9Ni steels stand out as a great option for manufacturing the top side portion of these injection systems. Presenting a DBTT as low as -196 °C (SHIN *et al.*, 2000), those steels are commonly adopted in the transport and storage of LNG, and its applications are recently expanding to the supercritical CO_2 injection in deepwater oil fields (FARIAS *et al.*, 2018). The manufacture of the injection system involves welding procedures, which, must follow a multi-pass approach due to the large wall thickness of the pipes. The resulting HAZ microstructure is essentially martensitic due to the high hardenability of 9Ni steels (FONDA; SPANOS, 2014). However, the superposition of welding heat cycles will drastically impact the HAZ microstructure by introducing heterogeneity upon microstructural features, such as the size and morphology of constituents and the fraction of second phases. It is reported that the multi-pass welding can introduce LBZ in 9Ni steels HAZ (JANG *et al.*, 2002; JANG *et al.*, 2003), which would be related to the presence of M-A constituents (JANG *et al.*, 2003).

Along with the features associated with the M-A constituents, other microstructural factors may also impact the 9Ni steel toughness. The retained austenite, for example, is classically attributed as the most significant agent for toughness improvement in 9Ni steels (MARSHALL *et al.*, 1962; ZHANG *et al.*, 2013), which many authors classify as TRIP steels (ZHANG, 2012; ISHEIM *et al.*, 2013; JAIN *et al.*, 2018), proposing that the martensite transformation induced by plastic strain would enhance plasticity by the introduction of deformation mechanisms (OLSON; AZRIN, 1978). However, Barrick and DuPont (2019), in a study on simulated HAZ in a 10 wt% Ni steel, demonstrated that the toughness is not solely derived from the austenite content, which is unexpected for TRIP steels. The authors verified that, in some cases, austenite content does not even follow a positive correlation with toughness (BARRICK; DUPONT, 2019). Also, recent papers point out martensite morphology heterogeneities as one major factor in determining

deformability in low-carbon Ni-alloyed steels (MORSDORF *et al.*, 2016). Morsdorf *et al.* (2015) developed extensive work towards the characterisation of microstructural heterogeneities in 5Ni steel. The authors identified coarse martensite laths as soft zones within a much harder matrix of thin laths, proposing that these constituents form a nano-composite-like microstructure, in which the coarse martensite lath could significantly enhance the steel's toughness.

Drawing the relationship between microstructure and mechanical properties in 9Ni steels has proven to be a complex task, which can be hampered when evaluating the reheated HAZ resulting from multi-pass welding. Although few studies were presented regarding the effects of multi-pass welding on microstructure and toughness of the HAZ in 9Ni steels (JANG *et al.*, 1997; JANG *et al.*, 1998; JANG *et al.*, 2002; JANG *et al.*, 2003; JANG *et al.*, 2003), there is a lack of information on how the numerous microstructural features may impact the mechanical properties of this HAZ. In this context, the present study aims to conduct a detailed microstructural investigation through the different HAZ regions, using an extensive microhardness mapping on the HAZ of 9Ni steel pipes multi-pass girth welds as reference. Three heat-input conditions were submitted to microstructural characterisation by LOM and SEM with EBSD analysis.

3.3 Experimental procedure

This work analysed three distinct welded joints of quenched and tempered ASTM A333 Gr.8 (9Ni) steel pipes, which chemical composition (Table 3) was evaluated through optical emission spectroscopy with a Shimadzu PDA-7000. The pipes presented a diameter of 219.1 mm and thickness of 31.7 mm and were girth welded through GMAW using a Markle HighPULSE 550 RS power source in a robotic workbench equipped with a KUKA KR16 robot and a KUKA DKP-400 positioner. The adopted filler metal was the Ni-based superalloy Inconel 625 (AWS ER NiCrMo-3), and its chemical composition is presented in Table 2. For the root pass, a heat input of 0.5 kJ/mm was aimed in all joints, using a continuous direct current of 119 A, a voltage of 16,4 V, and a 250 mm/min welding speed, achieving a short-circuiting metal transfer. For the fill and cap passes, pulsed GMAW was applied, imposing different heat-input conditions for each of the three welded joints. The aimed parameters for each condition are presented in Table 4 (MIRANDA; SILVA, 2016).

Samples of the welded joints' complete cross-section were removed and submitted to conventional metallographic preparation, being grinded with sandpaper and mechanically polished up to 1 μm diamond paste.

Table 2 – Typical weld metal analyses (wt.%) of the AWS ER NiCrMo-3.

C	Mn	Si	Ni	Cr	Mo	Nb	Fe
0.09	0.05	0.12	Bal.	21.90	8.70	3.65	0.62

Source: WELDWIRE (2021).

Table 3 – Chemical composition (wt.%) of the ASTM A333 Gr.8 (9Ni) steel pipes.

C	Mn	Si	Ni	Cr	S	P	Fe
0.032	0.496	0.278	9.460	0.032	<0.005	<0.005	Bal.

Source: Own elaboration.

With surfaces in as-polished condition, microhardness Vickers mapping was carried out with a LECO AMH55 LM-110AT tester on the HAZ of each sample. A load of 100 gf and a dwell time of 13 s were applied, while the samples were orthogonally displaced, guaranteeing a 100 μm distance between each indentation. The mapped areas covered the reheated HAZ of at least three fill passes located at the half-height of the samples. Also, microhardness profiles were evaluated on the cap passes HAZ of each sample, aiming to compare a non-reheated HAZ with the reheated mapped HAZ.

Table 4 – Parameters for fill and cap passes in welding of ASTM A333 Gr.8 (9Ni) steel pipes.

Heat-input condition	Arc voltage (V)	Mean welding current (A)	Welding speed (mm/min)	Heat-input (kJ/mm)
Low heat-input			470	0.7
Medium heat-input	30	184	220	1.5
High heat-input			132	2.5

Source: Modified from Miranda and Silva (2016).

The samples' HAZ and Base Metal (BM) were then chemically etched by immersion in 4% Picral solution for 45 s followed by immersion in 2% Nital solution for 20 s. LOM analysis was then performed as a first evaluation step with a Carl Zeiss Axiovision Z1M. A deeper analysis was carried out by SEM using a FEI Quanta 450 FEG operated at 20 kV in secondary electron mode. Figure 17 shows the etched low heat-input sample, highlighting the HAZ mapped area.

For macrohardness measurements Hardness Vickers testing was conducted in a ZwickRoell Indentec ZHU250CL universal hardness tester. A load of 10 kgf and a dwell time of

10 s were applied for 6 indents scattered along the fill passes' HAZ of each welded joint.

Also, size-reduced samples of the welding interfaces were extracted for microstructural investigation through EBSD analyses. Those samples were submitted to a similar metallographic preparation with the addition of a final electropolishing step, which was performed with a mixture of 70% perchloric acid in 99.8% ethanol in a volume ratio of 1:9. The polishing was conducted at 10 °C, applying 25 V during 50 s. EBSD measurements with 0.5 μm step size were carried out in a FEI Quanta 250 SEM coupled with Oxford Nordlys Max EBSD detector operated at 20 kV. Inverse Pole Figure (IPF) maps and microstructural interfaces were then constructed using Channel 5 package to evaluate the size distribution of martensite constituents along the HAZ of each sample.

Figure 17 – Low heat-input sample macrography showing the multi-pass weld cross-section. The dark zone corresponds to the Inconel 625 fusion zone, and the light grey along with the interface is the HAZ. Sample etched by immersion in 4% Picral and 2% Nital solutions (a). Macrography of the enlarged mapped region as indicated in Figure 17a (b). LOM micrograph montage of the microhardness mapped region (c).

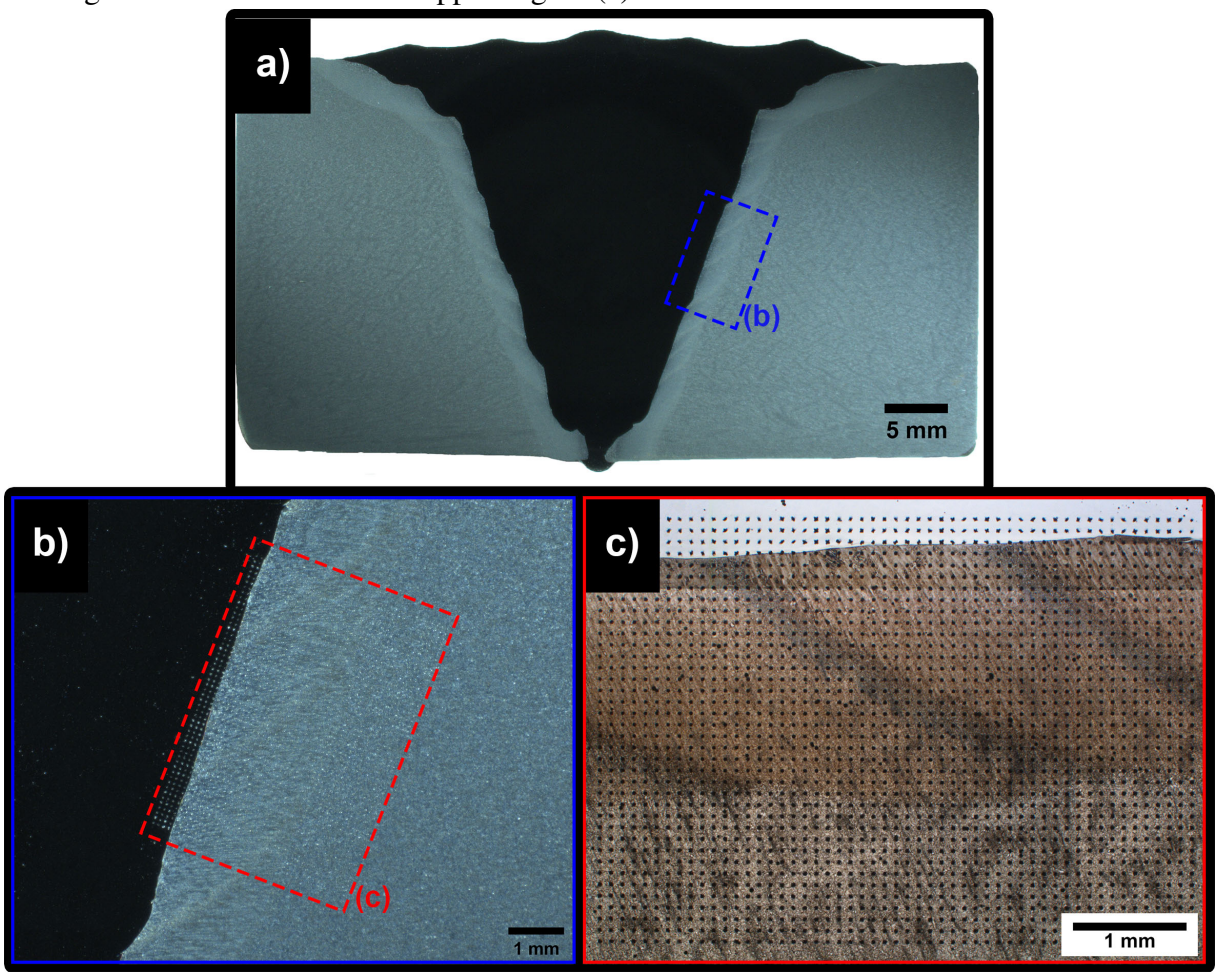

Source: Own elaboration.

3.4 Results and discussion

3.4.1 Microhardness testing

Figure 18 shows the microhardness profiles for the cap passes HAZ in each sample, presenting insets of LOM micrograph montages which supported the HAZ segmentation into CGHAZ, FGHAZ and ICHAZ. Regarding the CGHAZ and the FGHAZ, complete austenitization ($T > Ac_3$) is provided in both cases. However, in CGHAZ, the peak temperature is sufficiently high to promote intense grain growth, achieving a coarse microstructure, while, in FGHAZ, a lower austenitization temperature will result in a refined microstructure. The ICHAZ, in turn, is submitted to intercritical temperatures ($Ac_3 > T > Ac_1$) in which partial austenitization occurs, also allowing carbon diffusion and precipitation, mainly along with grains and lath boundaries (LIPPOLD *et al.*, 2015). Some authors may also discriminate a fourth HAZ region in carbon and low alloy steels welding, the so-called SCHAZ, submitted to temperatures below Ac_1, providing a tempering effect (BHADESHIA; HONEYCOMBE, 2017). The SCHAZ wasn't identified in any of the profiles of Figure 18, as the BM microstructure already consists of tempered lath martensite, which is the expected microstructure for the SCHAZ.

From the microhardness profiles of Figure 18, it is clear that the CGHAZ consists of a softer HAZ region at the cap passes of all samples, while the higher microhardness values are observed at the FGHAZ, and moderate values are observed at the ICHAZ. These results oppose Fernandes *et al.* (2020) observations, which report the CGHAZ as the hardest and most brittle HAZ region. Nevertheless, having the CGHAZ as softer HAZ regions corroborates the recent proposals by Morsdorf *et al.* (2015), which points out the coarse martensite lath as a significant agent for mechanical properties determination in low-carbon Ni-alloyed steels, being identified as soft zones inside a thin lath martensite matrix, and capable of significantly enhance the steel's toughness. The author verified that a larger austenite grain size would increase the coarse lath area fraction (MORSDORF *et al.*, 2015). Therefore, it is expected that the CGHAZ might present a more significant coarse lath area fraction over the other HAZ regions.

Regarding the reheating imposed by the multi-pass welding, Figure 19 shows the microhardness mappings over the fill passes HAZ in each sample, revealing a heterogeneous but standardised HAZ, where it is possible to discriminate regions according to their microhardness values. On maps, the upper area of light blue tones consists of the FZ, while the lower area, composed of dark blue tones (lower microhardness), consists of the BM.

Figure 18 – Microhardness profiles for the cap passes HAZ in samples of low heat-input (a), medium heat-input (b) and high heat-input (c). The profiles cover from the FZ to the BM.

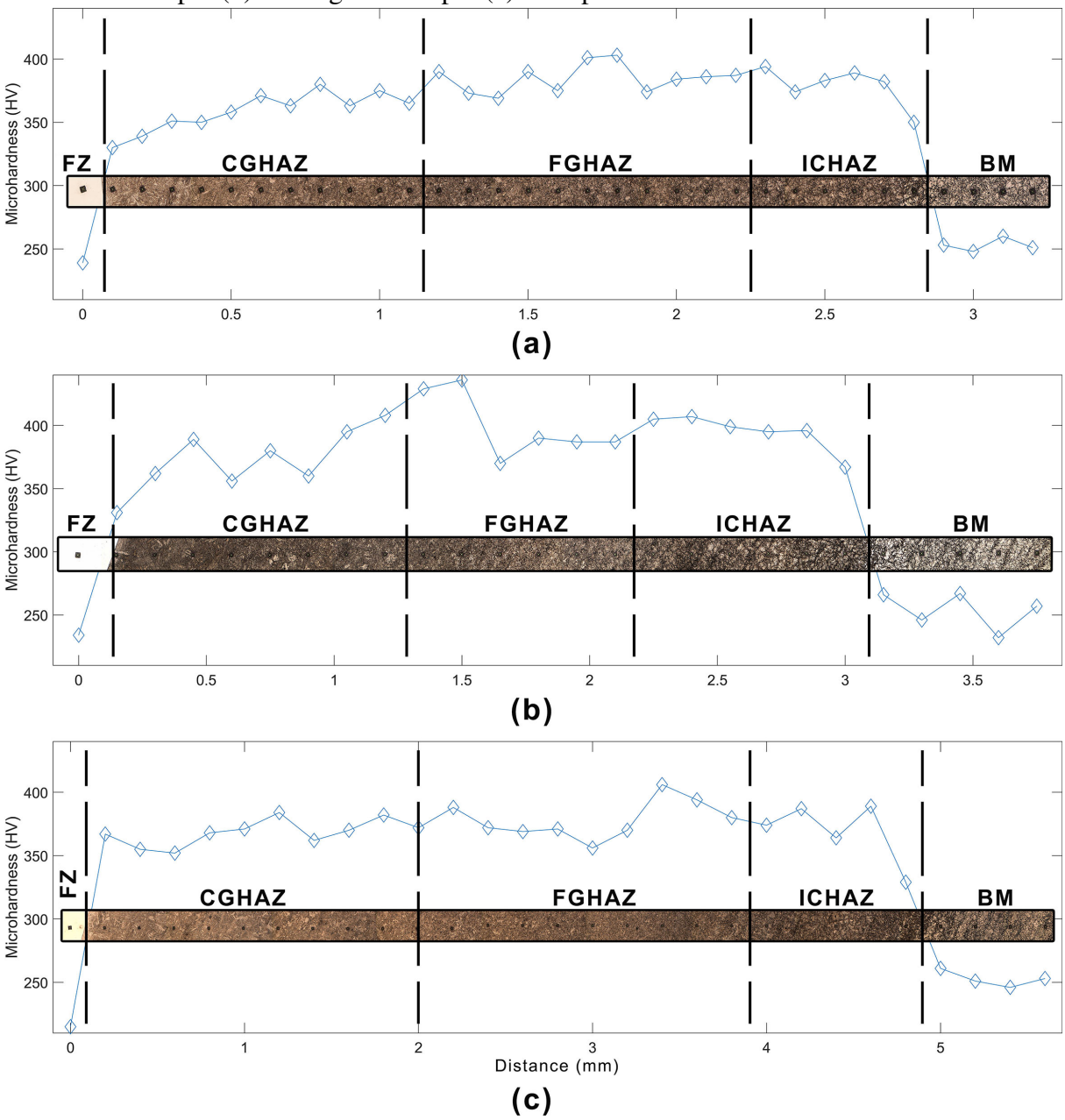

Source: Own elaboration.

To evaluate the reheated HAZ, we may introduce new labels to describe the impact of the reheating thermal cycles over the previous passes' HAZ. Therefore, the previously introduced HAZ segmentation may be sub-categorised according to the reheating temperature. The CGHAZ, for example, can be segmented into: Subcritically reheated CGHAZ (SC-CGHAZ); Intercritically reheated CGHAZ (IC-CGHAZ); Supercritically reheated CGHAZ (SCR-CGHAZ), condition achieved when low super-critical reheating temperatures are imposed, resulting in a microstructure similar to that of the FGHAZ; Unaltered CGHAZ (UA-CGHAZ), condition

achieved when high super-critical reheating temperatures are imposed or when isn't observed any relevant effect from reheating (KIM *et al.*, 1991; JANG *et al.*, 2003).

This segmentation relates to the high heterogeneity of mechanical properties that is clearly observed in the microhardness maps, where a wide range of microhardness values is obtained at the HAZ of each sample. Figure 20a shows statistics about the macrohardness measurements taken inside the HAZ of each sample, pointing out a drop in microhardness values with the increase of heat-input, which relates to the increase in softer zones area fraction observed when comparing the maps of Figure 19.

Figure 19 – Microhardness mapping over reheated HAZ of fill passes on samples of medium heat-input (a), low heat-input (b) and high heat-input (c).

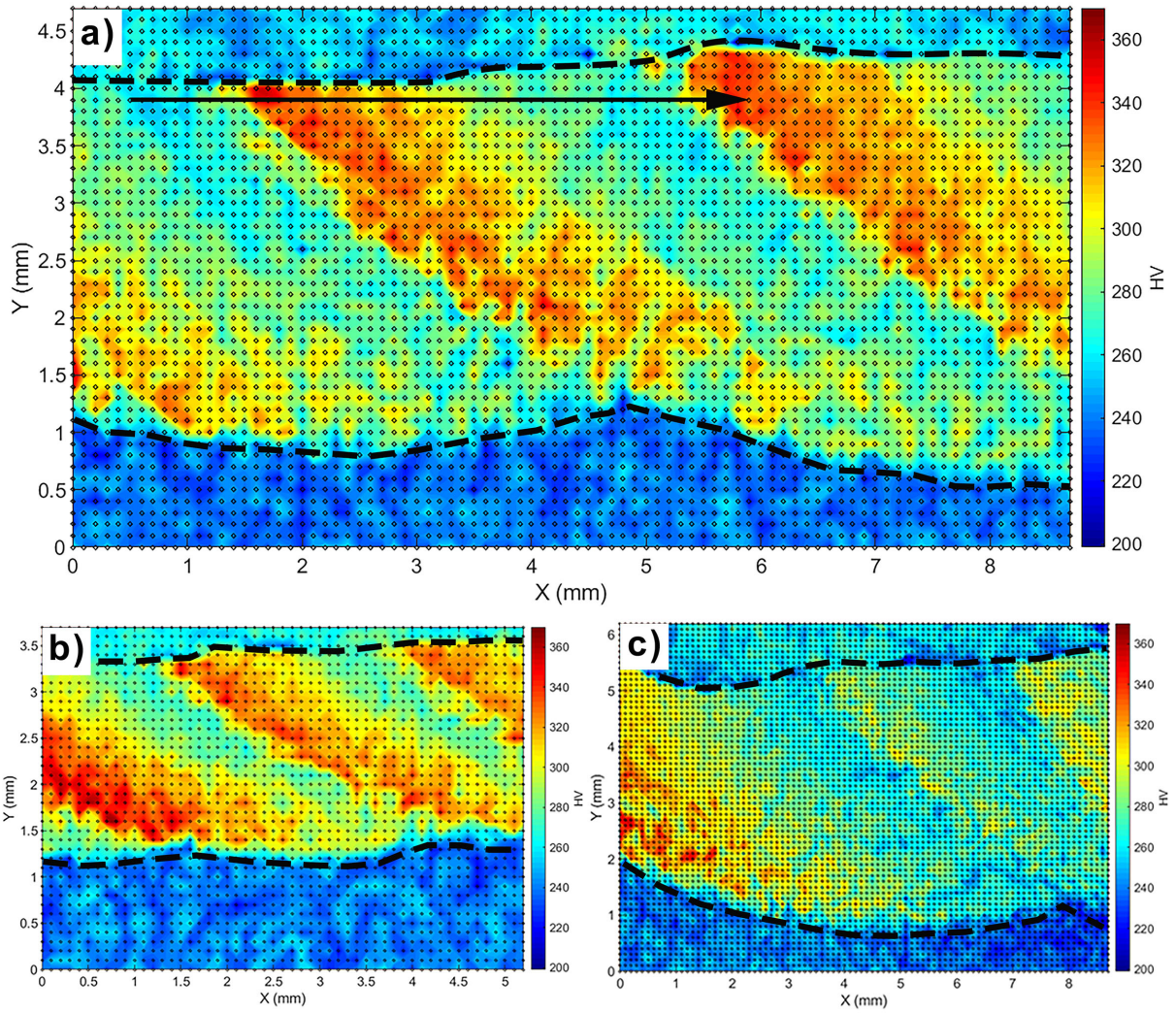

Source: Own elaboration.

The microhardness mapping revealed that high hardness zones, as well as low hardness zones, may reach out the whole HAZ extension, from the weld interface to the BM, expanding in a close to radial manner. This configuration indicates that the reheating cycles

greatly impact the mechanical properties of the HAZ, surpassing the influence of the initial HAZ microstructure defined by the previous welding pass. The effects of the reheating cycles are also highlighted by the microhardness values periodicity observed when evaluating profiles parallel to the weld interface. This behaviour is demonstrated by the microhardness profile presented in Figure 21, which follows the vector displayed in Figure 19a. The profile exhibit two valleys, at X = 1,0 mm and X = 4,9 mm, and two peaks, at X = 1,7 mm and X = 5,7 mm. Each one corresponds to a specific HAZ region with particular microstructural features, as will be demonstrated later.

Figure 20 – Mean values and error bars from macrohardness measurements taken on the HAZ (a). Mean values and error bars from microhardness measurements taken on the SC-CGHAZ (b), the IC-CGHAZ (c) and the SCR-CGHAZ (d) within the mapped areas.

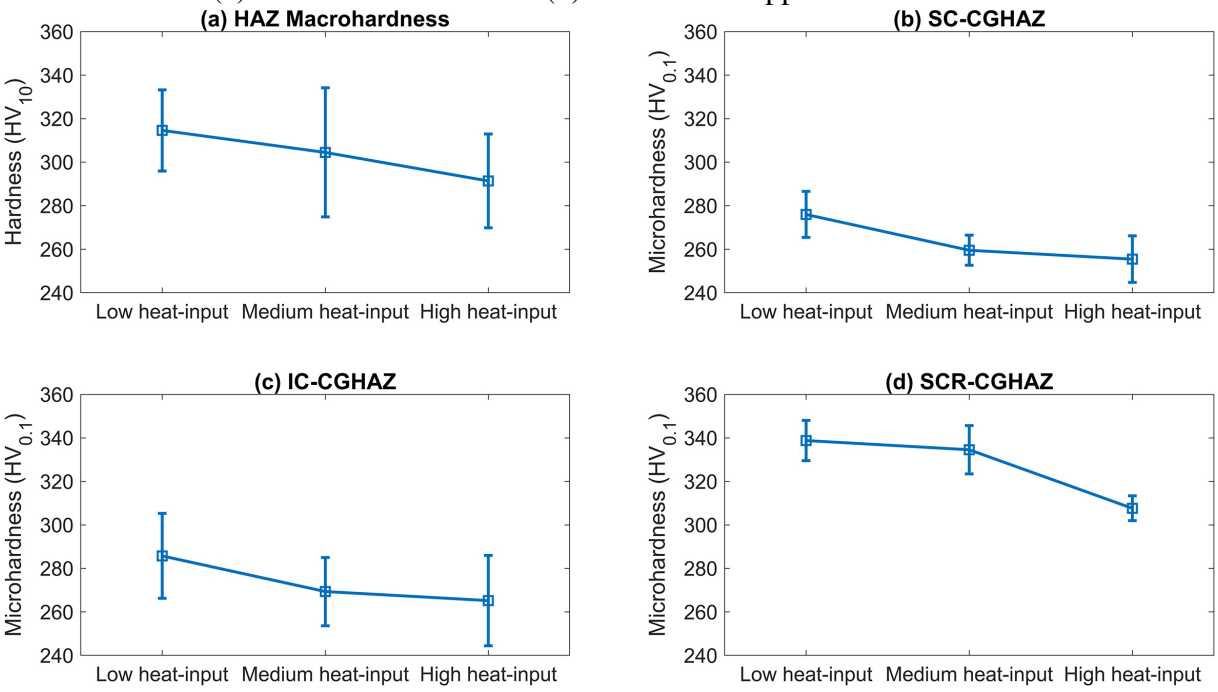

Source: Own elaboration.

3.4.2 Microstructural characterisation

To understand the impact of the heating cycles over the HAZ microhardness distribution it is necessary to carry out an extensive microstructural investigation over this complex zone. By an initial HAZ macro analysis, it is possible to tell that the radial regions of the microhardness maps correspond to regions submitted to similar reheating cycles. Figures 22a and 22b reveal that the soft HAZ zones of the map initially presented in Figure 19a are invariably located to the left of intensely etched regions, which exhibit darker tones in LOM analyses. As one may see by the HAZ pattern shown in Figures 22a and 22b, those soft zones relate to

the HAZ regions that are the farthest from the heat source of the respective welding pass and, therefore, are submitted to a low temperature reheating, which will promote a tempering effect on those regions. Through the same images, it's possible to verify that this reheating cycle isn't pronounced at the HAZ/BM interface, as the BM already exhibits a microstructure composed of tempered martensite. Those observations validate the fact that the soft HAZ regions of the microhardness maps from Figure 19 consist of subcritically reheated areas.

Figure 21 – Microhardness profile obtained by following the vector displayed in Figure 19a.

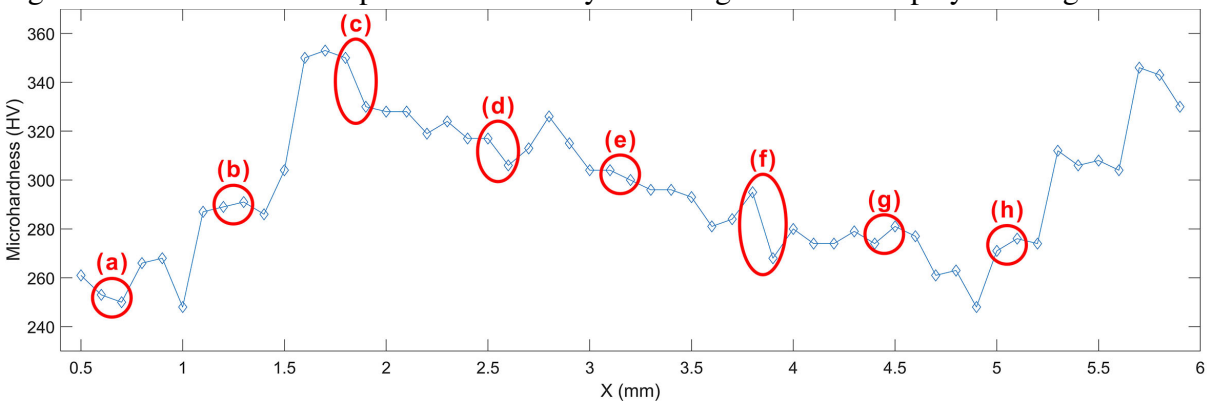

Source: Own elaboration.

However, considering the high microstructural complexity of the evaluated reheated HAZ, the proper identification and characterisation of the different HAZ regions demand a higher magnification analysis. Be that as it may, to evaluate the effect of reheating on the microstructure, efforts were concentrated on investigations close to the weld interface, seeking to obtain information regarding the CGHAZ and its previously described segmentation. Figures 22c-g show micrographs of the regions highlighted in Figure 22a. In those images, the microhardness indents were superimposed by geometries coloured according to the microhardness scale introduced in Figure 19. Also, higher magnification LOM images are presented in Figure 23 following the microhardness profile of Figure 21. The highlighted indents in Figure 21 are marked with red borders at the micrographs of Figure 23.

Figure 22c exhibit a micrograph over the softer CGHAZ region. The microstructure is highly etched on the right side, exhibiting a higher contrast in LOM analysis, while the microstructure on the left side doesn't share the same aspect. A higher magnification LOM micrograph of the later region is presented in Figure 23a. As discussed above, the HAZ microhardness pattern indicates that this region consists of the SC-CGHAZ, presenting microhardness values ranging from 250 HV to 271 HV for the medium heat-input condition (Figure 20b), while the non-reheated CGHAZ of the cap passes presented a mean value of 357,4 HV. At

the SC-CGHAZ registered in Figure 23a, it is possible to identify dark etched features, which resemble precipitates nucleated at the microstructure interfaces, such as lath, block and packet boundaries that may act as nucleating agents.

Figure 22 – Overview of the mapped area in the medium heat-input sample (a) with an overlay of the microhardness map introduced in Figure 19a (b). Micrographs of the regions highlighted in Figure 2a, revealing the reheated CGHAZ segmentation (c-g).

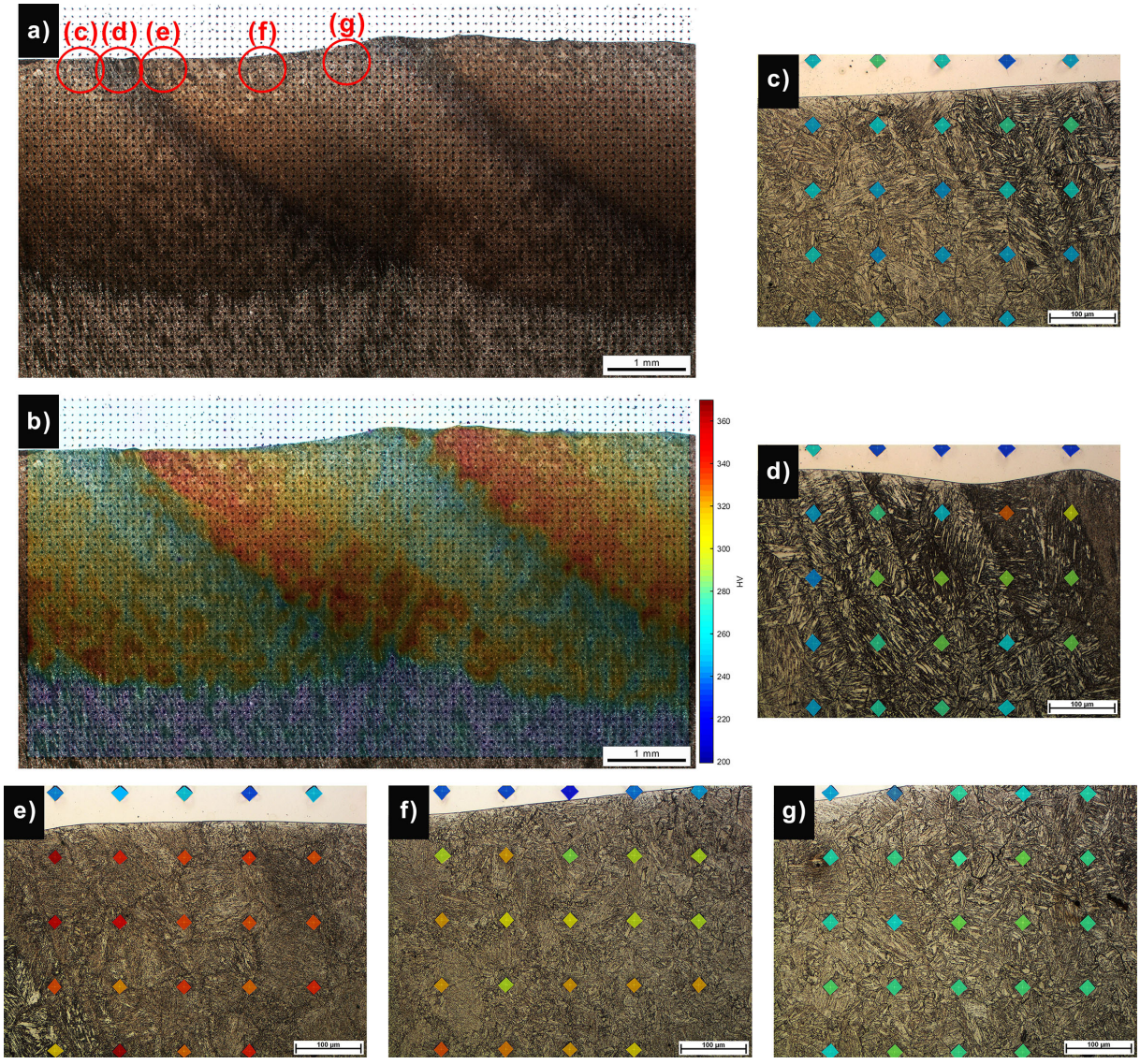

Source: Own elaboration.

This precipitation is evident in the SEM image shown in Figure 24a, where a clear decoration can be observed at the boundaries of the highlighted coarse martensite lath, as pointed out by the red arrows, and Figure 24b, which shows the distribution of the precipitated particles throughout the previously mentioned microstructure interfaces, with the yellow arrows indicating the precipitation throughout the PAG boundaries, while the red and blue ones point to precipitates at the martensite packets and blocks interfaces, respectively. Those particles at the

SC-CGHAZ mainly consist of carbides that may experience growth due to the tempering effect resulting from the subcritical reheat (MORSDORF *et al.*, 2015). Furthermore, intense carbide precipitation is also observed in the interior of the coarse laths on SC-CGHAZ, as can be seen in Figure 24a. Those nanometric carbides typically extend in three orientation variants, agreeing with results from Fonda and Spanos (2014), which suggest that the coarse lath is initially formed as a supersaturated component and the precipitation of carbides takes place during subsequent thermal activation, discarding the hypothesis of bainite coalescence proposed by other authors (BHADESHIA *et al.*, 2006; KEEHAN *et al.*, 2008).

The particle precipitation along the microstructure interfaces is even more evident in the region registered in Figures 22d and 23b, which consists of the previously mentioned highly etched area. As pointed out in Figure 23b, in LOM analysis, an intense decoration by coarse particles is observed at the packet boundaries and the PAG boundaries. This decoration was then evaluated in SEM analysis, as shown in Figure 24c, identifying the presence of fine structures of fresh martensite – indicated by the yellow arrows – and faceted particles of retained/reversed austenite – indicated by blue and red arrows. Those observations provide solid information for classifying this region as an IC-CGHAZ, which experienced an intercritical reheating capable of partially austenitizing the microstructure. The austenite mainly nucleates at the packet and PAG boundaries, being later submitted to high cooling rates, resulting in fresh martensite and a small fraction of stable austenite. This stabilisation may be primarily promoted by the diffusion of austenite stabiliser elements, such as C and Ni, to the reversed austenite. During holding at intercritical temperature, Ni can be rapidly segregated into austenite due to its higher diffusivity (YANG *et al.*, 2010). Also, the diffusive activity may be noted by analysing the coarse laths interior. As one may see, in Figure 24d, a lack of precipitates is observed within the highlighted coarse laths, which exhibit a featureless surface, contrasting with the previously presented coarse laths of the SC-CGHAZ. During holding at intercritical temperature, the carbides precipitated within the coarse martensite laths may experience dissolution, and the C atoms will segregate to the coarse lath interfaces, acting on the stabilisation of austenite while "cleaning" the interior of coarse laths. Thereby, the condition presented in Figure 24d will be achieved, where the coarse laths exhibit a featureless surface, and their boundaries are decorated by austenite particles. Compared to the SC-CGHAZ, a wide range of microhardness values is observed on IC-CGHAZ, presenting values from 248 HV to 289 HV for the medium heat-input condition (Figure 20c), where the higher microhardness values may be a consequence of the fresh martensite nucleation.

Figure 23 – CGHAZ LOM images. Micrographs were taken over the highlighted indents of the microhardness profile presented in Figure 21 (a-h). The red-bordered geometries identify indents contained in the profile.

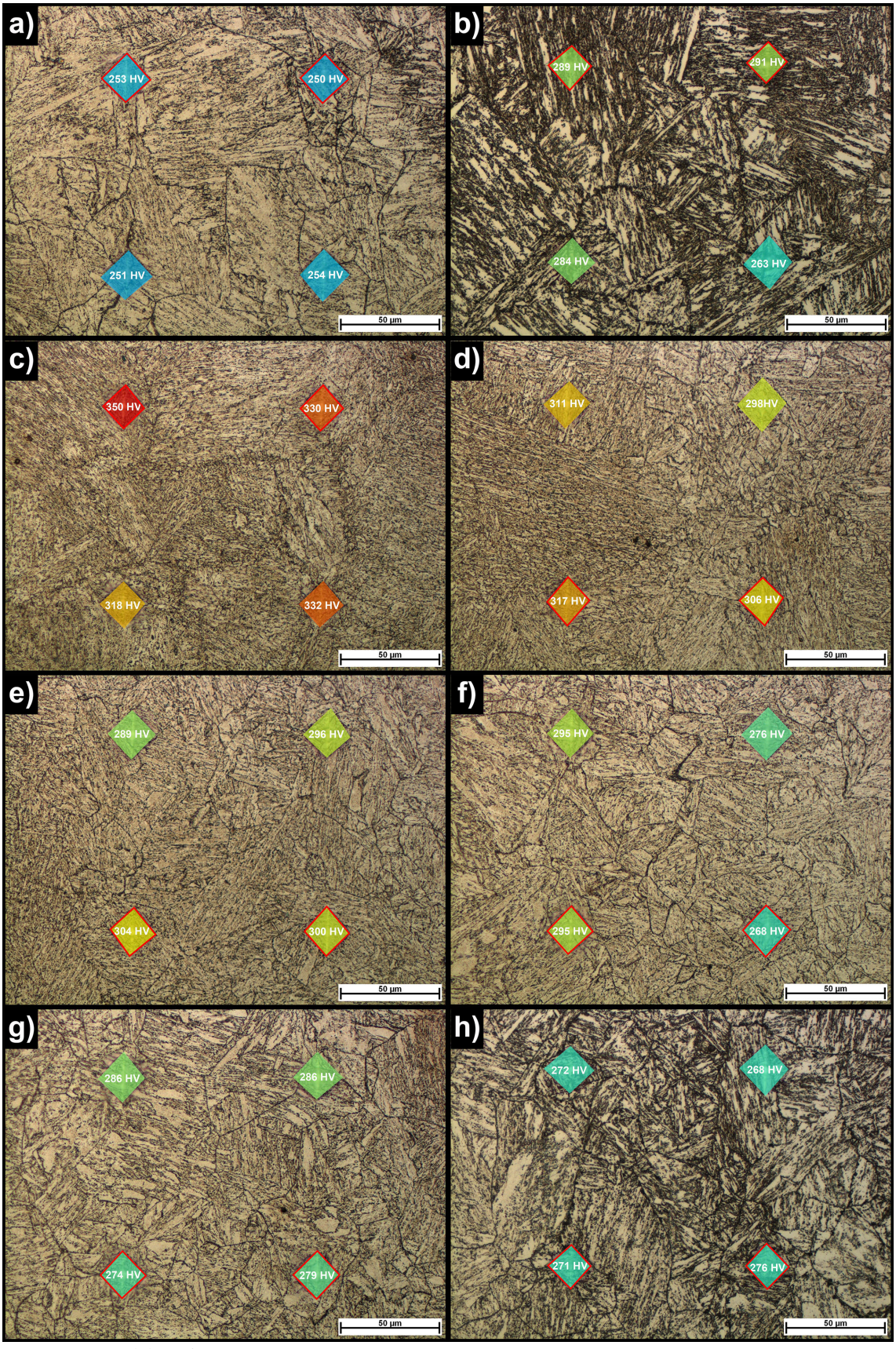

Source: Own elaboration.

Figure 24 – Low heat-input sample CGHAZ SEM images. Micrographs highlighting the microstructural features of the SC-CGHAZ (a-b), the IC-CGHAZ (c-d) and the SCR-CGHAZ (e-f).

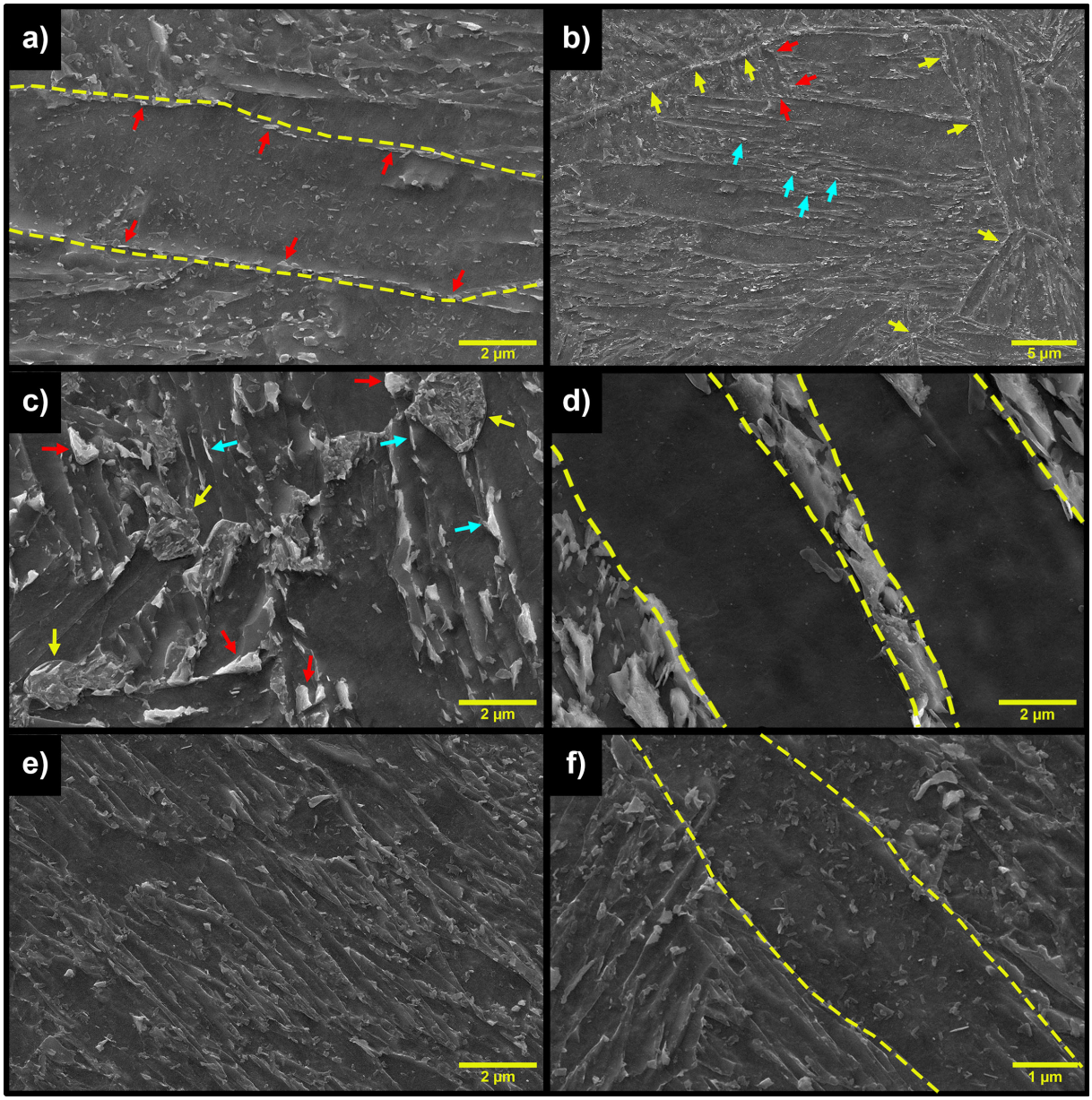

Source: Own elaboration.

Continuing the microstructure scanning through the welding interface, Figures 22e and 23c show LOM images over the hardest CGHAZ region, exhibiting an average microhardness value of 335 HV – for the medium heat-input condition (Figure 20d). Coming from the IC-CGHAZ, this region is strongly characterised by an abrupt increase in microhardness values which follows an evident change in microstructural features, mainly related to the refinement of martensite structures. Figure 24e shows a SEM image of this region, revealing a microstructure mainly composed of thin laths and finely dispersed precipitates located at the lath boundaries.

Although the area fraction of coarse lath is drastically decreased, Figure 24f exposes a coarse martensite lath detected in this region, revealing nanometric carbides precipitation in the interior of this microconstituent, in a similar condition to the one observed on SC-CGHAZ. Following the previous classifications, it is expected that this region would consist of a SCR-CGHAZ. It makes sense that a low-supercritical reheat could achieve a refinement of the microstructure. Morsdorf *et al.* (2015) reported that low austenitization temperatures can substantially decrease the area fraction of coarse laths. The resulting refinement is reflected in the high microhardness values observed in this area. Also, these results agree with the initial analysis at the cap passes HAZ, which shows the FGHAZ – region submitted to low-supercritical temperatures – as the hardest HAZ region (Figure 18).

Figure 22f is representative of a gradual transition zone, where higher supercritical temperatures will result in coarser martensite structures, decreasing the microhardness values. Figures 23d-f exhibit the microstructure evolution through this transition zone, where the registered regions correspond to the respective markers over the microhardness profile in Figure 21. The progressive temperature increase is expected to lead to an UA-CGHAZ microstructure. Instead, the effects of the reheating promoted by the next welding pass were observed, resulting in a microstructure characteristic of the SC-CGHAZ, as shown in Figures 22g and 23g. Continuing the microstructural analysis over the microhardness profile, Figure 23f reveals the beginning of another IC-CGHAZ, exposing a periodic microstructural pattern related to the periodicity of microhardness values presented in Figure 21. The same microstructure pattern is observed for all samples, not presenting regions that would be characteristic of an UA-CGHAZ. In fact, the only reheated CGHAZ region with microhardness values similar to the CGHAZ of cap passes is the SCR-CGHAZ, confirming that the deposition pattern of the welding fill passes was capable of avoiding the presence of UA-CGHAZ regions, which are reported as LBZ in 9Ni reheated HAZ (JANG *et al.*, 2002; JANG *et al.*, 2003; JANG *et al.*, 2003).

As exhibited in Figure 25, each CGHAZ region presents similar microstructural features in all welding conditions. However, differences arise when evaluating the morphological aspects of the lath martensite microstructure, such as martensite blocks width and coarse laths area fraction.

Aiming to evaluate the variation in martensite block width, each sample's CGHAZ microstructure was analysed via EBSD. Figure 26 exhibit, for example, IPF maps used to measure martensite block width along the CGHAZ of the low heat-input sample. According to

reports by Long *et al.* (2016), high angle interface boundaries were reconstructed over the maps: boundary orientation angles from 15° to 45° for PAGs, from 45° to 55° for martensite packets, and from 55° to 65° for martensite blocks, those boundaries are also highlighted in Figures 26d-f. At least 40 martensite blocks were measured for each region in each welding condition.

Figure 25 – SEM micrographs registering, respectively, the SC-CGHAZ, the IC-CGHAZ and the SCR-CGHAZ in the samples of low (a-c), medium (d-f) and high (g-i) welding heat-input.

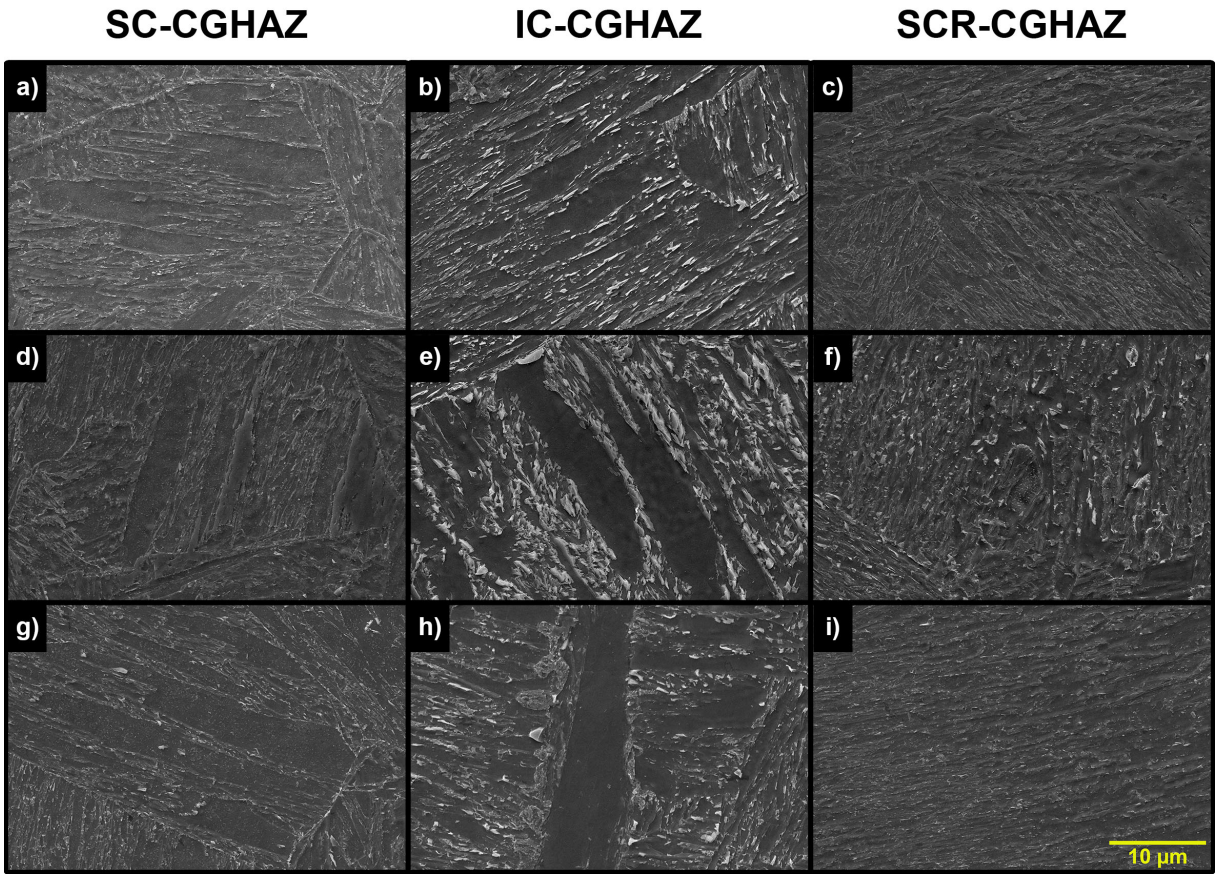

Source: Own elaboration.

Figure 27 shows the trend regarding the martensite block size on the evaluated samples through boxplots, which indicate the maximum and minimum values, in addition to the median and the first and the third quartiles, while the diamond marker inside each box represents the mean values. It is observed that the SCR-CGHAZ has the most refined microstructure among the CGHAZ regions while the SC-CGHAZ and IC-CGHAZ tend to exhibit larger martensite blocks, with equivalent widths for both zones. Also, we may notice that the application of higher heat-inputs can promote the obtainment of a coarser microstructure, represented by the increment in width of the martensite blocks. An inverse correlation between the coarser microstructure and the microhardness values was found. As coarser as the microstructure is, it would exhibit lower

microhardness, a relation observed while evaluating the increase in heat-input, which promotes the decrease in microhardness values of all CGHAZ regions. Also, when evaluating the different CGHAZ regions on the same sample, it is observed that the variation of microhardness values follows a strong relation with the martensite blocks width: presenting considerably lower block width values, the SCR-CGHAZ exhibit much higher microhardness values, while the coarser regions, composed by the SC-CGHAZ and the IC-CGHAZ, are softer, with the SC-CGHAZ presenting slightly wider martensite blocks, and also slightly lower microhardness values.

Figure 26 – IPF maps of the SC-CGHAZ (a), the IC-CGHAZ (b), and the SCR-CGHAZ (c) for the low heat-input welding condition. The grain boundaries of each map are shown in Figure 26d-f.

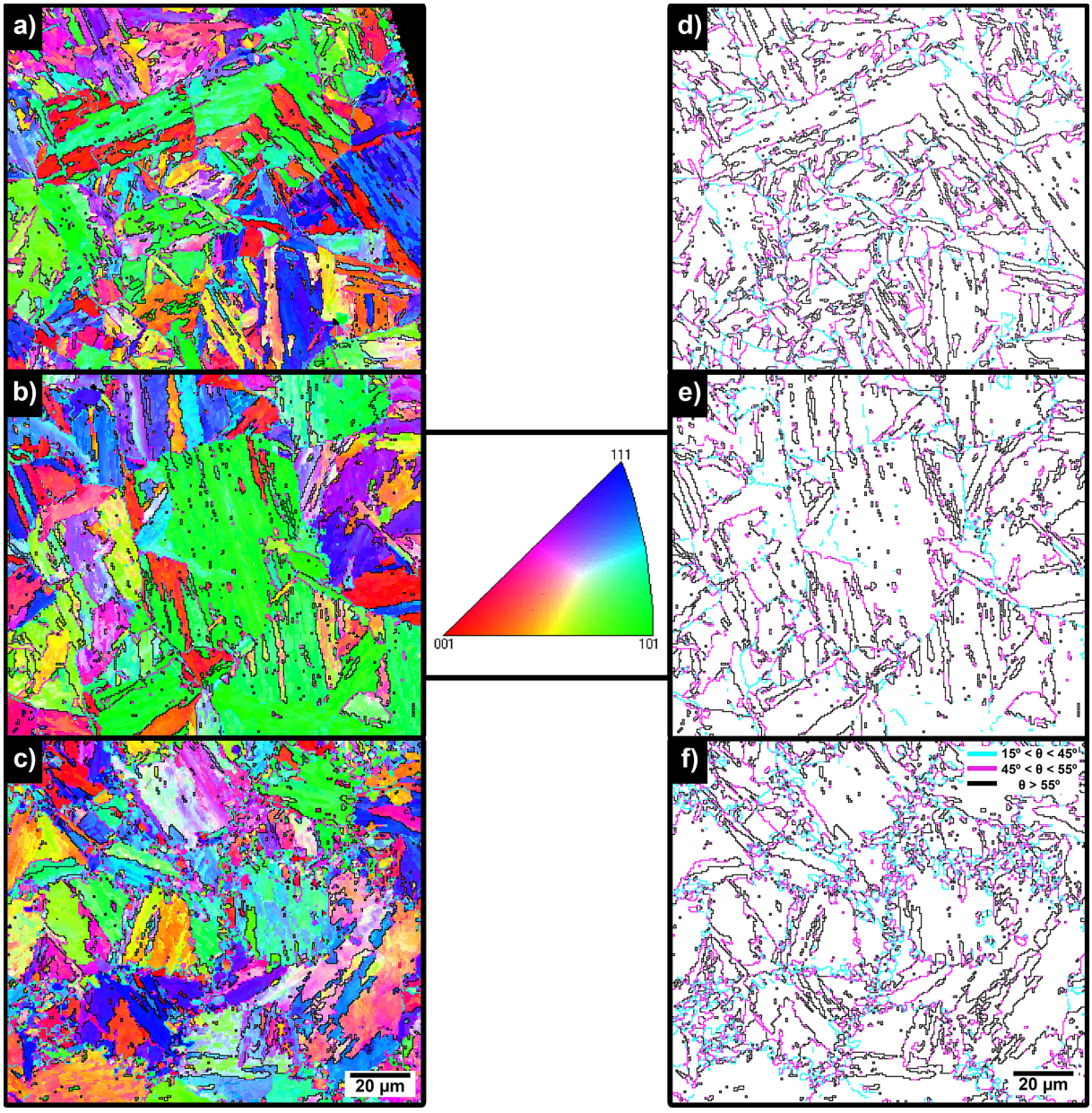

Source: Own elaboration.

Regarding the area fraction of coarse martensite laths, multiple high-resolution SEM micrographs in secondary electron mode were evaluated, resulting in the cover of at least 22,000 μm^2, in each CGHAZ region, for the quantification of the area fractions. As an example of the evaluated images, Figure 28 exhibits micrographs of the three CGHAZ regions for the high heat-input welding condition, where the dashed lines outline the coarse martensite laths. The results obtained through the quantification are summarised in Table 5, which reveals a significant decrease in the area fraction of coarse laths for the SCR-CGHAZ. This behaviour certainly contributes to the higher microhardness values of this region in comparison to the SC-CGHAZ and IC-CGHAZ, which present similar values of coarse lath area fraction on each of the evaluated conditions. Furthermore, it can also be noticed that increasing the heat-input enlargers the fractions of coarse lath in all of the CGHAZ zones. This outcome agrees with the results of Morsdorf *et al.* (2015), which suggested that higher austenitization temperatures would guarantee a softer austenite matrix that imposes less resistance to the coarse laths growth, resulting in microstructures with larger coarse lath area fraction.

3.4.3 Mechanical response

By relating the microhardness values to the yield strength, we may discuss the observed microstructural features' contribution to the local mechanical properties of the CGHAZ regions. In steels, the yield strength (σ_y) can be evaluated as a sum of strengthening mechanism which contributes to hindering dislocation slip:

$$\sigma_y = \sigma_0 + \sigma_{ss} + \sigma_{gs} + \sigma_{dis} + \sigma_{ppt}, \tag{3.1}$$

where σ_0 is the intrinsic lattice friction of pure iron, and σ_{ss}, σ_{gs}, σ_{dis} and σ_{ppt} are the strengthening from solid solution, grain size, dislocation and precipitation, respectively (YU *et al.*, 2018; HOU *et al.*, 2020).

Solid solution strengthening may be closely related to the type and the concentration of the alloying elements (XIAO *et al.*, 2016). However, the complexity of the microstructure and the composition of lath martensitic steels made it challenging to clarify this hardening mechanism. It is known that the mechanical properties of martensitic steels are significantly impacted by the distribution of C atoms in the microstructure and the eventual precipitation of carbides during the tempering process (HUTCHINSON *et al.*, 2011). Exhibiting high martensite start temperature – approximately 330 °C (FONDA; SPANOS, 2014) –, 9Ni steels undergo

an unavoidable autotempering during quenching, which is especially observed at the coarse laths, microconstituents that form close to the martensite start temperature (MORSDORF *et al.*, 2015). According to Morsdorf *et al.* (2021), this phenomenon induces the decomposition of the Zener-ordered supersaturated lattice, leading to agglomeration of C atoms in BCT clusters within the BCC matrix. These clusters may further evolve into transition carbides and precipitated cementite, with the C atoms diffusing and agglomerating along dislocations to form cementite nuclei. This carbon redistribution will reduce the C supersaturation in the vicinity of dislocation cores which act as carbon sinks.

Figure 27 – Boxplots representing the martensite blocks width distribution on the different CGHAZ regions, and microhardness values tendency between those regions. The blue cross markers represent outliers. Measurements taken over the samples of low (a), medium (b) and high (c) heat-inputs.

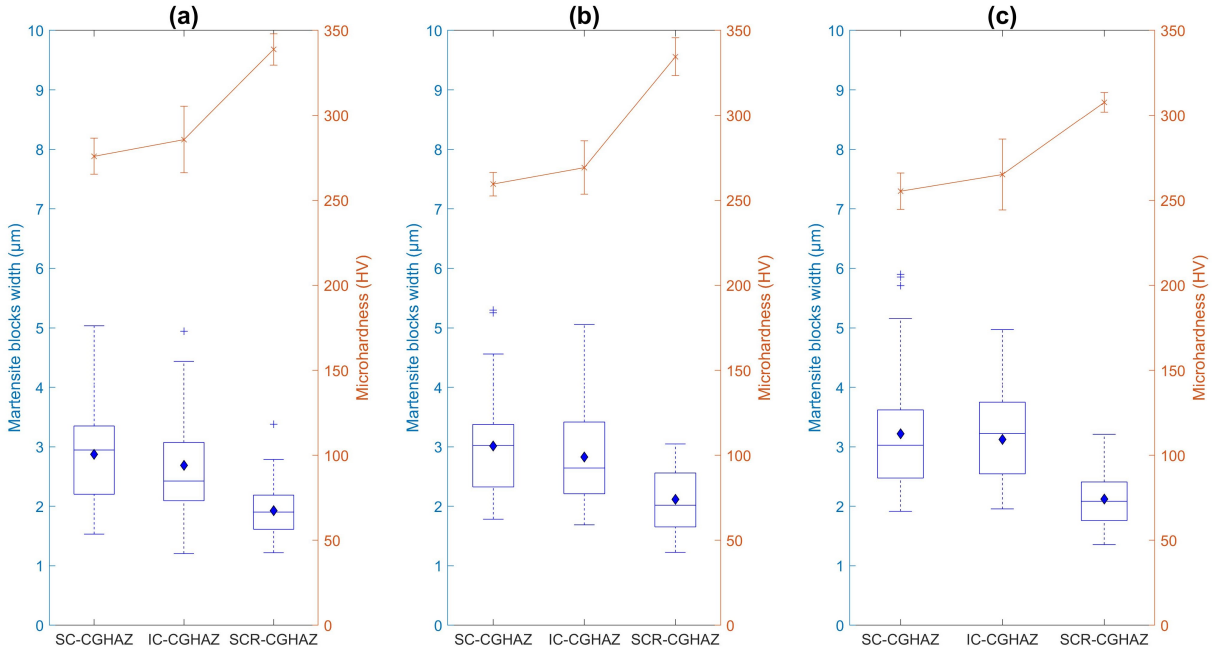

Source: Own elaboration.

The carbon distribution is already complex in an as-quenched condition, with even a single PAG experiencing a wide range of autotempering levels. With the reheating cycles induced by the multipass welding, the HAZ will be submitted to further tempering effect. At the CGHAZ, this tempering will produce the SC-CGHAZ, where the reheating will contribute to the decomposition of the supersaturated lattice and the formation of carbides, resulting in a relatively soft region. In contrast, the SCR-CGHAZ is the closest to an as-quenched condition that we may observe at the CGHAZ. This region presents a considerably higher hardness, with a possibly higher fraction of C supersaturated thin laths – it is important to note that the SCR-CGHAZ

also undergoes an autotempering effect, as carbide precipitation is observed within the coarse martensite laths of this region (Figure 24f).

Figure 28 – Large field of view SEM images in secondary electron mode highlighting the coarse laths in SC-CGHAZ (a), IC-CGHAZ (b) and SCR-CGHAZ (c) for the high heat-input condition.

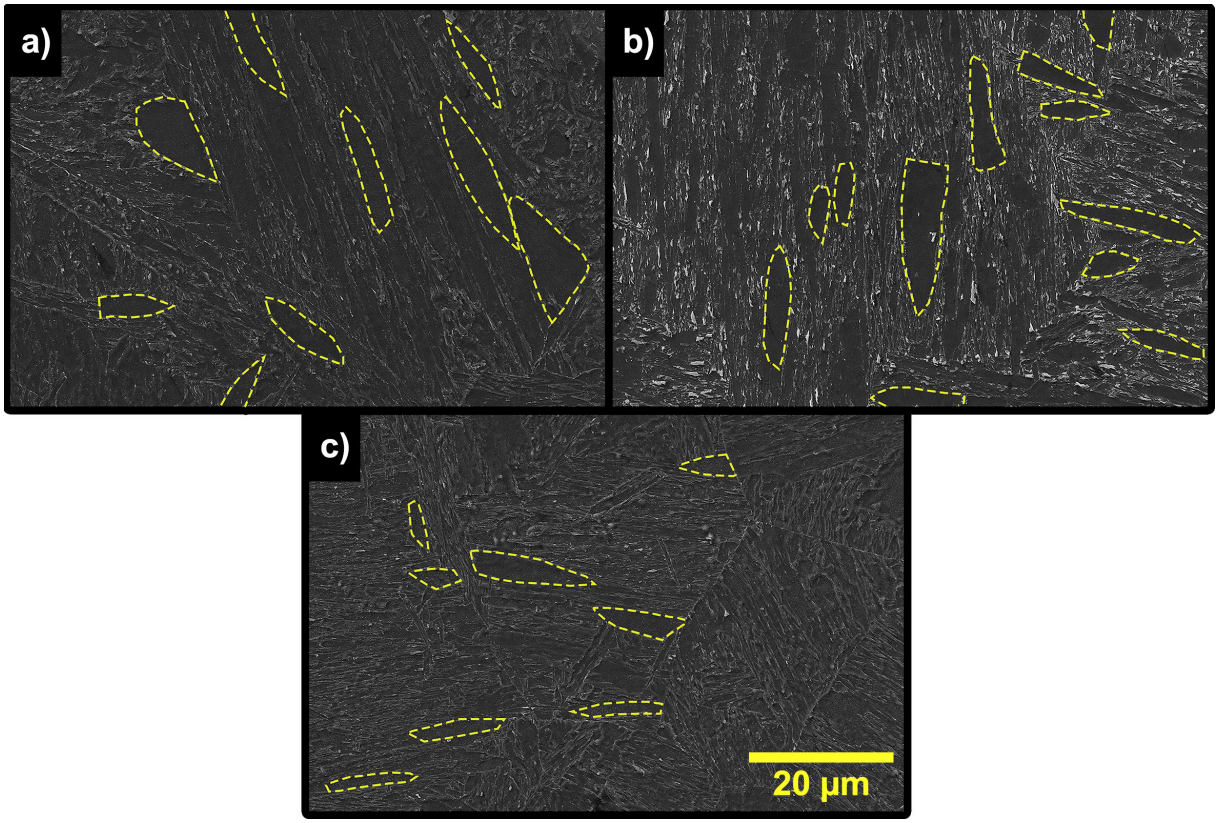

Source: Own elaboration.

The Hall-Petch equation has been commonly used to express the effect of grain size on steel strengthening:

$$\sigma_{gs} = K_{hp} d^{-1/2}, \tag{3.2}$$

where K_{hp} is the Hall-Petch coefficient and d is the mean value of the effective grain size. The effective grain size in lath martensite steels is usually attributed to the block size since the block boundaries are considered the smallest crystallographic discontinuity able to pin or significantly impair the dislocation mobility, following a consistent Hall-Petch relationship (MORRIS, 2011; LONG *et al.*, 2016). As shown in Figure 27, martensite block widths along the CGHAZ influence the local mechanical properties. The block refinement promoted by the superposition by FGHAZ or by applying a lower heat-input may increase the microhardness values of the HAZ. Although the Hall-Petch equation describes the connection between the effective grain size and the yield strength, it is recognised that the hardness measures a material's plastic flow resistance and is,

therefore, a function of yield strength and strain hardening. Considering the proportionality between microhardness and yield strength, it is possible to evaluate that the results initially presented in Figure 27 follow a strong Hall-Petch relationship, as exhibited in Figure 29a. The variation in martensite block width promoted by differences in welding pass superpositions and heat-input conditions draws a consistent Hall-Petch relationship which corroborates with the results of studies which has performed actual uniaxial tensile experiments to verify the effects of the lath martensite hierarchical microstructure on the mechanical properties of lath martensite steels (MORRIS, 2011; LONG *et al.*, 2016; LUO *et al.*, 2020).

Regarding dislocation strengthening, this mechanism may also be partially related to the morphological aspects of the lath martensite microstructure. Morsdorf *et al.* (2015) developed extensive characterisation work towards the lath martensite constituents, identifying the coarse laths as a low dislocation density zone, which presents itself as "soft" microconstituents dispersed inside a much harder matrix composed of thin martensite laths. The authors formulate that this condition is a result of the martensite transformation sequence, in which the coarse laths are the first martensite constituents to grow into the initially "soft" austenite grain. As they grow and the temperature decreases, the significant increase in dislocation density of the highly constrained untransformed austenite will inhibit further coarse lath growth – which will undergo an autotempering process – and catalyse the nucleation of thin martensite laths, that will exhibit significantly higher dislocation density in comparison to the coarse martensite laths (MORSDORF *et al.*, 2015; SHAMSUJJOHA, 2020). Morsdorf *et al.* (2015) also observed that the coarse lath area fraction increases with the PAG size, a factor related to the increase in martensite start temperature, which contributes to the lower resistance of the initial austenite structure. These observations suggest that the CGHAZ would present the highest coarse lath area fraction along the HAZ, which is observed, with the SC-CGHAZ and the IC-CGHAZ exhibiting higher values of coarse lath area fraction – and also lower microhardness values – for all welding conditions (Table 5). However, those high fractions are not observed at the harder SCR-CGHAZ, which corresponds to a CGHAZ region submitted to reheat at low supercritical temperatures, promoting the complete austenitization and the refinement of this zone. The refined austenite grains obtained during reheating will hinder the coarse martensite lath growth during the subsequent cooling, resulting in the low coarse lath area fraction values observed in Table 5. The welding heat-input effect is also observed in the values presented in Table 5. As expected, a higher heat-input will promote the formation of larger PAGs at the CGHAZ,

increasing the coarse lath area fraction on the final microstructure. This effect seemingly extends to the SCR-CGHAZ, which exhibited a significant increase in coarse lath area fraction for the high heat-input condition.

Figure 29b shows the relationship between the local microhardness and the coarse lath area fraction, exhibiting values for all of the evaluated CGHAZ regions in each welding condition. Considering the same CGHAZ region at the different welding conditions, it is verified that the increase in heat-input promotes the increase in coarse lath area fraction, which is followed by the decrease in microhardness values. Also, when comparing the different CGHAZ regions in the same heat-input condition, it is observed that the lower microhardness values are obtained in the regions with a larger area fraction of coarse lath. As exhibited in Figure 29b, this relationship follows a strong linear tendency; however, it is difficult to measure the impact of the coarse lath at the local mechanical properties, as its area fraction increment is usually followed by an increase in martensite block size. Both observations seem to promote a decrease in microhardness values, indicating that grain size and dislocation strengthening significantly contribute to the local mechanical properties.

Table 5 – Mean values of coarse lath area fraction.

	SC-CGHAZ	IC-CGHAZ	SCR-CGHAZ
Low heat-input	5.6%	5.3%	1.4%
Medium heat-input	6.1%	6.5%	1.9%
High heat-input	7.4%	7.2%	3.6%

Source: Own elaboration.

Besides the morphological aspects, the precipitation pattern also presents itself as a microstructural feature capable of promoting the observed heterogeneity in HAZ microhardness values. When comparing Figures 24c and 24d to Figures 24a and 24b and Figures 24e and 24f, the effects of an intercritical reheating on the precipitation interlath and intralath martensite structure are clearly observed. In the martensite transformation sequence, the coarse laths are the first constituents to transform from the prior austenite grain, being subjected to an auto-tempering process during the subsequent cooling. As a result of this low range diffusion process, nanocarbides precipitate in the interior of the initially supersaturated coarse martensite lath, as exhibited in Figures 24a and 24f. These microstructural features agree with previous studies performed by Morsdorf *et al.* (2015). When this constituent is submitted to reheating at intercritical temperature, the energy provided is high enough to promote the dissolution of these carbides and the C atoms diffusion to the coarse laths boundary. The accumulation of carbon along with these

boundaries leads to the carbon clustering, which subsequently can nucleate reverted austenite. Additionally, the segregation of C atoms to dislocations and boundaries can fastly diffuse it towards the retained austenite, previously formed under the quench. This carbon enrichment will act on stabilising reverted and retained austenite, resulting in a seemingly featureless coarse lath surrounded by a microstructure containing C-rich retained/reverted austenite particles, as registered in Figures 24c and 24d. This microstructural landscape described here for the 9Ni steel HAZ has some similarities with some studies on lath martensitic steels that have characterised the observed constituents as retained/reverse austenite particles (FULTZ *et al.*, 1985; FULTZ *et al.*, 1986; ZHANG, 2012; ZHANG *et al.*, 2013; JAIN *et al.*, 2017; JAIN *et al.*, 2018).

Figure 29 – Plot of microhardness vs reciprocal square root block width (a) and plot of microhardness vs coarse lath are fraction (b) at the CGHAZ regions in each evaluated condition.

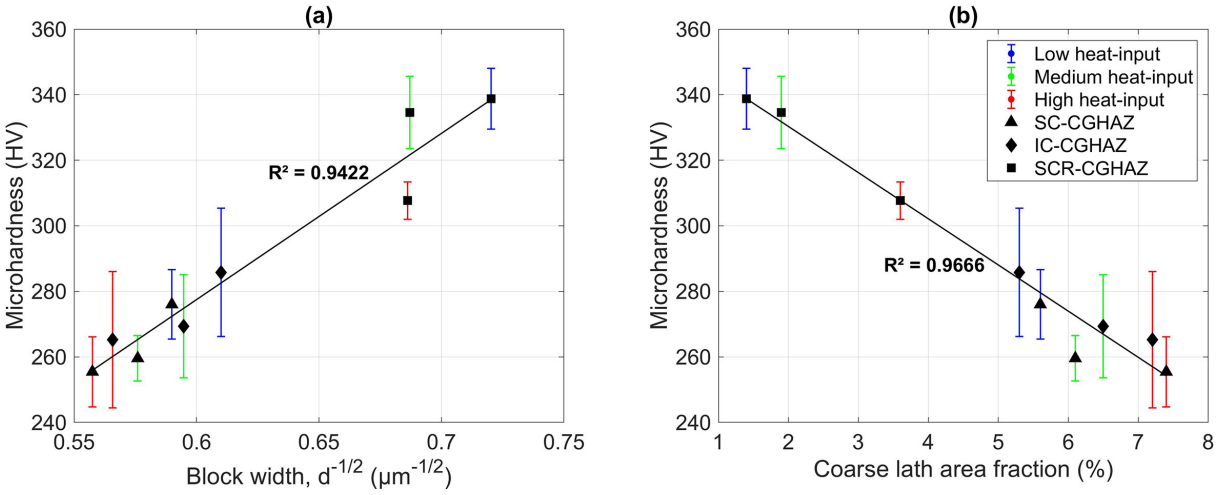

Source: Own elaboration.

Nonetheless, those austenite structures are also quite similar to the microconstituents characterised by Ramachandran *et al.* (2020) as necklace-type M-A (red arrows in Figure 24c) and slender-type M-A constituents (blue arrows in Figure 24c). These M-A constituents are considered deleterious structures capable of significantly reducing the toughness due to the significant hardness difference between the M-A and the surrounding matrix microstructure, acting on crack initiation mechanisms (LEE *et al.*, 2018; RAMACHANDRAN *et al.*, 2020). This assumption agrees with previous reports that have characterised the IC-CGHAZ as LBZ within the HAZ of 9Ni steel welded joints, relating this observation to the chemical composition of M-A constituents (JANG *et al.*, 2002; JANG *et al.*, 2003).

Also, regarding the intercritical reheating effects over the lath martensite microstructure, it is clear that the partial austenitization is responsible for the precipitation of fresh martensite

along the PAG boundaries, as indicated by the yellow arrows in Figure 24c. The presence of these hard supersaturated martensite constituents may explain the high deviation of microhardness values observed in the IC-CGHAZ for all the heat-input conditions, resulting in the slightly higher mean microhardness value in comparison to the SC-CGHAZ.

Concerning the SCR-CGHAZ, the refined microstructure impacts the dispersion of precipitates, as the precipitation mainly occurs at the microstructural interfaces (HUTCHINSON *et al.*, 2011; SHAMSUJJOHA, 2020). Be that as may, the precipitation hardening may be blurred by the grain size hardening. Also, the proper evaluation of the hardening promoted by the nanocarbides located within the coarse laths demands high spatial resolution mechanical testing to probe the microconstituents.

3.5 Conclusion

The present work conducted a microstructural and micromechanical investigation along the HAZ of 9Ni steel pipes multi-pass girth welds, revealing features related to reheating cycles and heat-input conditions. This study yielded the following conclusions:

a) The reheating cycles imposed by subsequent welding passes are the most impacting factors on the local microhardness, standing out in comparison to the impact of the prior microstructure, resulting in the obtaining of hard and soft layers that reach out the entire radial extension of the HAZ.

b) The highest microhardness values, for all welding conditions, are founded at the SCR-CGHAZ – agreeing with the analysis at the cap passes, which exhibit the FGHAZ as the hardest HAZ region –, while the SC-CGHAZ and the IC-CGHAZ exhibit lower microhardness values, although the later presents a high deviation that is probably related to the presence of hard fresh martensite and C-rich retained/reversed austenite particles at the intercritically reheated zone.

c) The variation in the mechanical response of the CGHAZ regions is mainly related to the grain size strengthening, as the martensite block refinement promoted by reheating and by heat-input condition follows a strong Hall-Petch relation, and to the coarse lath area fraction, as these microconstituents are characterised as "soft" zones of low dislocation density.

d) Although it is expected that the precipitates would act in the alloy strengthening, the evaluation of this hardening mechanism is hindered by the precipitation

pattern at the microstructure interfaces, which may blur the line between grain size strengthening and precipitation strengthening. The effect of the precipitates is observed at the IC-CGHAZ, where the intercritical reheating promotes the dissolution of the nanocarbides within coarse laths and may contribute to the stabilisation of C-rich retained/reversed austenite particles.

4 PLASTICITY OF COARSE MARTENSITE LATHS WITHIN THE HEAT-AFFECTED ZONE OF 9NI STEEL GIRTH WELDED PIPES

4.1 Abstract

Presenting a low DBTT compared to other BCC structural steels, lath martensitic steels, such as 9Ni steels, are the most prominent high-strength steels proposed for low-temperature and cryogenic services. In the past couple of decades, broad access to tools and instrumentation required to map complex crystallographic relations allowed authors to draw several relations between the lath martensite microstructure and the mechanical properties of those steels. Recently, morphological heterogeneity of lath martensite microstructure has been pointed out as a microstructural feature responsible for the scattering in local yield strength within the microstructure, with coarse martensite laths acting as soft zones with enhanced deformation ability. The present work conducts an investigation covering macro- to micro-plasticity of 9Ni steel welded joints, focusing on the HAZ and the contribution of these coarse laths to the strain mechanisms of the microstructure. Tensile tests and EBSD analyses were conducted over a selected area in tensile specimens at progressive strain levels. Local strain measurements revealed that the CGHAZ is the only HAZ region that experiences significant strain, with the SC-CGHAZ presenting the highest strain levels. Regarding the coarse lath contribution, EBSD analyses revealed that, up to 7% strain, these coarse constituents present a progressive increase in GND density increasing rate, indicating that they may carry plasticity for even further stages of plastic regime. However, at the very beginning of plastic deformation, dislocation activity is mostly observed at thin lath areas due to the deformation-driven martensitic transformation of interlath austenite films.

Keywords: 9Ni steels. Heat-affected zone. Lath martensite. Plasticity. Electron backscatter diffraction.

4.2 Introduction

Lath martensite plays a significant role in structural materials selection as the main strength-providing microconstituent in high-strength steels. Lath martensitic steels have important technological implications for fracture phenomena: presenting a low DBTT compared to other BCC structural steels, lath martensitic steels are the most prominent high-strength steels proposed for low-temperature and cryogenic services (MORRIS, 2011). Among those alloys,

9Ni steel stands out for its excellent toughness in temperatures as low as -196 °C (SHIN *et al.*, 2000), being commonly applied in the storage and transportation of liquefied gases in the oil industry (FARIAS *et al.*, 2018).

Despite the long history and use of low-carbon Ni-alloyed steels and other lath martensitic steels, it was only in the last couple of decades that the broad access to tools and instrumentation required to map complex crystallographic relations allowed the discussion of fundamental mechanisms of lath martensite plasticity based on quantitative evaluations. Morito *et al.* (2003) and Kitahara *et al.* (2006), developed pioneering research regarding the orientation relationship between the lath martensite and its prior austenite. Based on the K-S OR – $\{111\}_{\gamma} || \{101\}_{\alpha'}$, $\langle 1\bar{1}0\rangle_{\gamma} || \langle 11\bar{1}\rangle_{\alpha'}$ –, the authors described the crystallographic hierarchy that rules the lath martensite microstructure, which is composed by martensite packets that are subdivided into martensite blocks, sub-blocks and thin laths (MORITO *et al.*, 2003; MORITO *et al.*, 2006; KITAHARA *et al.*, 2006). All of the mentioned sub-structures can be observed in a single PAG, presenting boundaries whose misorientation level follows the hierarchy.

Since the establishment of the lath martensite hierarchy, several studies have been carried out to draw microstructure-mechanical properties relationships (YU *et al.*, 2018). Within this hierarchical microstructure, the high-angle block boundaries were found to be the main microstructural interface responsible for the restriction of slip transmission, an observation that led to the determination of the block size as the effective grain size in lath martensitic steels (SHIBATA *et al.*, 2010; MORRIS, 2011; DU *et al.*, 2016a; LONG *et al.*, 2016). Michiuchi *et al.* (2009) verified the preference in the activation of slip systems with Burgers vector parallel to lath interfaces (in-lath-plane slip system), suggesting that, although the laths of a single martensite packet share the same parallel slip plane, the slip direction may diverge between the martensite blocks within this packet, resulting in different Schmid factors and the consequent activation of different slip systems, which, in turn, will lead to heterogeneity in the deformability between blocks of the same packet (MORSDORF *et al.*, 2016). Also, several studies were developed towards the retained austenite – which for a long time was considered to be the primary toughness provider in lath martensitic steel (MARSHALL *et al.*, 1962; STRIFE; PASSOJA, 1980; AHSAN *et al.*, 2014) –, that, being present as interlath films, may act as a "viscous plane" on which the adjacent laths would slide through (MARESCA *et al.*, 2014). This mechanism, however, must not be a determining factor throughout the whole plastic deformation process, as the retained austenite may undergo a martensitic transformation induced by plastic deformation at the early

stages of the plastic regime (MORSDORF *et al.*, 2016).

Clearing the relationship between microstructure and mechanical properties of lath martensitic steels is still a work in progress, as the relevance of many microstructural features and strain mechanisms continues to be evaluated. One relatively recent exposed microstructural feature is the presence of auto-tempered coarse martensite laths within a matrix of much finer laths (FONDA; SPANOS, 2014). Morsdorf *et al.* (2015) carried out an extensive characterization of these microconstituents, identifying them as early transforming martensite structures with low dislocation density that were subjected to an auto-tempering process during subsequent cooling. The coarse laths present themselves as "soft" zones inside a much harder matrix, a configuration that motivates to interpret the lath martensite as a nano-composite structure (MORSDORF *et al.*, 2015; BADINIER *et al.*, 2015). Regarding the plasticity, the heterogeneities associated with the coarse martensite laths may act in the scattering in local yield strength within the microstructure (MORSDORF *et al.*, 2016). It is expected that the deformability of these constituents would be enhanced in comparison to the matrix; however, the coarse laths do not necessarily improve the toughness of lath martensitic steels, as they act as sites with a low resistance to crack propagation (MORSDORF *et al.*, 2016; UEKI *et al.*, 2020).

Although coarse martensite laths have been identified at the HAZ in the welding of low-carbon Ni-alloyed steels (BARRICK *et al.*, 2017; BARRICK; DUPONT, 2019), the effects in mechanical properties, as well as the strain mechanisms acting in those constituents, haven't been appropriately evaluated under the welding metallurgy perspective. Recently, coarse microconstituents, resembling coarse martensite laths, have been reported in studies towards the HAZ in the welding of 9Ni steels (FERNANDES *et al.*, 2020; RIOS *et al.*, 2021); however, the authors have labelled it as coalesced bainite. This study aims to clarify the contribution of coarse martensite lath to the plasticity and the mechanical properties of the HAZ of 9Ni steel girth welded pipes. Weld tensile specimens were submitted to progressive tensile tests and analyses through detailed EBSD analyses in a *quasi-in-situ* procedure, enabling the evaluation of the microstructure and the local strain evolution during the plastic deformation of the welded joint.

4.3 Experimental procedure

In this work, tensile specimens were extracted from two distinct girths welded joints, both with quenched and tempered ASTM A333 Gr.8 (9Ni) steel as Base Metal (BM) and Ni-based superalloy Inconel 625 (AWS ER NiCrMo-3) as the filler metal (chemical composition

presented in Table 6). The chemical composition of the 9Ni steel pipes (Table 7) was evaluated through optical emission spectroscopy, with a Shimadzu PDA-7000. The welding procedure was conducted in a robotic workbench equipped with a Markle HighPULSE 550 RS power source, a KUKA KR16 robot, and a KUKA DKP-400 positioner. GMAW was applied for both girth welds; however, different heat-input conditions were imposed for fill and cap passes of each welded joint. One of them was welded with a heat-input equal to 1.5 kJ/mm, while the other one was welded with 2.5 kJ/mm of heat-input. The arc potency parameters remained constant while changing the welding speed.

Table 6 – Typical weld metal analyses (wt.%) of the AWS ER NiCrMo-3 (recap).

C	Mn	Si	Ni	Cr	Mo	Nb	Fe
0.09	0.05	0.12	Bal.	21.90	8.70	3.65	0.62

Source: WELDWIRE (2021).

Table 7 – Chemical composition (wt.%) of the ASTM A333 Gr.8 (9Ni) steel pipes (recap).

C	Mn	Si	Ni	Cr	S	P	Fe
0.032	0.496	0.278	9.460	0.032	<0.005	<0.005	Bal.

Source: Own elaboration.

The cross-sections of the welded joints are presented in Figure 30a. Figure 30b presents the dimensions – in millimetres – of the tensile specimens extracted from the welded joints. Figure 30c shows the machined test specimens. The useful area of the specimen comprises FZ, HAZ, and BM, with the fill passes HAZ located at the gauge length centre.

Initially, one tensile specimen of each condition was submitted to a complete tensile test to obtain the stress-strain curves of the welded joints. The surfaces of these specimens were first grinded in sandpaper and mechanically polished up to 1 μm diamond paste. Then they were etched by immersion in 2% Nital (the result can be seen in Figure 30c). The stress-strain curves were evaluated to predefine the strain level steps to which the specimens destined for the micro-plasticity analyses would be submitted. The tensile tests were carried out in a MTS Landmark 370.10, with 0.5 mm/min crosshead speed. Figure 31 exhibits a specimen with an axial extensometer mounted in its gauge length during the test.

For the specimens destined for the micro-plasticity analysis, the surface preparation took a further step: after the mechanical polishing, the HAZ area located at the gauge length

centre was submitted to a final electropolishing step in a Struers LectroPol-5. The polishing was conducted with a mixture of 70% perchloric acid in 99.8% ethanol in a volume ratio of 1:9, applying 25 V during 50 s, at a temperature of 10 °C. Also, to measure the local strain with high accuracy, low-load (25 gf) microhardness indentations were inserted along the specimens' length at a distance of 150 μm to each other. The insertion of these indentations was automatically conducted in a LECO AMH55 LM-110AT. With the region of interest properly polished, EBSD analyses were conducted to evaluate the initial state of one selected CGHAZ area.

Figure 30 – Cross-sections of the welded joints from the procedures with 1.5 kJ/mm of heat-input (a_1) and with 2.5 kJ/mm of heat-input (a_2). Dimensions of the tensile specimens in millimetres (b). Etched surfaces of the tensile specimens from the conditions of 1.5 kJ/mm of heat-input (c_1) and 2.5 kJ/mm of heat-input (c_2).

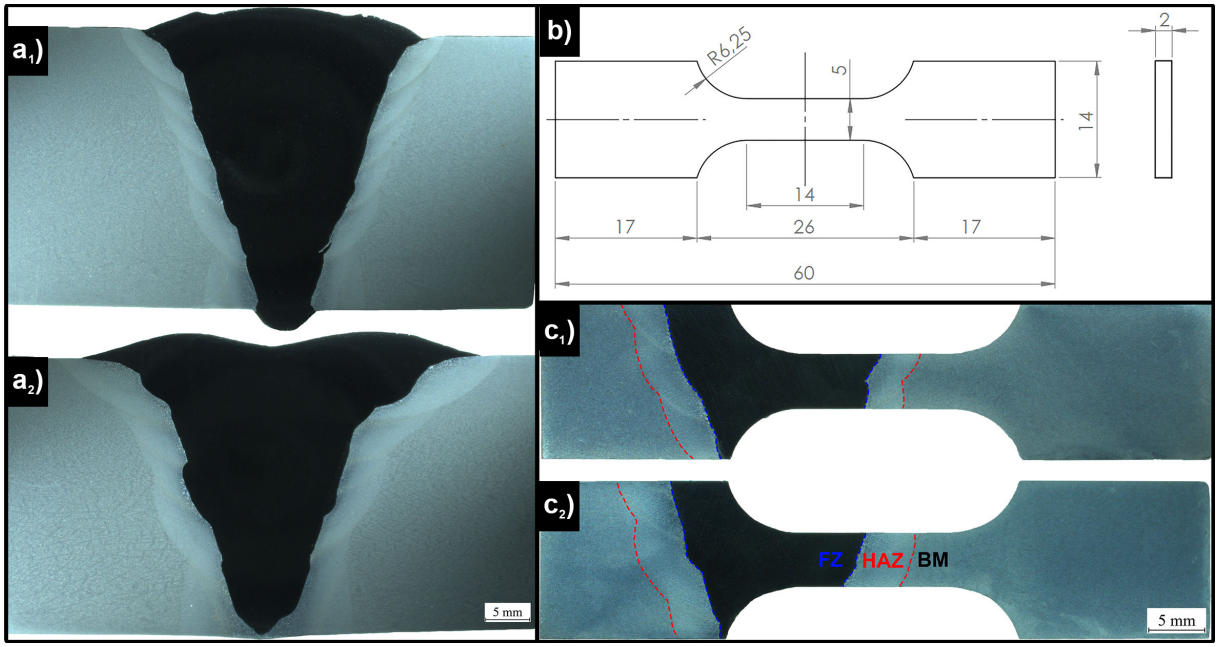

Source: Own elaboration.

After the initial evaluation, the analyses proceeded as follows: the specimens were carefully submitted to a strain increment step, using the same previously mentioned testing machine and monitored by an extensometer, reaching a predefined strain level; the local strain was then calculated through the distance between the microhardness indentations, which was measured through LOM; finally, the specimens were mounted in an SEM to the execution of EBSD analysis over the selected area. This process was repeated four times, resulting in the evaluation of five different strain levels, as shown in Table 8.

The EBSD analyses were carried out in a FEI Quanta 250 SEM coupled with an Oxford Nordlys Max EBSD detector operated at 20 kV. All of the analyses were conducted over

the same area, aiming to evaluate the strain evolution in the microstructure, applying a step size of 100 nm in each scanning. The primary analysis applied in the evaluation of the micro-strain in lath martensite was the KAM mapping, executed using the Channel 5 package, and the GND mapping, executed using the ATEX software (BEAUSIR; FUNDENBERGER, 2017). For KAM analyses, the values were calculated up to the second-nearest neighbour. The misorientation values above the predefined threshold of 5° were excluded from the calculation, as these points were assumed to belong to adjacent grains or subgrains. The same threshold was applied for the GND analyses, in which a BCC iron Burgers vector with a length of 2.48 Å $(a/2\langle 111\rangle)$ was defined for estimation of GND density values. The local strain was determined through measurements taken with a Carl Zeiss Axiovision Z1M LOM, and the macrographs presented in this work were captured through a Carl Zeiss SteREO Discovery.V12.

Figure 31 – Tensile test set-up.

Source: Own elaboration.

Table 8 – Strain levels resulting from the progressive strain increments imposed to the tensile specimens.

Strain Level	Specimen strain	Local strain	
		1.5 kJ/mm	2.5 kJ/mm
0	0%	0%	0%
1	2.0%	1.24%	2.26%
2	4.6%	2.29%	3.38%
3	8.0%	4.32%	5.48%
4	12.0%	5.92%	6.65%

Source: Own elaboration.

4.4 Results and discussion

4.4.1 Tensile tests

Figure 32 exhibits the stress-strain curves of the specimens submitted to an initial tensile test, while Figure 33 presents macrographs over the fractured tensile specimens. Presenting a lower YS in comparison to the BM and HAZ (AWS, 2011; ASTM, 2018), the FZ was initially subjected to intense plastic strain in both conditions – the lower heat-input (1.5 kJ/mm) and the higher heat-input (2.5 kJ/mm). At the beginning of the plastic stage, the formation of slip bands is observed in this zone. Some of these slip bands are indicated by the arrows in Figure 33c, which exhibits the FZ of the fractured specimen of lower heat input. Thus, the difference between the YS presented in the stress-strain curves (Figure 32), is probably related to the metallurgical aspects of the FZ, deviating from the focus of this work.

Further plastic deformation will proceed on the FZ, even resulting in a discrete necking on this zone, which experiences an intense work hardening. When this work hardening reaches high levels, the mechanical strengthening of the FZ hampers subsequent deformation, and the plastic strain becomes more intense at the BM, resulting in the necking at this zone, where the fracture further occurs, as shown in Figures 33a and 33b.

Figure 32 – Stress-strain curves of the specimens related to the welded joints of both welding conditions.

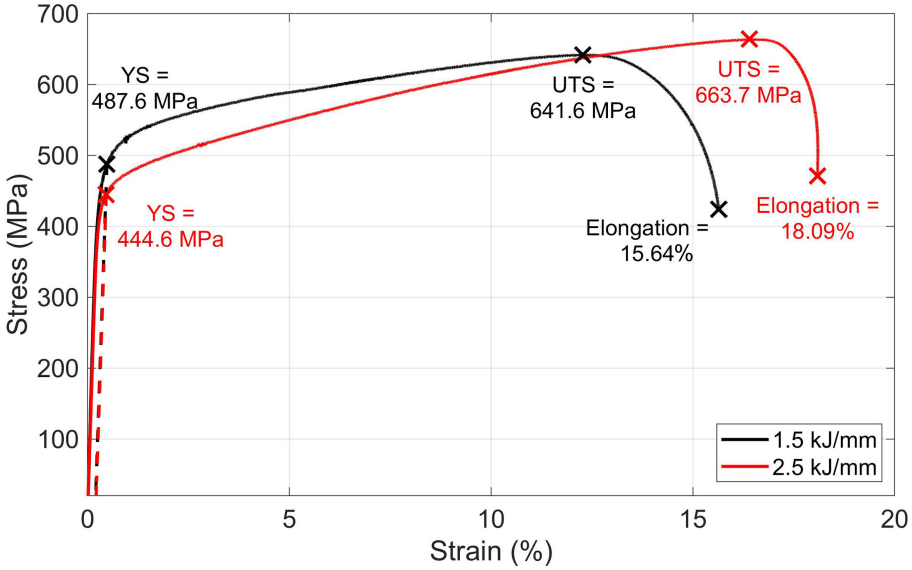

Source: Own elaboration.

Figure 33d shows a ductile aspect of the surface of the fracture that occurs just after the necking at the BM in the lower heat-input specimen. In contrast, the HAZ, the harder zone

of the welded joint, is seemingly submitted to the lower strain levels, being the only region through the gauge length that maintains its stability during the whole tensile test, not undergoing any neck formation. Figure 33e portrays this stability, exhibiting a HAZ between the two neck formations: the necking at the FZ (red arrow) and the BM (yellow arrow).

Figure 33 – Macrographs of the fractured specimens of lower heat-input (a) and higher heat-input (b). Deformed FZ of the lower heat-input specimen. Green arrows indicate the formation of slip-bands in its initially polished surface (c). The fracture surface is located at the BM in the specimen of lower heat-input (d). HAZ in the fractured specimen of lower heat-input (e).

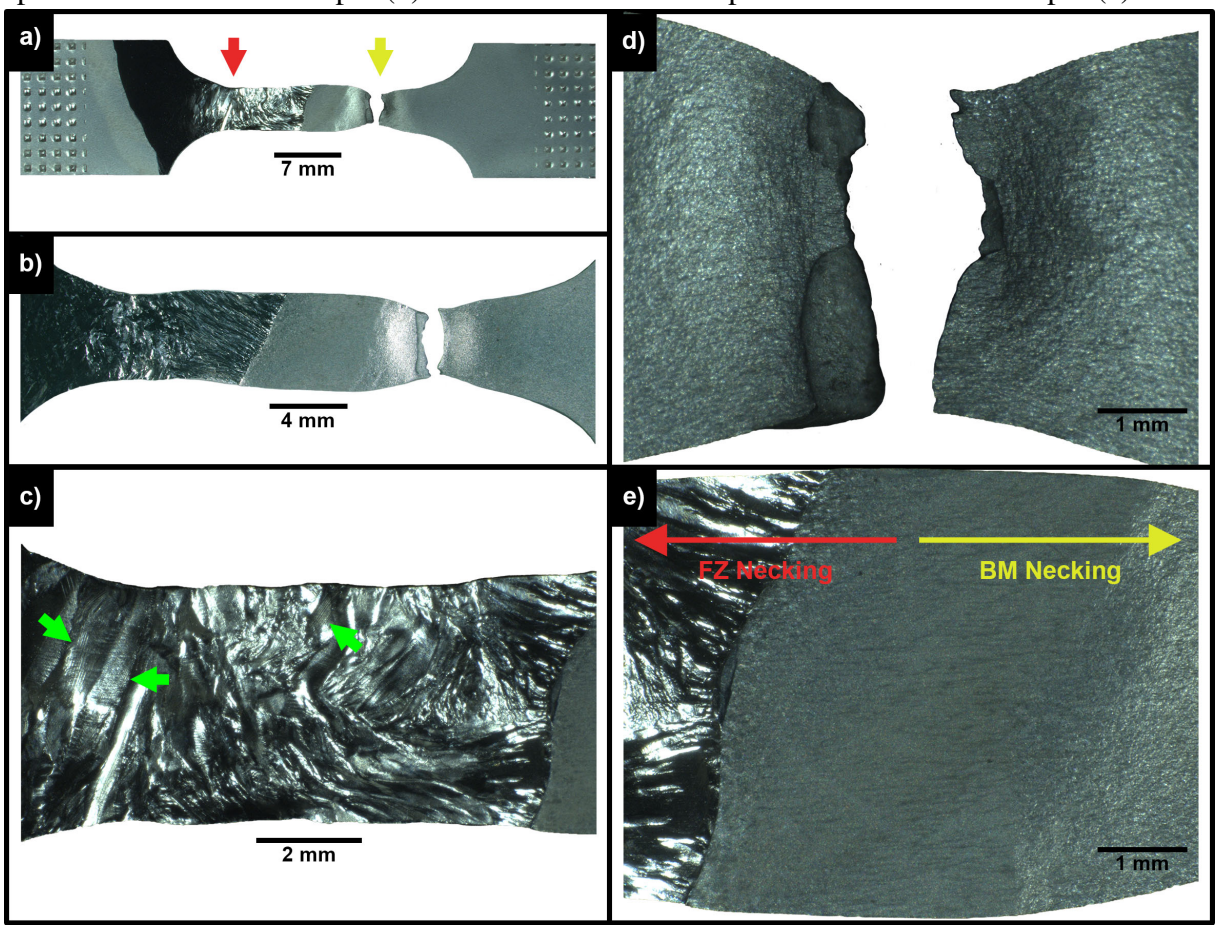

Source: Own elaboration.

It is expected that the metallurgical transformations that occurred at the HAZ would significantly impact the total elongation of the welded joints, which can be observed in the stress-strain curves presented in Figure 32. As shown in previous work (Chapter 3), applying higher heat-inputs will not only result in larger martensite block sizes but also significantly increase the area fraction of coarse martensite laths within the microstructure, microconstituents characterized as soft zones of high deformability within a much harder matrix of thin martensite laths (MORSDORF *et al.*, 2016). These two effects seem to provide a HAZ of higher deformability when welded with higher heat inputs, increasing the total elongation of the welded joint. Even

though the HAZ of these multi-pass welded joints presents a microstructure of high heterogeneity due to the reheating cycles, those effects are observed for all of the HAZ regions, impacting the mechanical properties of the whole zone. However, it is important to consider that the metallurgical aspects of the FZ may also impact the elongation and the Ultimate Tensile Strength (UTS) of the tensile specimens. Thus, it is hard to evaluate the impact of the metallurgical aspects of the HAZ on the mechanical properties of the welded joint in a macroanalysis.

4.4.2 Heat-affected zone plasticity

Aiming to assess the local plastic behaviour of the HAZ, three microhardness indent vectors were placed along the HAZ of the lower heat-input specimen. As represented in Figure 34, all three vectors lay parallel to the gauge length; one was inserted at the center of the gauge width (vector V2), while the other two were inserted at a distance of 1 mm from the top and the bottom edges (vectors V1 and V3, respectively). The first indent of each vector was inserted at 100 μm from the weld interface. The subsequent indents were inserted following a spacing of 150 μm from each other moving towards the BM. Each microhardness vector is composed of 15 indents. The local strain values presented in Figure 34 were calculated through the final (after each strain increment step) and initial distances between neighbouring indents.

Figure 34 exhibits a macrograph of the gauge length overlapped by a microhardness map, which, although it is not the exact microhardness map of the evaluated tensile specimen, is a result of an extensive microhardness analysis over the HAZ of the same welded joint. The positioning of the overlapping map was based on LOM observations and the microhardness values of the indent vectors. Through the representative mapping, it is possible to observe that each vector assesses distinct HAZ regions. Vector V1 begins at the softest region of the CGHAZ, which results from a subcritical reheating ($T < Ac_1$) of this zone, then the vector continues to proceed through a large subcritical reheated area, reaching, at its end, a zone with moderate microhardness values which barely undergoes a significant reheat. Vector V3, in contrast, begins at the hardest region of the CGHAZ, which results from a low-temperature supercritical reheating ($T > Ac_3$) of this zone, proceeding through a short transition zone characterized by a region that undergoes an intercritical reheating ($Ac_3 > T > Ac_1$). The microhardness values begin to decrease as the vector enters a subcritically reheated zone. Finally, vector V2 begins in a transition zone between a FGHAZ and a CGHAZ, undergoing a minor subcritical reheating, and proceeds to a FGHAZ which does not experience any reheating effect imposed by the next

welding pass. An extensive microstructural characterization of the HAZ regions of the evaluated welded joints has been presented in the previous study (Chapter 3).

Through the plots of Figure 34, it is possible to observe that no significant strain is promoted at the HAZ region far from the FZ, which would be composed by the FGHAZ, the ICHAZ, the SCHAZ, and its respective segmentation. This pattern is observed regardless of the microhardness values of those zones. In vector V3, for instance, even being considerably soft, the zones located at 2 mm from the weld interface do not experience any significant strain.

In the previous study (Chapter 3), it was verified that, in a fresh HAZ of a 9Ni steel welded joint (which does not experience any reheating cycle), the FGHAZ presents itself as the hardest region, presenting a very refined lath martensite microstructure with no significant coarse martensite lath area fraction. Although the subcritical reheating is seemingly quite effective in decreasing FGHAZ hardness – as observed through the indents of vector V3 that are farther from the welding interface (Figure 34) – by promoting the diffusion of C atoms in the initially supersaturated structure (MORSDORF *et al.*, 2015; MORSDORF *et al.*, 2021), the refined microstructure maintains the plastic strain resistance of this region. Independent of the reheating cycle, the FGHAZ exhibits greater resistance to plastic deformation compared to its adjacent regions: the much coarser CGHAZ and the softer (and also coarser) BM.

The only HAZ regions that experience significant strain are the CGHAZ and its segmentation. The closer to the weld interface, the higher the strain level to which the CGHAZ is submitted. In contrast to the farther HAZ regions, at the CGHAZ, the microhardness values follow a strong relationship with the observed strain levels: the lower the microhardness values of a CGHAZ region, the higher the strain level it experiences. At a specimen strain level of 12.0%, the SC-CGHAZ may reach 13.2% of local strain (see vector V1 in Figure 34), while the SCR-CGHAZ exhibited 3.04% as its higher local strain value (see vector V3 in Figure 34).

It is expected that the HAZ microstructural features evaluated in previous work (Chapter 3) would play a significant role in this distribution of plastic strain levels throughout the CGHAZ. One of these studied microstructural aspects is the coarse martensite lath area fraction. The study conducted over the same welded joint revealed that this fraction is quite sensitive to the reheating temperature to which the CGHAZ is submitted. For the SC-CGHAZ, which only experience a tempering effect during reheating, the area fraction of coarse martensite laths is, on average, 6.1%, while for the SCR-CGHAZ, which is submitted to a low-temperature austenitization responsible for a significant microstructure refinement, this value decreases to

1.9%. Apparently, coarse martensite laths are microconstituents critical to the HAZ plasticity, which would agree with the proposals by Morsdorf *et al.* (2015), who suggest an interpretation inspired by nano-composite structures, with the coarse martensite laths acting as soft zones of high deformability within a matrix of hard thin laths (MORSDORF *et al.*, 2016).

Figure 34 – Microhardness indent vectors disposed along the HAZ of the lower heat-input specimen. A microhardness map overlaps the macrograph to represent the microstructural heterogeneity resulting from a multi-pass welding process. The plots exhibit the local strain at four steps of progressive strain increments.

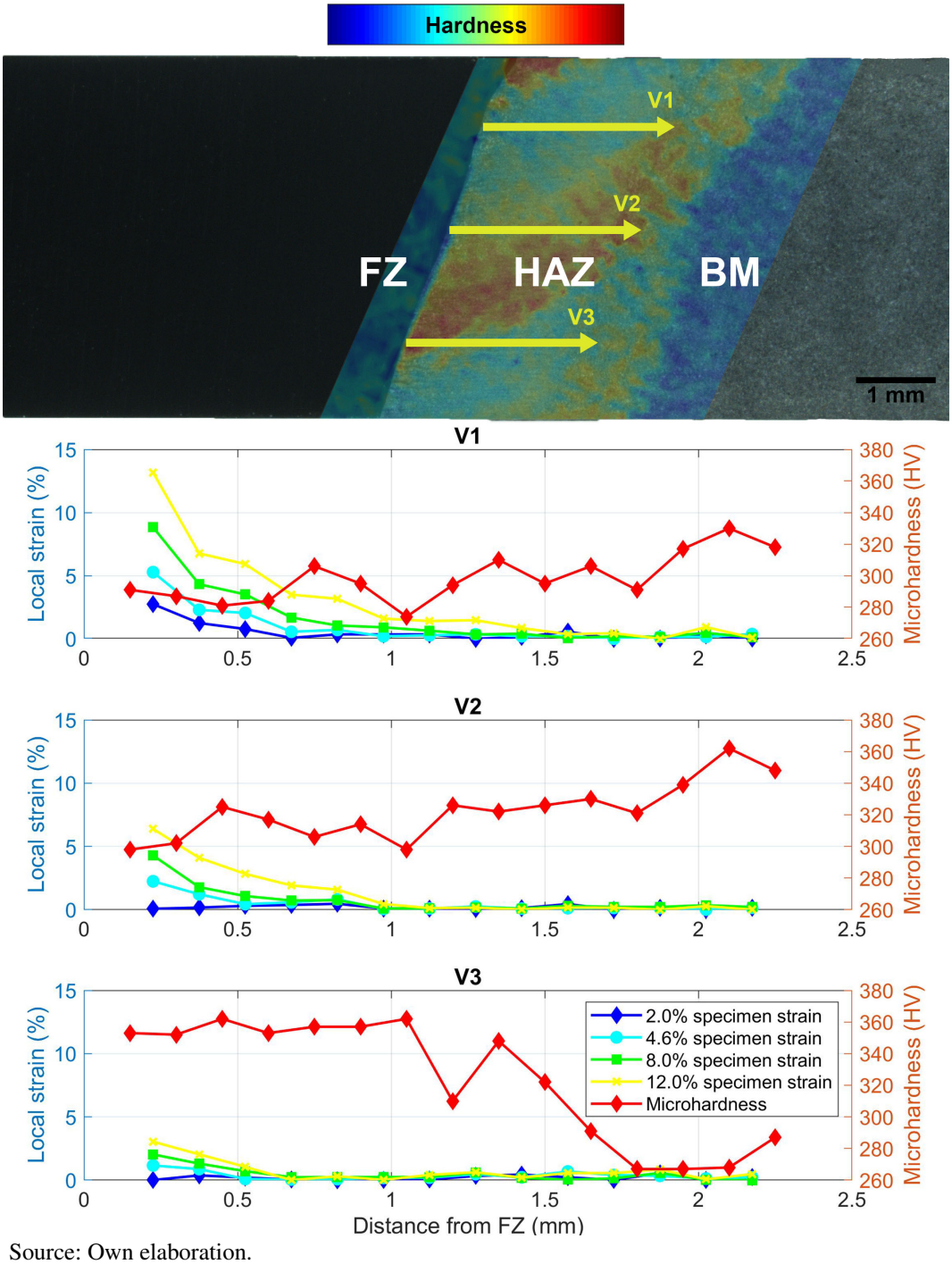

Source: Own elaboration.

4.4.3 Coarse martensite lath plasticity

To evaluate how the coarse martensite laths could contribute to the CGHAZ plasticity, EBSD measurements were taken over one selected area located at the SC-CGHAZ in each tensile specimen. For the lower heat-input tensile specimen, a selected coarse lath is highlighted in Figure 35. In the band contrast map (Figure 35a), the coarse lath presents itself as a bright structure, indicating an low-strained microconstituent (WRIGHT *et al.*, 2011), while, in the KAM map, it presents low KAM values, not only indicating an low-strained microconstituent, but also revealing a structure with low density of GND (CALCAGNOTTO *et al.*, 2010; WRIGHT *et al.*, 2011; SHAMSUJJOHA, 2020). The histograms in Figure 35c compare the KAM values observed within the coarse martensite lath to those observed in the microstructure matrix composed of thin laths, revealing that the average KAM value (θ_{KAM}) is significantly lower in the interior of the coarse laths.

For the higher heat-input tensile specimen, a selected coarse lath is highlighted in Figure 36, which shows that, for the higher heat-input conditions, lower KAM values are observed within both coarse and thin martensite laths (Figure 36c). When comparing the KAM maps in Figures 35b and 36b, one may notice that the higher KAM values tend to be more concentrated at the lath martensite microstructural boundaries when the welding process is conducted with higher heat input, while these high values are visibly more spread throughout the thin laths matrix in the lower heat-input condition. These observations suggest that the lower cooling rates obtained in a higher heat-input welding can guarantee a less strained martensite structure, as significantly lower KAM values are observed for this condition. Also, the larger exposure time to higher temperatures during the reheating cycles may be capable of significantly activating the movement of dislocation (MORSDORF *et al.*, 2015) to the lath martensite microstructural boundaries, which exhibit significantly higher KAM values in comparison to the bulk of the microconstituents, indicating that higher GND densities are observed at those regions (CALCAGNOTTO *et al.*, 2010; SHAMSUJJOHA, 2020).

In both conditions, the selected coarse martensite lath was located at the SC-CGHAZ, between two microhardness indents used as a reference to calculate the local strain. The plastic strain steps were defined according to the total gauge length strain measured by an axial extensometer. Four strain increment steps were taken, stopping the analyses cycle as soon as one of the specimens reached the UTS. Figure 37 shows that the specimen that reached the UTS was the lower heat-input specimen, which surpassed the UTS during the strain increment step

responsible for taking the specimen strain to 12.0%. Both specimens were submitted to the same strain levels; however, due to differences regarding the microstructural aspects, different values of local strain were obtained for each welding condition, as shown in Table 8.

Figure 35 – Band contrast map (a) and KAM map (b) over a selected coarse martensite lath (yellow dashed line) located at the SC-CGHAZ of the lower heat-input specimen. Frequency plot of the KAM values within the coarse martensite lath and within the thin laths matrix (c).

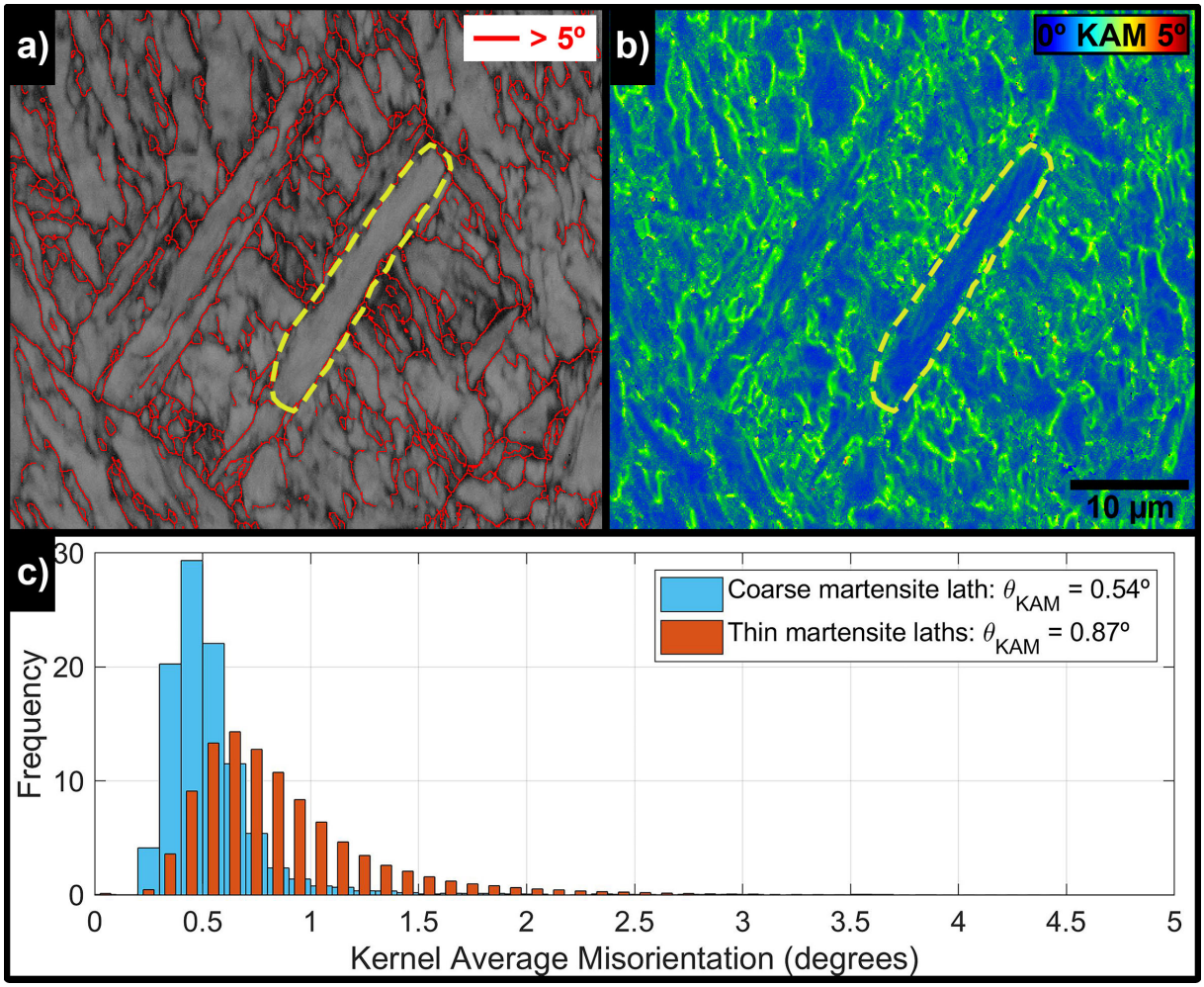

Source: Own elaboration.

Figures 38 and 39 exhibit the evolution of the microstructure regarding the KAM values throughout the progressive specimens deformation. Increasing the local strain increases the KAM values in coarse and thin martensite laths, with the coarse constituent presenting a significantly higher percentage increase. In the analysis over the lower heat-input specimen, the average KAM value of the coarse martensite lath increased by 48.15%, against 26.44% for KAM values of the thin laths matrix. The difference was even higher for the condition of higher welding heat-input, with the coarse constituent presenting a percentage increase of 91.89% in average KAM values against 59.09% for the thin martensite laths.

Figure 36 – Band contrast map (a) and KAM map (b) over a selected coarse martensite lath (yellow dashed line) located at the SC-CGHAZ of the higher heat-input specimen. Frequency plot of the KAM values within the coarse martensite lath and within the thin laths matrix (c).

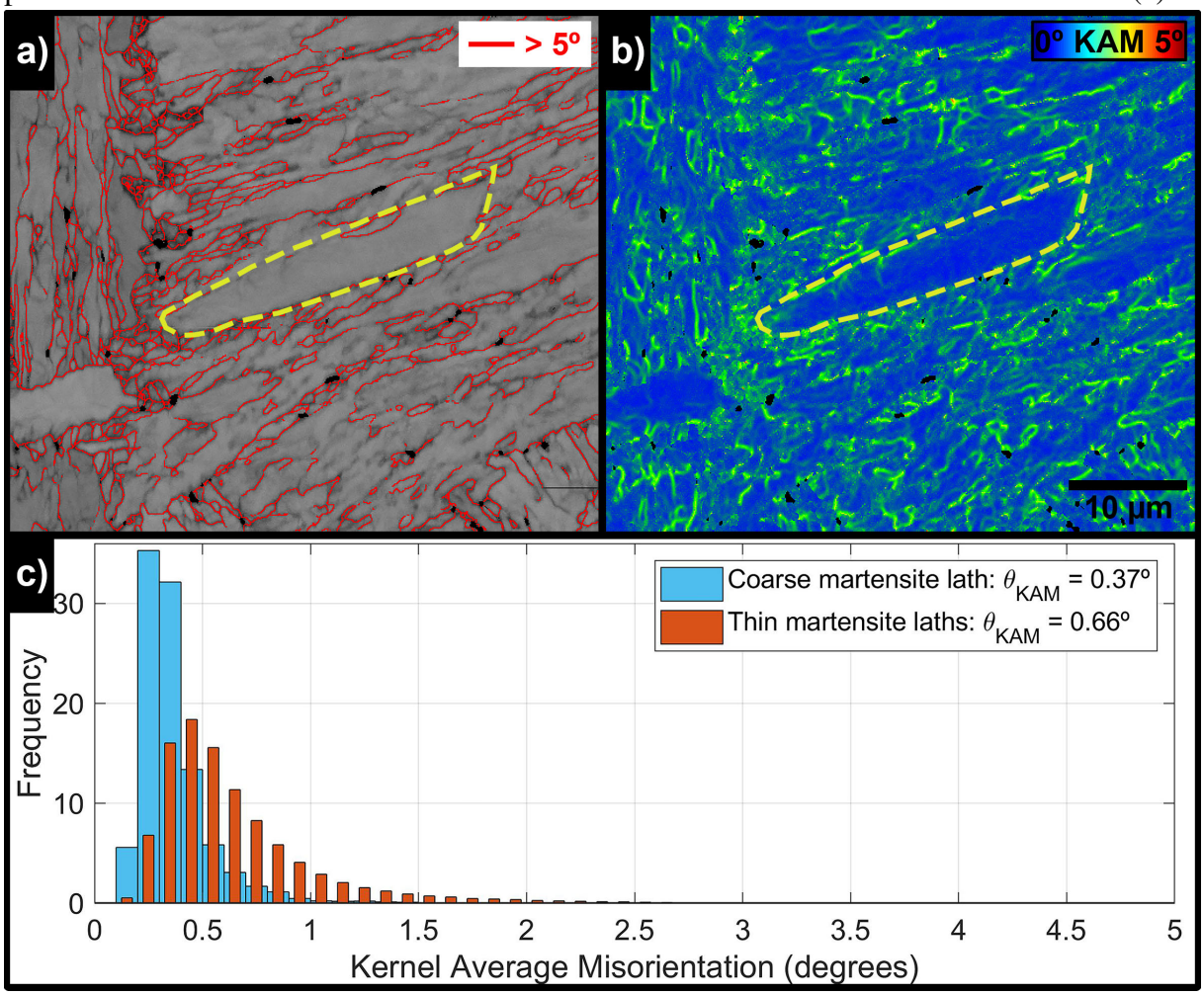

Source: Own elaboration.

Also, the increase in local strain is accompanied by the emergence of non-indexed zones within the thin laths matrix. These zones – highlighted over the maps in Figures 38 and 39 –, do not consist of microvoids, but are areas with high dislocation density and high misorientation level, where weak EBSD patterns are observed, hampering the proper indexation. These areas emerge from regions of initially high deformation and are commonly surrounded by the highest KAM values observed on the presented maps, indicating the higher deformation levels to which the thin laths matrix is submitted when compared to the coarse constituents.

To further assess the plasticity of lath martensite microstructure, GND density maps were estimated from the EBSD orientation data. These maps are presented in Figures 40(k-o), for the lower heat-input condition, and Figures 41(k-o), for the higher heat-input condition. The estimation involves the determination of dislocation density tensor components from the misori-

entation measurements (PANTLEON, 2008; BEAUSIR; FUNDENBERGER, 2017). Evaluating the initial condition (Figures 40k and 41k), it is clear that a lower overall GND density is observed in the higher heat-input welding, which is a result of the lower cooling rate obtained in this process. In both conditions, increasing the local strain through the progressive tensile tests results in the emergence of dark blue areas with significantly low GND density. However, these areas are misleading since they are related to the non-indexed points, which progressively increase along with the strain level and may likely present even higher dislocation densities. Due to this reason, analyses of the GND density evolution were conducted only in the areas highlighted in Figures 40 and 41. These areas were selected based on the GND density maps, while the IPF maps supported the positioning of these subsets, guaranteeing that the same microconstituents were evaluated through all deformation steps.

Figure 37 – Progressive strain increments imposed on the lower heat-input specimen (a) and higher heat-input specimen (b).

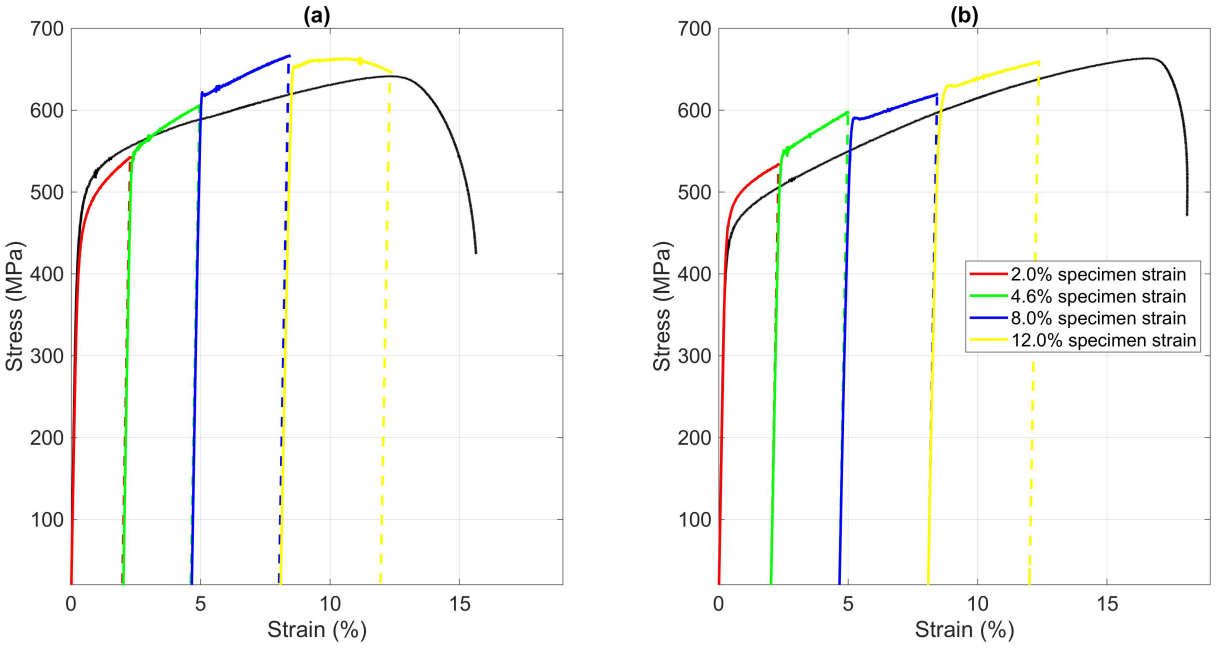

Source: Own elaboration.

Increasing the local plastic strain increases the GND density, which evolves in different manners for coarse and thin laths. As shown in Figure 42, at the early stages of plastic deformation, thin martensite laths exhibit a larger increase in GND density when compared to the one observed at the coarse laths. However, for the later strain increment steps, the GND density at the thin laths tends to exhibit smaller increases, while, at the coarse laths, the increment rate seems to get higher.

Figure 38 – KAM maps over the coarse martensite lath highlighted in Figure 35 at the following local strain levels: 1.24% (a), 2.29% (b), 4.32% (c), 5.92% (d). Frequency plot of the KAM values related to maps a, b, c and d, respectively (e-h).

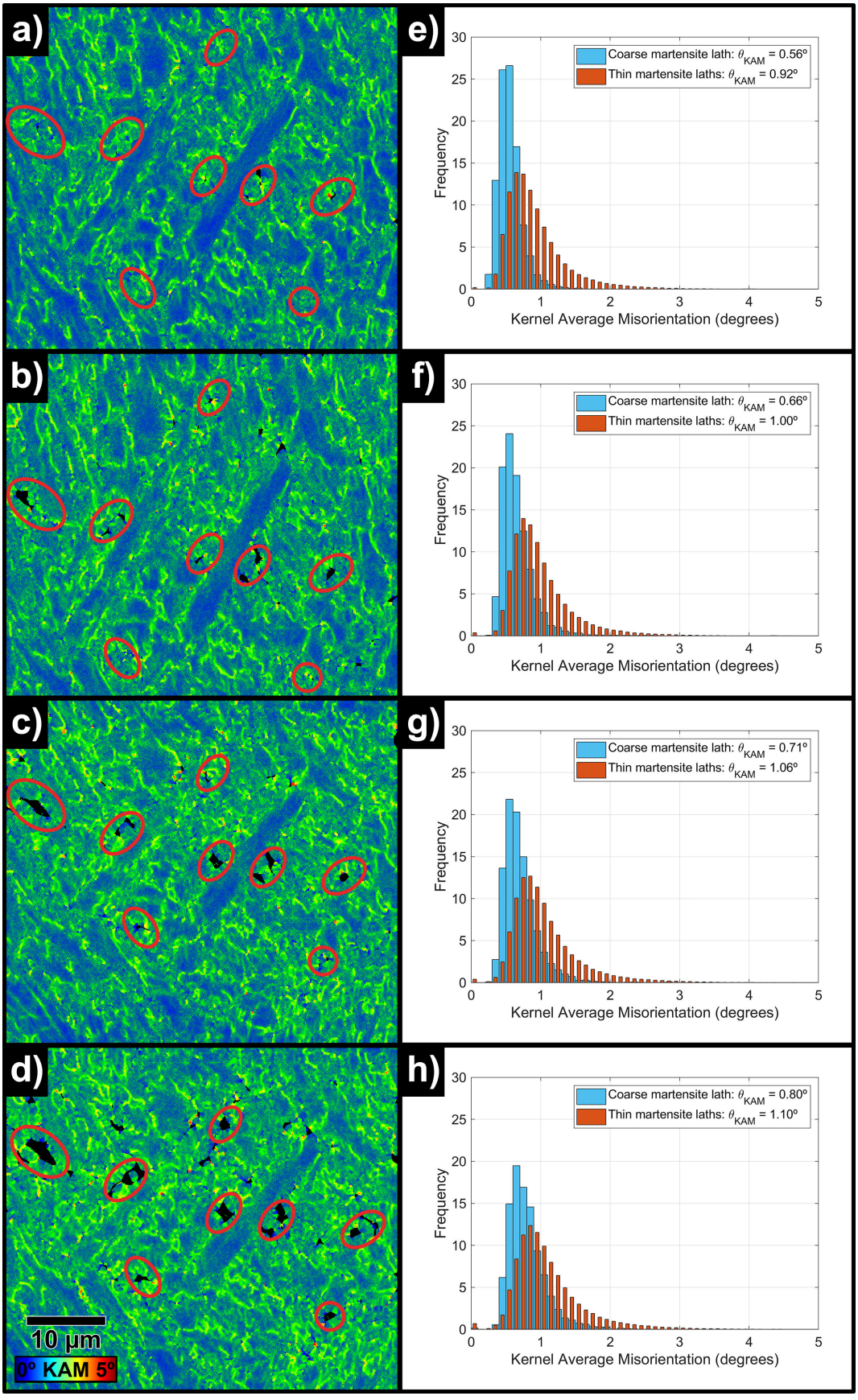

Source: Own elaboration.

Figure 39 – KAM maps over the coarse martensite lath highlighted in Figure 36 at the following local strain levels: 2.26% (a), 3.38% (b), 5.48% (c), 6.65% (d). Frequency plot of the KAM values related to maps a, b, c and d, respectively (e-h).

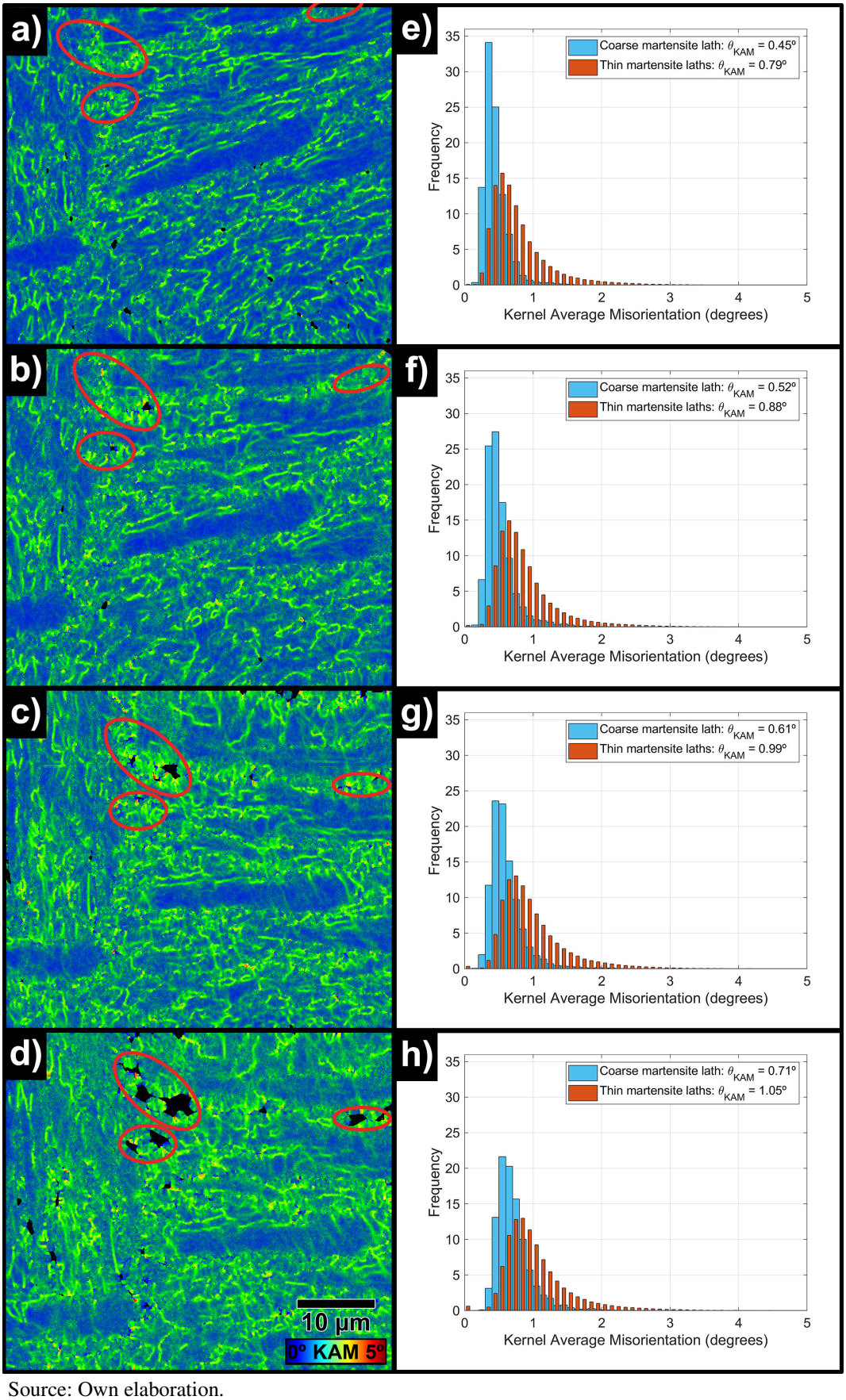

Source: Own elaboration.

Morito *et al.* (2003) and Harjo *et al.* (2017) reported that the overall dislocation density of lath martensite evolves linearly along with the strain increment. However, when considering the multiple lath martensite morphologies (FONDA; SPANOS, 2014; MORSDORF *et al.*, 2015), we see that this heterogeneity is reflected in the GND evolution. Morsdorf *et al.* (2016), in a study over another lath martensitic steel (Fe–0.13C–5.1Ni), observed that the plastic deformation would initiate at the coarse martensite laths, as, at low strain levels (up to 1.9%), a higher number of slip traces is observed in these constituents in comparison to observations in thin laths. The authors also noted that, for higher strain conditions, the coarse laths were covered with a dense pattern of slip steps, while significantly less slip activity was observed in the thin laths. However, as exhibited in Figure 42, the GND density increasing behaviour indicates that, in the early plastic regime, dislocation activity would mostly occur at the thin lath areas, while the coarse laths exhibit a more subtle increment in GND density. At first, this observation seems quite contradictory, since coarse laths are characterised as soft microconstituents (MORSDORF *et al.*, 2015), being, most likely, the first ones to yield. To comprehend this behaviour, it is necessary to consider the other microstructural features, such as the retained austenite.

The presence of thin interlath austenite films within the lath martensite microstructure is a well-established feature for a wide range of lath martensitic steels (MARESCA *et al.*, 2014), such as the 9Ni steel (ARAUJO *et al.*, 2021). The retention of these austenite films is mainly a result of chemical stabilisation, due to the alloying composition, and mechanical stabilisation, due to the transformation strain associated with martensitic transformation (MARESCA *et al.*, 2014). However, the contribution of this retained austenite to lath martensite plasticity is still unclear. Although some authors suggest that the thin austenite films contribute by enabling the sliding motion of lath martensite substructures (MARESCA *et al.*, 2014; DU *et al.*, 2016b; ARAUJO *et al.*, 2021), it was verified that the austenite initially retained between the martensite laths of a Fe-0.30C-5Ni steel is not detected at strain levels greater than 4%, indicating that the interlath austenite films might not effectively contribute to the overall plastic process (MORSDORF *et al.*, 2016). Even though the EBSD technique applied in the present study isn't well suited for the detection of these nanometric austenite films, some retained austenite clusters were identified in the analyses of the higher heat-input welding condition. As shown in the phase maps of Figures 41(a-e), the retained austenite undergoes a martensitic transformation induced by plastic strain throughout the progressive strain increment steps, so that, when a local strain level of 3.38% is reached, isn't detected any significant fraction of austenite.

Figure 40 – Phase maps (a-e), IPF maps (f-j) and GND density maps (k-o) for the 0%, 1.24%, 2.29%, 4.32% and 5.92% local strain levels, respectively. Maps estimated from the EBSD orientation data of the lower heat-input specimen.

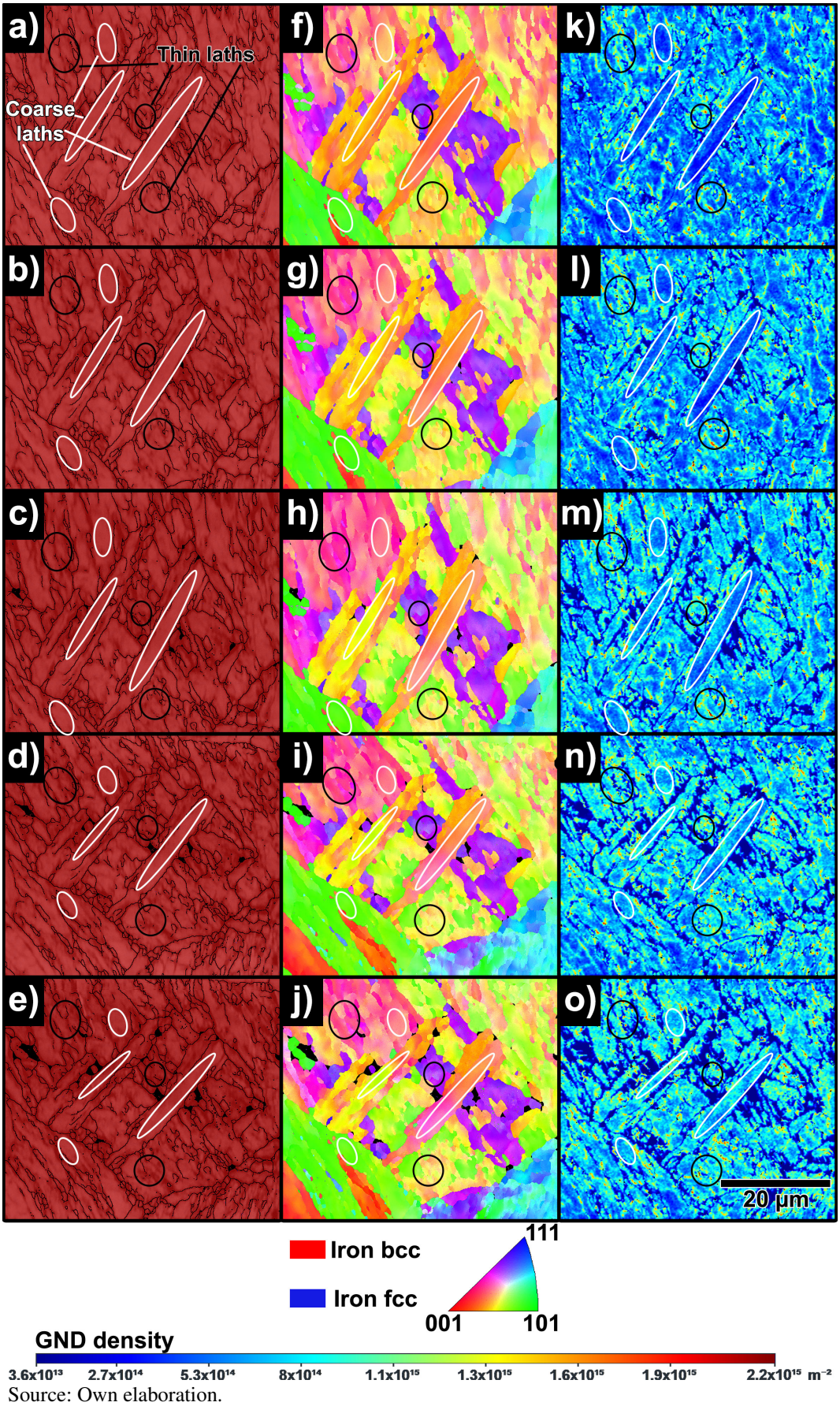

Source: Own elaboration.

Figure 41 – Phase maps (a-e), IPF maps (f-j) and GND density maps (k-o) for the 0%, 2.26%, 3.38%, 5.48% and 6.65% local strain levels, respectively. Maps estimated from the EBSD orientation data of the higher heat-input specimen.

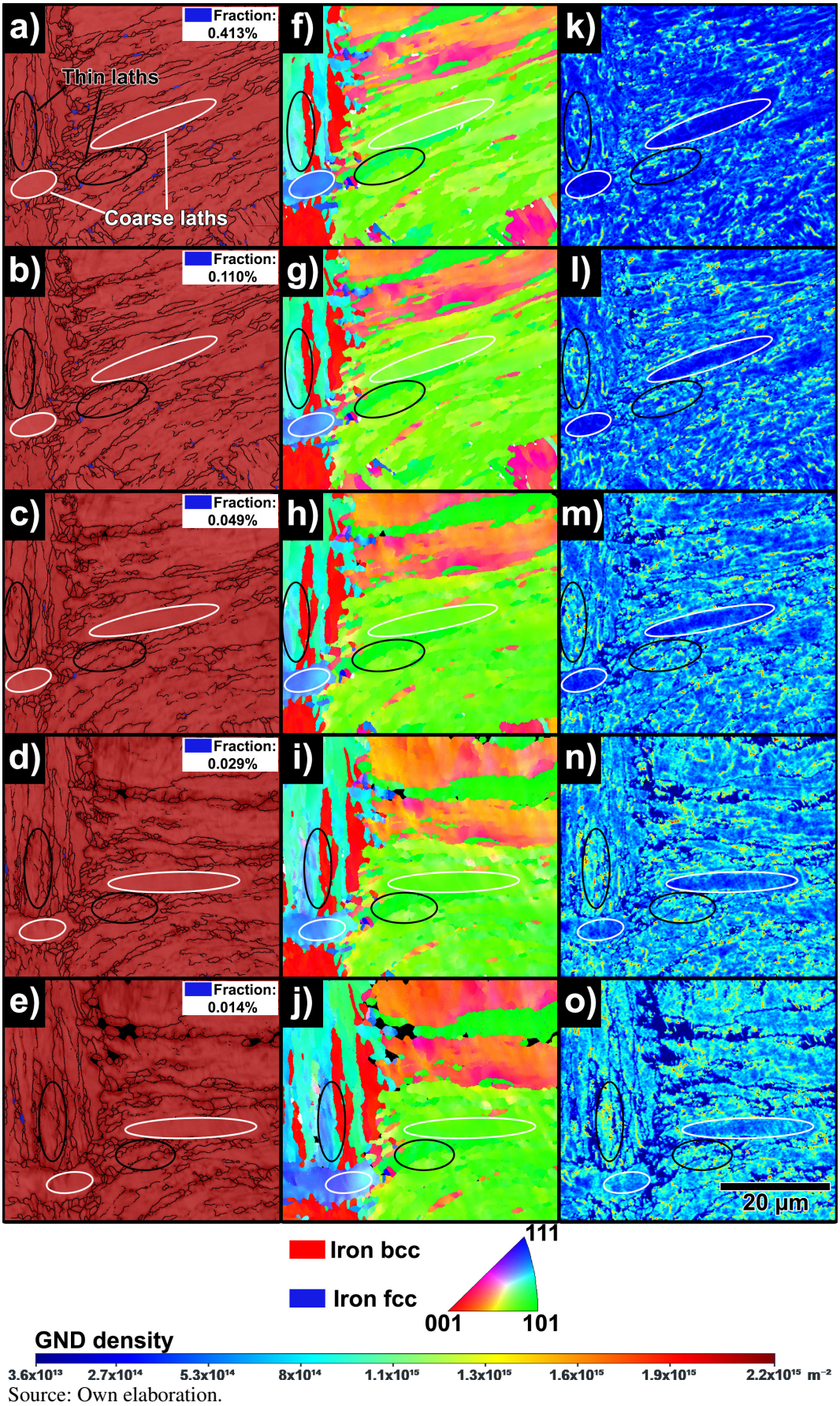

Source: Own elaboration.

It is expected that the interlath austenite follows a similar behaviour, undergoing a deformation-driven transformation into fresh martensite during the early stages of the plastic regime, as reported by Morsdorf *et al.* (2016). To achieve its initial chemical stability, it is likely that these thin austenite films were enriched by C and Ni atoms that have been expelled from the supersaturated BCC lattice during welding thermal cycles. Thus, fresh martensite films with high C content will be present at lath boundaries after light deformation. Continuing the deformation process, dislocation movement will be hindered by the high-carbon martensite films, creating high stress on the interface of lath boundaries (MORITO *et al.*, 2013). This interaction may explain the GND density increasing behaviour presented in Figure 42, as the early increase in thin laths' GND density may be related to the martensitic transformation induced by plastic strain of the interlaths austenite films. It should be noted that the analysis in the present work only assesses the GND, neglecting the statistically stored dislocations, as the EBSD analysis is limited to the evaluation of the former dislocation type.

Figure 42 – Evolution of the GND densities of the evaluated constituents during the deformation of the tensile specimens. Analyses on the lower heat-input condition (a) and the higher heat-input condition (b).

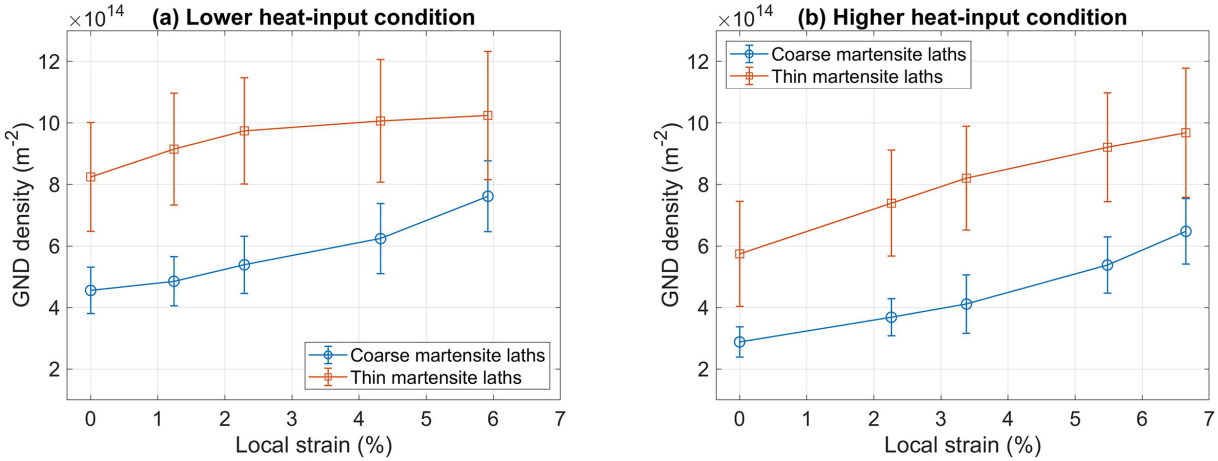

Source: Own elaboration.

After this initial plastic stage, the GND density increasing rate tends to get lower at the thin lath areas while getting higher at the coarse martensite laths, indicating that plastic strain manly proceeds through the coarse martensite deformation, which act as a reservoir of plasticity, highlighting the contribution of these microconstituents to the lath martensite overall plasticity. At the final strain increment steps, it is observed that the GND density levels of the coarse lath tend to reach those of the thin laths, getting the microstructure to a high constraint condition.

Figure 43 exhibits Taylor factor maps of the microstructures at the undeformed

condition. The Taylor factor would serve as a simplified measure that quantifies the amount of crystallographic shear required for compatible deformation per microscopic unit deformation step, being an approximate strength measure that evaluates the deformation ability of the martensite constituents under the applied loading conditions (TAYLOR, 1938). For the lower heat-input condition (Figure 43a), the selected coarse lath exhibits a low Taylor factor in comparison to the adjacent thin laths, indicating that the coarse constituent would present a higher deformation ability. In contrast, for the higher heat-input condition (Figure 43b), the selected coarse constituent exhibits a higher Taylor factor in comparison to some of the thin laths within the highlighted area. However, in both cases, the GND evolution follows the same behaviour. These results corroborate the analyses carried out by Morsdorf *et al.* (2016) in a Fe-0.13C-5.1Ni steel, which revealed that the localised microstructure strain does not reveal a strong correlation with the corresponding Taylor factor, indicating that the slip activity is altered by the initial yield strength distribution throughout the microstructure, which is related to the presence of retained austenite and the defect density and autotempering variations associated with the morphology heterogeneity (i.e. the contrast between coarse 'soft' laths and fine 'hard' laths).

Figure 43 – Taylor factor map of the selected areas for the analyses over the lower (a) and higher (b) heat-input welds. Undeformed condition.

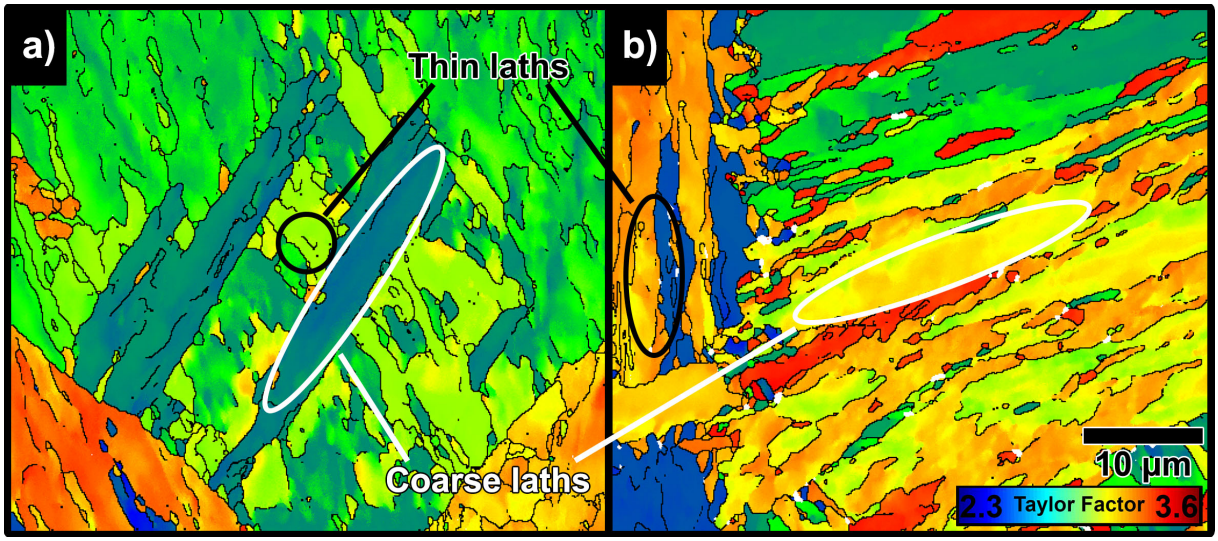

Source: Own elaboration.

The results exposed in this Subsection indicate that the lath martensite microstructure follows a hierarchy in its plastic deformation. First, intense dislocation activity associated with the deformation-driven martensitic transformation of interlath austenite films is observed at the lath boundaries. The resulted C-rich fresh martensite films hinder the dislocation movement at

the lath boundaries increasing the dislocation density and creating high stress on the interface. As the transformation of the interlath austenite proceeds, increasing dislocation activity is observed at the coarse laths, where the GND density increasing rate progressively rises along with the specimen strain level. It is expected that these coarse constituents may contribute by guaranteeing some plasticity during most of the early plastic regime until the microstructure reaches a state of high constraint, in which the dislocation density within the coarse laths would assume an equivalent value to the observed at the thin laths matrix. This plastic deformation hierarchy is summarised in the schematic presented in Figure 44.

Figure 44 – Schematic of the stages of plastic deformation in lath martensite microstrucutre.

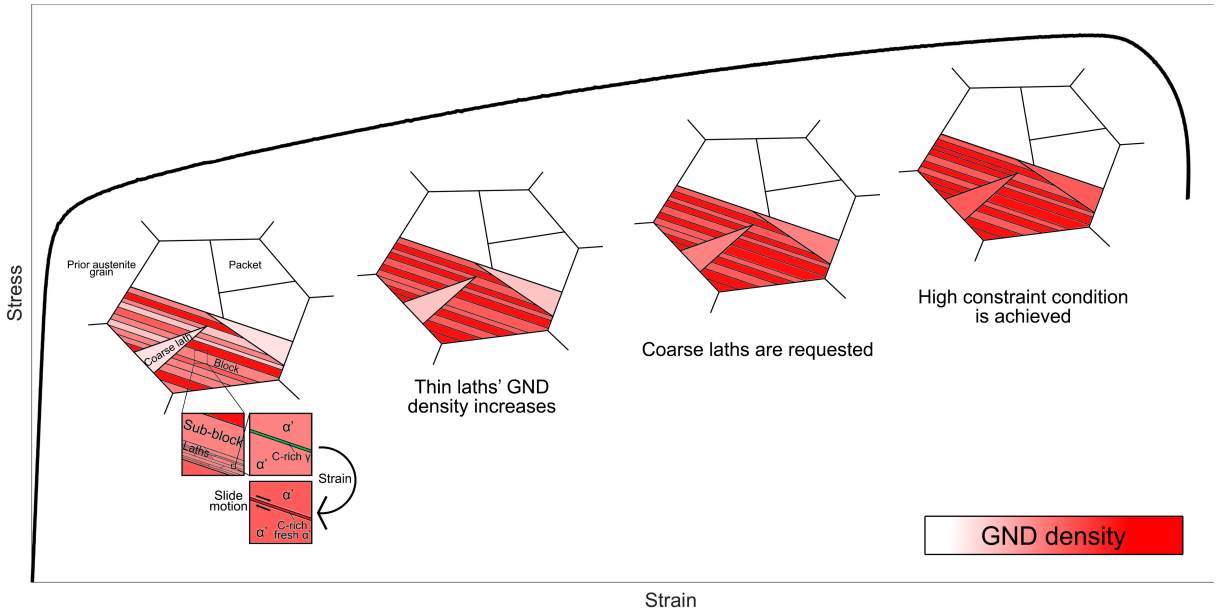

Source: Own elaboration.

4.5 Conclusion

The present work proposed an investigation covering macro- to micro-plasticity of 9Ni steel welded joints, focusing on the HAZ and the contribution of coarse martensite laths to the strain mechanisms of the microstructure. This study yielded the following conclusions:

a) The initial tensile tests revealed that the HAZ maintains its stability while the adjacent zones (FZ and BM) undergo a neck formation. Although the FZ yields first, being submitted to higher levels of plastic strain at the beginning of the plastic stage, an intense work hardening promotes the mechanical strengthening of this zone, hampering subsequent plastic deformation, which mainly proceeds at the BM, where a ductile fracture further occurs.

b) The only HAZ region that experiences significant strain is the CGHAZ, reaching higher strain levels at points closer to the weld interface. Also, the reheating cycles significantly impact the deformation ability, introducing microstructural heterogeneities that affect the local mechanical properties. The SC-CGHAZ experienced the higher strain levels, while the SCR-CGHAZ exhibited the lowest values throughout the CGHAZ.

c) Lath martensite microstructure follows a hierarchy in its plastic deformation. This hierarchy is associated with retained austenite films and the initial yield strength distribution throughout the microstructure, which is related to the morphology heterogeneity.

d) Initial dislocation activity is mostly a result of the deformation-driven martensitic transformation of interlath austenite films and the dislocation entanglement promoted by the resulted high C fresh martensite films. As the transformation of the interlath austenite proceeds, coarse constituents contribute by guaranteeing some plasticity during most of the early plastic regime until the microstructure reaches a state of high constraint.

e) The same plastic behaviour was observed in both lower and higher heat-input conditions. However, higher strain levels were achieved at the HAZ of the higher heat-input specimen, which exhibits a lower initial GND density due to the lower cooling rates.

5 SUMMARY

This thesis presented two main research topics developed and discussed in the studies exposed in Chapters 3 and 4. Both reports covered microstructural aspects of the HAZ in 9Ni steel girth welded pipes. While the first one proposes an extensive microstructural and micromechanical investigation along the HAZ evaluating multiple microstructural features at distinct HAZ regions, the second one focus on the plasticity of 9Ni steel welded joints, concentrating efforts on the evaluation of the HAZ plasticity and the contribution of coarse martensite laths to strain mechanisms of the microstructure. The obtained results yielded the following conclusions:

a) The primary strengthening mechanism acting in the HAZ regions is the grain size strengthening, as the martensite block refinement promoted by reheating and by heat-input condition follows a strong Hall-Petch relation with the microhardness values observed at the CGHAZ regions. It is expected that the precipitation strengthening would also impact the HAZ mechanical properties; however, the precipitation patterns at the martensite block and packet boundaries (as well as at the prior austenite grain boundaries) may blur the line between grain size strengthening and precipitation strengthening.

b) Along with the presence of wider martensite blocks, a larger coarse lath area fraction was considered a major responsible for the achievement of low average microhardness values at the SC-CGHAZ. Low microhardness values are observed at the IC-CGHAZ as well, a region that also presents a significant coarse martensite lath area fraction; however, the IC-CGHAZ presents a high deviation in microhardness values, which is probably related to the formation of hard fresh martensite and C-rich retained/reversed austenite particles.

c) Lath martensite microstructure follows a hierarchy in its plastic deformation. This hierarchy is associated with retained austenite films and the initial yield strength distribution throughout the microstructure. Initial dislocation activity is mostly a result of the deformation-driven martensitic transformation of interlath austenite films and the dislocation entanglement promoted by the resulted high C fresh martensite films. As the transformation of the interlath austenite proceeds, the softer coarse laths contribute by guaranteeing some plasticity during most of the early plastic regime until the microstructure reaches a state of high constraint, in

which the dislocation density within the coarse laths would assume an equivalent value to the observed at the thin laths matrix.

d) Increasing the welding heat-input achieves a softer HAZ which presents a coarser lath martensite microstructure, with wider martensite blocks and a more significant area fraction of coarse constituents. This increment is also responsible for expanding the extent of all HAZ regions and guaranteeing a higher deformation ability to the weld while lowering the initial GND density of the microstructure.

The present thesis brings solid results regarding the characterisation of a variety of microstructural features of the HAZ in 9Ni steel girth welded pipes, aiding in understanding how multipass welding processing may impact the microstructure and mechanical properties of the HAZ, allowing the optimisation of the welding parameters for manufacture of safer welded structures in many industrial sectors. The discussions presented here also bring new insights on the mechanical behaviour of lath martensite microstructure, verifying how its microconstituents – especially the coarse martensite laths – may contribute to its plastic deformation ability.

BIBLIOGRAPHY

AHSAN, Q.; HASEEB, A. S. M. A.; HUSSEIN, N. I. S. B.; CHANG, S. Y. 9% nickel steels and their welding behavior. In: HASHMI, S.; BATALHA, G. F.; VAN-TYNE, C. J.; YILBAS, B. (Ed.). **Comprehensive Materials Processing**. Oxford: Elsevier, 2014. p. 135–149.

AMERICAN WELDING SOCIETY. **A5.14 / A5.14M: 2011**: Specification for nickel and nickel-alloy bare welding electrodes and rods. 11. ed. Miami, FL, 2011.

ARAUJO, M. A. C.; VOGT, J.-B.; BOUQUEREL, J. Retained austenite-aided cyclic plasticity of the quenched 9Ni steel. **International Journal of Fatigue**, v. 152, p. 106445, 2021.

ARCHIE, F.; ZAEFFERER, S.; RAABE, D.; MÜNSTERMANN, S. **Damage nucleation in DP-steels: experimental characterization of the contributing microstructural parameters**. Thesis (PhD), 2018.

ARMSTRONG, T. N.; BROPHY, G. R. Some properties of 8.5% Ni steel. In: **Annual Conference of Petroleum Division**. Houston, TX: American Society of Mechanical Engineers, 1947. p. 402.

ARMSTRONG, T. N.; GAGNEBIN, A. P. **Impact Properties of Some Low Alloy Nickel Steels at Temperatures Down to-200 Degrees Fahr**. Materials Park, OH: American Society for Metals, 1940.

ASTM INTERNATIONAL. **A333 / A333M – 18**: Standard specification for seamless and welded steel pipe for low-temperature service and other applications with required notch toughness. West Conshohocken, PA, 2018.

BADINIER, G.; SINCLAIR, C.; SAUVAGE, X.; WANG, X.; BYLIK, V.; GOUNÉ, M.; DANOIX, F. Microstructural heterogeneity and its relationship to the strength of martensite. **Materials Science and Engineering: A**, v. 638, p. 329–339, 2015.

BAIN, E. C.; DUNKIRK, N. Y. The nature of martensite. **Transactions of the Metallurgical Society of AIME**, The American Institute of Mining, Metallurgical, and Petroleum Engineers, v. 70, n. 1, p. 25–47, 1924.

BARRICK, E. J.; DUPONT, J. N. Mechanical properties and microstructural characterization of simulated heat-affected zones in 10 wt pct Ni steel. **Materials Science and Engineering: A**, Elsevier, v. 748, p. 189–204, 2019.

BARRICK, E. J.; JAIN, D.; DUPONT, J. N.; SEIDMAN, D. N. Effects of heating and cooling rates on phase transformations in 10 wt pct Ni steel and their application to gas tungsten arc welding. **Metallurgical and Materials Transactions A**, Springer, v. 48, n. 12, p. 5890–5910, 2017.

BEAUSIR, B.; FUNDENBERGER, J. Analysis tools for electron and x-ray diffraction. **ATEX—software**, Université de Lorraine, 2017. Available from Internet: <www.atex-software.eu>.

BELTRÃO, R. L. C.; SOMBRA, C. L.; LAGE, A. C. V. M.; NETTO, J. R. F.; HENRIQUES, C. C. D. Challenges and new technologies for the development of the presalt cluster. In: **2009 Offshore Technology Conference**. Houston, TX: Offshore Technology Conference, 2009.

BHADESHIA, H. K. D. H.; HONEYCOMBE, R. **Steels: microstructure and properties**. 3. ed. Oxford: Butterworth-Heinemann, 2017.

BHADESHIA, H. K. D. H.; KEEHAN, E.; KARLSSON, L.; ANDRÉN, H.-O. Coalesced bainite. **Transactions of the Indian Institute of Metals**, Citeseer, v. 59, n. 5, p. 689–694, 2006.

BLACK, J. T.; KOHSER, R. A. **DeGarmo's materials and processes in manufacturing**. 10. ed. Hoboken, NJ: John Wiley & Sons, 2007.

BLONDEAU, R. **Metallurgy and mechanics of welding: processes and industrial applications**. Hoboken, NJ: John Wiley & Sons, 2013.

BOWLES, J. S.; MACKENZIE, J. K. The crystallography of martensite transformations I. **Acta metallurgica**, Elsevier, v. 2, n. 1, p. 129–137, 1954.

CALCAGNOTTO, M.; PONGE, D.; DEMIR, E.; RAABE, D. Orientation gradients and geometrically necessary dislocations in ultrafine grained dual-phase steels studied by 2D and 3D EBSD. **Materials Science and Engineering: A**, v. 527, n. 10, p. 2738–2746, 2010.

CEZAR, A. P.; PEREIRA, A. R.; DANIEL, L. L.; OAZEN, E.; TROVOADO, L.; ALMEIDA, M. C. de. Subsea Solutions in the Pre-Salt Development Projects. In: **2015 Offshore Technology Conference**. Houston, TX: Offshore Technology Conference, 2015.

COURTNEY, T. H. **Mechanical behavior of materials**. Long Grove, IL: Waveland Press, 2005.

DAVIS, C. L.; KING, J. E. Cleavage initiation in the intercritically reheated coarse-grained heat-affected zone: Part i. fractographic evidence. **Metallurgical and materials transactions A**, Springer, v. 25, n. 3, p. 563–573, 1994.

DING, M.; YUAN, F.; WANG, Y.; XIA, X.; CHEN, W.; LIU, D. Oil recovery from a CO_2 injection in heterogeneous reservoirs: The influence of permeability heterogeneity, CO_2-oil miscibility and injection pattern. **Journal of Natural Gas Science and Engineering**, v. 44, p. 140–149, 2017.

DU, C.; HOEFNAGELS, J.; VAES, R.; GEERS, M. Block and sub-block boundary strengthening in lath martensite. **Scripta Materialia**, v. 116, p. 117–121, 2016.

DU, C.; HOEFNAGELS, J. P. M.; VAES, R.; GEERS, M. G. D. Plasticity of lath martensite by sliding of substructure boundaries. **Scripta Materialia**, Elsevier, v. 120, p. 37–40, 2016.

DUHEN, T.; SAGOT, A.; KERBART, Y. Deep offshore slim hole drilling. In: **1997 Offshore Technology Conference**. Houston, TX: Offshore Technology Conference, 1997.

ELDEVIK, F.; GRAVER, B.; TORBERGSEN, L. E.; SAUGERUD, O. T. Development of a guideline for safe, reliable and cost efficient transmission of CO_2 in pipelines. **Energy Procedia**, v. 1, n. 1, p. 1579–1585, 2009.

FARIAS, F. W. C.; FILHO, J. d. C. P.; AZEVEDO, L. M. Barreto de. Microstructural and mechanical characterization of the transition zone of 9% Ni steel cladded with Ni-based superalloy 625 by GTAW-HW. **Metals**, Multidisciplinary Digital Publishing Institute, v. 8, n. 12, p. 1007, 2018.

FERNANDES, V. S.; FARIAS, F. W. C.; FILHO, J. da C. P. Fracture toughness of a 9% Ni steel pipe girth welded with Ni-based superalloy 625 filler metal operating in a sour environment. **Journal of Materials Research and Technology**, Elsevier, v. 9, n. 3, p. 6305–6321, 2020.

FEYNMAN, R. P. **The Character of Physical Law – The Distinction of Past and Future**. 1964. Lectures at Cornell University. Available from Internet: <https://youtu.be/YIOfOiZyQ3U>. Cited: feb. 15th, 2022.

FONDA, R. W.; SPANOS, G. Effects of cooling rate on transformations in a Fe-9 pct Ni steel. **Metallurgical and Materials Transactions A**, Springer, v. 45, n. 13, p. 5982–5989, 2014.

FONDA, R. W.; SPANOS, G.; VANDERMEER, R. A. Observations of plate martensite in a low carbon steel. **Scripta Metallurgica et Materialia**, Elsevier, v. 31, n. 6, p. 683–688, 1994.

FULTZ, B.; KIM, J. I.; KIM, Y. H.; KIM, H. J.; FIOR, G. O.; MORRIS, J. W. The stability of precipitated austenite and the toughness of 9Ni steel. **Metallurgical Transactions A**, Springer, v. 16, n. 12, p. 2237–2249, 1985.

FULTZ, B.; KIM, J. I.; KIM, Y. H.; MORRIS, J. W. The chemical composition of precipitated austenite in 9Ni steel. **Metallurgical Transactions A**, Springer, v. 17, n. 6, p. 967–972, 1986.

GRENINGER, A. B.; TROIANO, A. R. The mechanism of martensite formation. **Journal of Metals**, Springer, v. 1, n. 9, p. 590–598, 1949.

HARJO, S.; KAWASAKI, T.; TOMOTA, Y.; GONG, W.; AIZAWA, K.; TICHY, G.; SHI, Z.; UNGÁR, T. Work hardening, dislocation structure, and load partitioning in lath martensite determined by in situ neutron diffraction line profile analysis. **Metallurgical and Materials Transactions A**, Springer, v. 48, n. 9, p. 4080–4092, 2017.

HEDBERG, H. D.; MOODY, J. D.; HEDBERG, R. M. Petroleum Prospects of the Deep Offshore. **AAPG Bulletin**, v. 63, n. 3, p. 286–300, 1979.

HOU, W.; LIU, Q.; WEN, H.; GU, J. Effect of cyclic intercritical tempering on the microstructure and mechanical properties of a low-carbon Cu-bearing 7Ni steel. **Metallurgical and Materials Transactions A**, Springer, v. 51, p. 3981–3995, 2020.

HUTCHINSON, B.; HAGSTRöM, J.; KARLSSON, O.; LINDELL, D.; TORNBERG, M.; LINDBERG, F.; THUVANDER, M. Microstructures and hardness of as-quenched martensites (0.1–0.5%C). **Acta Materialia**, v. 59, n. 14, p. 5845–5858, 2011.

ISHEIM, D.; HUNTER, A. H.; ZHANG, X. J.; SEIDMAN, D. N. Nanoscale analyses of high-nickel concentration martensitic high-strength steels. **Metallurgical and Materials Transactions A**, Springer, v. 44, n. 7, p. 3046–3059, 2013.

JAIN, D.; ISHEIM, D.; ZHANG, X. J.; GHOSH, G.; SEIDMAN, D. N. Thermally stable Ni-rich austenite formed utilizing multistep intercritical heat treatment in a low-carbon 10 wt pct Ni martensitic steel. **Metallurgical and Materials Transactions A**, Springer, v. 48, n. 8, p. 3642–3654, 2017.

JAIN, D.; SEIDMAN, D. N.; BARRICK, E. J.; DUPONT, J. N. Atom-probe tomographic investigation of austenite stability and carbide precipitation in a TRIP-assisted 10 wt pct Ni steel and its weld heat-affected zones. **Metallurgical and Materials Transactions A**, Springer, v. 49, n. 4, p. 1031–1043, 2018.

JANG, J.-I.; JU, J.-B.; LEE, B.-W.; KWON, D.; KIM, W.-S. Effects of microstructural change on fracture characteristics in coarse-grained heat-affected zones of QLT-processed 9% Ni steel. **Materials Science and Engineering: A**, Elsevier, v. 340, n. 1-2, p. 68–79, 2003.

JANG, J.-I.; LEE, B.-W.; JU, J.-B.; KWON, D.; KIM, W.-S. Crack-initiation toughness and crack-arrest toughness in advanced 9 pct Ni steel welds containing local brittle zones. **Metallurgical and Materials Transactions A**, Springer, v. 33, n. 8, p. 2615–2622, 2002.

JANG, J.-I.; LEE, B.-W.; JU, J.-B.; KWON, D.; KIM, W.-S. Experimental analysis of the practical LBZ effects on the brittle fracture performance of cryogenic steel HAZs with respect to crack arrest toughness near fusion line. **Engineering fracture mechanics**, Elsevier, v. 70, n. 10, p. 1245–1257, 2003.

JANG, J.-I.; YANG, Y.-C.; KIM, W.-S.; KWON, D. Evaluation of cryogenic fracture toughness in SMA-welded 9% Ni steels through modified CTOD test. **Metals and Materials**, Springer, v. 3, n. 4, p. 230–238, 1997.

JANG, J.-I.; YANG, Y.-C.; KIM, W.-S.; KWON, D. A study of fracture toughness and microstructures in the weld heat-affected zone of QLT-processed 9% Ni steel. In: BALACHANDRAN, U. B.; GUBSER, D. G.; HARTWIG, K. T.; REED, R. P.; WARNES, W. H.; BARDOS, V. A. (Ed.). **Advances in Cryogenic Engineering Materials**. Boston, MA: Springer, 1998. p. 41–48.

KEEHAN, E.; KARLSSON, L.; BHADESHIA, H. K. D. H.; THUVANDER, M. Three-dimensional analysis of coalesced bainite using focused ion beam tomography. **Materials Characterization**, Elsevier, v. 59, n. 7, p. 877–882, 2008.

KELLY, P. M. Crystallography of lath martensite in steels. **Materials Transactions**, The Japan Institute of Metals, v. 33, n. 3, p. 235–242, 1992.

KIM, B. C.; LEE, S.; KIM, N. J.; LEE, D. Y. Microstructure and local brittle zone phenomena in high-strength low-alloy steel welds. **Metallurgical Transactions A**, Springer, v. 22, n. 1, p. 139–149, 1991.

KINNEY, C. C.; PYTLEWSKI, K. R.; KHACHATURYAN, A. G.; MORRIS, J. W. The microstructure of lath martensite in quenched 9Ni steel. **Acta materialia**, Elsevier, v. 69, p. 372–385, 2014.

KITAHARA, H.; UEJI, R.; TSUJI, N.; MINAMINO, Y. Crystallographic features of lath martensite in low-carbon steel. **Acta Materialia**, v. 54, n. 5, p. 1279–1288, 2006.

KNOOPE, M. M. J.; RAMÍREZ, A.; FAAIJ, A. P. C. A state-of-the-art review of techno-economic models predicting the costs of CO_2 pipeline transport. **International journal of greenhouse gas control**, Elsevier, v. 16, p. 241–270, 2013.

KOU, S. **Welding metallurgy**. 2. ed. Hoboken, NJ: John Wiley & Sons, 2003.

KRAUSS, G.; MARDER, A. R. The morphology of martensite in iron alloys. **Metallurgical Transactions**, Springer, v. 2, n. 9, p. 2343–2357, 1971.

KURDJUMOV, G.; SACHS, G. Over the mechanisms of steel hardening. **Zeitschrift für Physik**, Springer, v. 64, p. 325–343, 1930.

LEE, S. G.; SOHN, S. S.; KIM, B.; KIM, W. G.; UM, K.-K.; LEE, S. Effects of martensite-austenite constituent on crack initiation and propagation in inter-critical heat-affected zone of high-strength low-alloy (HSLA) steel. **Materials Science and Engineering: A**, v. 715, p. 332–339, 2018.

LEHOCKEY, E. M.; LIN, Y.-P.; LEPIK, O. E. Mapping residual plastic strain in materials using electron backscatter diffraction. In: ____. **Electron Backscatter Diffraction in Materials Science**. Boston, MA: Springer US, 2000. p. 247–264.

LIPPOLD, J. C.; KISER, S. D.; DUPONT, J. N. **Welding metallurgy and weldability of nickel-base alloys**. Hoboken, NJ: John Wiley & Sons, 2011.

LIPPOLD, J. C. *et al.* **Welding metallurgy and weldability**. Hoboken, NJ: John Wiley & Sons, 2015.

LONG, S. lei; LIANG, Y. long; JIANG, Y.; LIANG, Y.; YANG, M.; YI, Y. liang. Effect of quenching temperature on martensite multi-level microstructures and properties of strength and toughness in 20CrNi2Mo steel. **Materials Science and Engineering: A**, v. 676, p. 38–47, 2016.

LUO, H.; WANG, X.; LIU, Z.; YANG, Z. Influence of refined hierarchical martensitic microstructures on yield strength and impact toughness of ultra-high strength stainless steel. **Journal of Materials Science & Technology**, v. 51, p. 130–136, 2020.

MAHGEREFTEH, H.; ATTI, O. Modeling low-temperature-induced failure of pressurized pipelines. **AIChE journal**, Wiley Online Library, v. 52, n. 3, p. 1248–1256, 2006.

MARESCA, F.; KOUZNETSOVA, V. G.; GEERS, M. G. D. On the role of interlath retained austenite in the deformation of lath martensite. **Modelling and Simulation in Materials Science and Engineering**, IOP Publishing, v. 22, n. 4, p. 045011, 2014.

MARSHALL, C. W.; HEHEMANN, R. F.; TROIANO, A. R. The characteristics of 9% nickel low carbon steels. **Transactions of American Society for Metals**, American Society for Metals, v. 55, p. 135, 1962.

MATSUDA, F.; IKEUCHI, K.; FUKADA, Y.; HORII, Y.; OKADA, H.; SHIWAKU, T.; SHIGA, C. Review of mechanical and metallurgical investigations of M-A constituent in welded joint in japan. **Transactions of Joining and Welding Research Institute**, v. 24, n. 1, p. 1–24, 1996.

MICHIUCHI, M.; NAMBU, S.; ISHIMOTO, Y.; INOUE, J.; KOSEKI, T. Relationship between local deformation behavior and crystallographic features of as-quenched lath martensite during uniaxial tensile deformation. **Acta materialia**, Elsevier, v. 57, n. 18, p. 5283–5291, 2009.

MINE, Y.; HIRASHITA, K.; TAKASHIMA, H.; MATSUDA, M.; TAKASHIMA, K. Micro-tension behaviour of lath martensite structures of carbon steel. **Materials Science and Engineering: A**, Elsevier, v. 560, p. 535–544, 2013.

MIRANDA, H. C. de; SILVA, C. C. **Estudo da Soldabilidade de Aços Inoxidáveis Duplex e Superduplex: Relatório Técnico LPTS-CNPEM-9%Ni**. Fortaleza, CE, 2016.

MORITO, S.; HUANG, X.; FURUHARA, T.; MAKI, T.; HANSEN, N. The morphology and crystallography of lath martensite in alloy steels. **Acta Materialia**, Elsevier, v. 54, n. 19, p. 5323–5331, 2006.

MORITO, S.; NISHIKAWA, J.; MAKI, T. Dislocation density within lath martensite in Fe-C and Fe-Ni alloys. **ISIJ International**, v. 43, p. 1475–1477, 2003.

MORITO, S.; OHBA, T.; DAS, A. K.; HAYASHI, T.; YOSHIDA, M. Effect of solution carbon and retained austenite films on the development of deformation structures of low-carbon lath martensite. **ISIJ International**, v. 53, n. 12, p. 2226–2232, 2013.

MORITO, S.; TANAKA, H.; KONISHI, R.; FURUHARA, T.; MAKI, T. The morphology and crystallography of lath martensite in Fe-C alloys. **Acta materialia**, Elsevier, v. 51, n. 6, p. 1789–1799, 2003.

MORRIS, J. W. Stronger, tougher steels. **Science**, American Association for the Advancement of Science, v. 320, n. 5879, p. 1022–1023, 2008.

MORRIS, J. W. On the ductile-brittle transition in lath martensitic steel. **ISIJ international**, The Iron and Steel Institute of Japan, v. 51, n. 10, p. 1569–1575, 2011.

MORRIS, J. W.; GUO, Z.; KRENN, C. R.; KIM, Y. H. The limits of strength and toughness in steel. **ISIJ International**, The Iron and Steel Institute of Japan, v. 41, n. 6, p. 599–611, 2001.

MORRIS, J. W.; KINNEY, C.; PYTLEWSKI, K.; ADACHI, Y. Microstructure and cleavage in lath martensitic steels. **Science and technology of advanced materials**, IOP Publishing, v. 14, n. 1, p. 014208, 2013.

MORSDORF, L.; EMELINA, E.; GAULT, B.; HERBIG, M.; TASAN, C. Carbon redistribution in quenched and tempered lath martensite. **Acta Materialia**, v. 205, p. 116521, 2021.

MORSDORF, L.; JEANNIN, O.; BARBIER, D.; MITSUHARA, M.; RAABE, D.; TASAN, C. C. Multiple mechanisms of lath martensite plasticity. **Acta Materialia**, Elsevier, v. 121, p. 202–214, 2016.

MORSDORF, L.; TASAN, C. C.; PONGE, D.; RAABE, D. 3D structural and atomic-scale analysis of lath martensite: effect of the transformation sequence. **Acta Materialia**, Elsevier, v. 95, p. 366–377, 2015.

MU, W.; LI, Y.; CAI, Y.; WANG, M. Cryogenic fracture toughness of 9% Ni steel flux cored arc welds. **Journal of Materials Processing Technology**, Elsevier, v. 252, p. 804–812, 2018.

MU, W.; LI, Y.; CAI, Y.; WANG, M.; HUA, X. The cryogenic low-cycle fatigue performance of 9% Ni steel joint made by flux cored arc welding. **Materials Characterization**, Elsevier, v. 151, p. 27–37, 2019.

NIPPES, E. F.; BALAGUER, J. P. A study of the weld heat-affected zone toughness of 9% nickel steel. **Welding Journal**, AWS, v. 65, n. 9, p. 237, 1986.

NISHIYAMA, Z. X-ray investigation of the mechanism of the transformation from face centered cubic lattice to body centered cubic. **Science Reports of Tohoku University**, Tohoku University, v. 23, p. 637, 1934.

OLSON, G. B.; AZRIN, M. Transformation behavior of TRIP steels. **Metallurgical Transactions A**, Springer, v. 9, n. 5, p. 713–721, 1978.

PANTLEON, W. Resolving the geometrically necessary dislocation content by conventional electron backscattering diffraction. **Scripta Materialia**, v. 58, n. 11, p. 994–997, 2008.

PATEL, D. Developments in LNG storage: overview of LNG storage tanks. In: **Third International Conference on Experimental Mechanics and Third Conference of the Asian Committee on Experimental Mechanics**. Beijing: BGS group, 2000. v. 1651, p. 1–13.

PENSE, A. W.; STOUT, R. D. Fracture toughness and related characteristics of the cryogenic nickel steels. **Welding Research Council Bulletin**, Welding Research Council, n. 205, p. 1–43, 1975.

RAMACHANDRAN, D. C.; KIM, S.-D.; MOON, J.; LEE, C.-H.; CHUNG, J.-H.; BIRO, E.; PARK, Y.-D. Classification of martensite-austenite constituents according to its internal morphology in high-strength low alloy steel. **Materials Letters**, v. 278, p. 128422, 2020.

RIOS, M. C. G.; FILHO, J. d. C. P.; FARIAS, F. W. C.; PASSOS, A. V. *et al.* Microstructural characterization of the simulated heat-affected zone of 9 pct Ni steel. **Metallurgical and Materials Transactions A**, Springer, v. 52, n. 11, p. 5016–5031, 2021.

SCHEID, A.; FÉLIX, L. M.; MARTINAZZI, D.; RENCK, T.; KWIETNIEWSKI, C. E. F. The microstructure effect on the fracture toughness of ferritic Ni-alloyed steels. **Materials Science and Engineering: A**, Elsevier, v. 661, p. 96–104, 2016.

SHAMSUJJOHA, M. Evolution of microstructures, dislocation density and arrangement during deformation of low carbon lath martensitic steels. **Materials Science and Engineering: A**, v. 776, p. 139039, 2020.

SHIBATA, A.; NAGOSHI, T.; SONE, M.; MORITO, S.; HIGO, Y. Evaluation of the block boundary and sub-block boundary strengths of ferrous lath martensite using a micro-bending test. **Materials Science and Engineering: A**, v. 527, n. 29, p. 7538–7544, 2010.

SHIN, H.-S.; LEE, H.-M.; KIM, M.-S. Impact tensile behaviors of 9% nickel steel at low temperature. **International Journal of Impact Engineering**, v. 24, n. 6, p. 571–581, 2000.

STRIFE, J. R.; PASSOJA, D. E. The effect of heat treatment on microstructure and cryogenic fracture properties in 5Ni and 9Ni steel. **Metallurgical Transactions A**, Springer, v. 11, n. 8, p. 1341, 1980.

TAYLOR, G. I. Plastic strain in metals. **Journal of the Institute of Metals**, v. 62, p. 307–324, 1938.

UEKI, S.; MINE, Y.; TAKASHIMA, K. Microstructure-sensitive fatigue crack growth in lath martensite of low carbon steel. **Materials Science and Engineering: A**, v. 773, p. 138830, 2020.

WASSERMANN, G. Über den mechanismus der α-γ umwandlung des eisens. **Mitteilungen aus dem Kaiser-Wilhelm-Institut für Eisenforschung zu Düsseldorf; Verlag Stahleisen: Düsseldorf, Germany**, 1935.

WELDWIRE. **ERNiCrMo-3**. 2021. Available from Internet: <https://www.weldwire.net/weld_products/wwnicrmo-3/>. Cited: may. 30th, 2022.

WRIGHT, S. I.; NOWELL, M. M.; FIELD, D. P. A review of strain analysis using electron backscatter diffraction. **Microscopy and Microanalysis**, Cambridge University Press, v. 17, n. 3, p. 316–329, 2011.

XIAO, X.; TERENTYEV, D.; YU, L.; BAKAEV, A.; JIN, Z.; DUAN, H. Investigation of the thermo-mechanical behavior of neutron-irradiated Fe-Cr alloys by self-consistent plasticity theory. **Journal of Nuclear Materials**, v. 477, p. 123–133, 2016.

YANG, Y.-H.; CAI, Q.-W.; TANG, D.; WU, H.-B. Precipitation and stability of reversed austenite in 9Ni steel. **International Journal of Minerals, Metallurgy, and Materials**, Springer, v. 17, n. 5, p. 587–595, 2010.

YU, L.; XIAO, X.; CHEN, L.; CHENG, Y.; DUAN, H. A hierarchical theoretical model for mechanical properties of lath martensitic steels. **International Journal of Plasticity**, Elsevier, v. 111, p. 135–151, 2018.

ZHANG, J. M.; LI, H.; YANG, F.; CHI, Q.; JI, L. K.; FENG, Y. R. Effect of heat treatment process on mechanical properties and microstructure of a 9% Ni steel for large LNG storage tanks. **Journal of materials engineering and performance**, Springer, v. 22, n. 12, p. 3867–3871, 2013.

ZHANG, X. J. Microhardness characterisation in developing high strength, high toughness and superior ballistic resistance low carbon Ni steel. **Materials Science and Technology**, Taylor & Francis, v. 28, n. 7, p. 818–822, 2012.